HI analysis of resolved galaxies in the MeerKAT Absorption Line Survey

A thesis submitted for the degree of

DOCTOR OF PHILOSOPHY

of

RHODES UNIVERSITY

By

ERIC KAMAU MAINA

ORCID ID

https://orcid.org/0000-0002-6131-6100

September 13, 2024

I have prepared my thesis for the degree of Doctor of Philosophy, while under the supervision in the Department of Physics and Electronics, Rhodes University.

Supervisors:
Dr Gyula I. G. Józsa
Prof Oleg Smirnov

Co-supervisors:
Dr Neeraj Gupta

Abstract

This doctoral thesis examines two galaxy groups, Klemola 31 and UGC 439, leveraging the observational capabilities of the MeerKAT Absorption Line Survey (MALS). The focus was on studying the interstellar medium, specifically the neutral hydrogen (H I) content, distribution, density, and dynamics, through high spatial resolution observations of these groups, and therefore offering insights into the complex processes affecting galaxy evolution in different environments. To make use of an additional tool, the absorption line characteristics of H I in the two observed systems were analysed and compared with the kinematics and the morphology as induced by the observation of the H I emission line in the same systems. For Klemola 31, this thesis identifies significant H I deficiencies and interactions between member galaxies, with notable evidence of tidal interactions between Klemola 31 A and Klemola 31 B as well as ESO400-11 and LEDA 2807038; and possible ram-pressure stripping in ESO400-13. The combined analysis of the H I in emission and absorption indicates the presence of an extraplanar and potential intra-group medium in the group. The UGC 439 group was observed in the commissioning phase of the MeerKAT array, revealing contrasting H I distributions, with the central three galaxies indicating H I excess while the peripheral galaxies indicating H I deficiencies. There are two H I clouds, one close to the central three galaxies and the other to the north. In this case, the observations are consistent with an H I absorption system from within the disk of a galaxy. This thesis also highlights the necessity for further high spatial and spectral resolution observations to further reveal the intricacies of gas dynamics and its critical role in the life-cycle of galaxies. It serves as an outlook for further studies of the H I environment of galaxies by combining absorption and emission line studies as first provided by MALS and ultimately by deep H I surveys with the Square Kilometre Array. This thesis is organised into four chapters. The first chapter details a few concepts and background information about the physics of galaxy evolution. Chapter two talks about Klemola 31 galaxy group, where we start by describing our observation, data reduction and source finding. Thereafter, we explore the H I morphology and kinematics of this group. In Chapter Three, we turn our attention to UGC 439 galaxy group and organise it in a similar manner. A summary and comparison of the two groups is presented in Chapter 4.

Contents

List of Figures

List of Tables

Acknowledgements

I am really thankful for the opportunity to embark on this PhD journey. This thesis reflects not just my work but the unwavering support and collective wisdom of many remarkable individuals and institutions. Foremost, I extend my deepest gratitude to God for seeing me through my entire PhD Journey. Secondly, from the bottom of my heart, I would like to thank my supervisor, Dr Gyula I. G. Józsa, who is not merely an outstanding guide but a beacon of kindness, support, and understanding. Your unparalleled dedication, patience and hospitality have profoundly influenced me, making my PhD journey a truly enjoyable experience. I could not have asked for a better mentor. I would also like to thank my co-supervisor, Dr Neeraj Gupta, for your continued support and willingness to always help, and Abhisek Mohapatra for our constant discussions and making yourself available when I needed assistance. I am also really grateful to Prof Oleg Smirnov for your hospitality, support and understanding throughout my journey, as well as all the co-authors of my first paper, which would not have been possible without your support. I thank the Centre for Radio Astronomy Techniques and Technologies (RATT), the South African Radio Astronomy Organisation (SARAO), the South African National Research Foundation (NRF) and the National Science Foundation (NSF) for funding my studies. Special thanks to Thandiwe Matyobeni, Abednego Nzyuko, Noluvuyo Vuyo Matiwane, Koketso Mophahlane, Portia Legodi, Kristena Reddy and friends for your continuous support, encouragement and for adding spice to my life. I would also like to thank all my colleagues, and in particular, the RATT group members, for your support. And I would finally like to thank my family for your continued understanding and support during this journey.

Chapter 1

Introduction

In the chapters following this one, the observation of two galaxy groups is described, in which the chance coincidence of a distant bright background radio continuum source and a galaxy group causes an H I absorption line. The H I properties of the systems are studied, combining the information from the H I in emission and absorption, in order to study the physical processes acting on the gaseous components in the galaxy group and the individual galaxies.

In this chapter, a few concepts and background information about the physics of galaxy evolution, observational techniques and parameters, and their interpretation are laid out. Some of these have been used in the study of the astrophysical objects that are the subject of this thesis. Here, however, a somewhat more comprehensive overview shall be given to put the work into a scientific and technical context.

1.1 H I properties of galaxies in group environments

A star is born when a dense molecular cloud, mainly consisting of cool and cold hydrogen, collapses under its gravitational weight. Molecular hydrogen (H_2) and atomic neutral hydrogen (H I) are key ingredients in star formation. New stars are born at a given rate in a given volume in space, defining the star formation rate (SFR) density, which determines how efficient a galaxy is at forming stars. In recent years, a lot of work has gone into determining the global SFR density at redshifts of up to $z \sim 8$ (e.g. Madau & Dickinson, 2014; Hoppmann et al., 2015). From these studies, it has been deduced that there is a peak SFR density in the redshift range $1 < z < 3$ followed by an order of magnitude's decrease towards $z \sim 0$ corresponding to the last 10 Gyr or 70% of the age of the universe (Bouwens et al., 2014).

To understand the evolution of the SFR density with redshift and to attempt to uncover this shift in SFR at lower redshifts, it is imperative for us to understand the processes leading to the conversion of H I into H_2 and, eventually, to stars. To understand these processes, we need to observe molecular gas, which fuels star formation, as well as the atomic hydrogen, galaxies' reserve fuel for star formation and the dominant gas component of galaxies. In this study, we focus on observations of the neutral hydrogen gas, H I, in galaxies using the 21-cm emission line.

1.1.1 Galaxy Groups

Gas accretion and, consequently, the star formation process does not happen in isolation but rather in galaxies, which are integrated into the cosmic web and outline voids, filaments, clusters and groups. Galaxy groups tend to have lower mass, velocity dispersion and sizes compared to galaxy clusters. Compact galaxy groups are a subset of galaxy groups that typically have 4-5 galaxies with apparent densities of 10^6 Mpc^{-3} .

1.1.2 Environments of galaxies

Several authors (Giovanelli & Haynes, 1985; Chung et al., 2009; Solanes et al., 2001; Healy et al., 2021) studied a large sample of galaxies and found that those with low H I gas content are usually found in high-density environments in contrast to those with high H I gas content which are found in low-density environments. This suggests that galaxies in clusters lose their gas and stop forming stars and, therefore, become quenched via either ram-pressure stripping (e.g. Gunn & Gott III, 1972) where the gaseous disk of a galaxy becomes disrupted as it passes through the intergalactic medium at high velocities; or tidal disruption (e.g. Byrd & Valtonen, 1990; Moore et al., 1998) where galaxies' stellar and gaseous disks become disrupted potentially losing gas as a consequence of gravitational interaction. These processes lead to the galaxies' strangulation or starvation, where the weakly bound gas in galaxies is stripped off, leading to quenching of the star formation once the gas supply is exhausted (e.g. Larson et al., 1980). On the other hand, galaxies in field populations tend to accrete gas and keep forming stars as they are free from strangulation or starvation effects. Solanes et al. (2001) and Kilborn et al. (2009) found that there is a relationship between the galaxy morphology and the degree of H I depletion in groups and clusters where early type and dwarf spiral galaxies being more depleted.

There are several processes that can disturb H I disks, ranging from ram-pressure stripping and tidal interaction to galaxy merger and accretion events. There are several signatures when it comes to ram-pressure stripping. Among them are truncated H I discs, lopsided H I morphologies, enhanced star formation on the leading edge of galaxies in nearby clusters as well as one-sided H I tails (e.g. Yoon et al., 2017; Cayatte et al., 1990; Vollmer et al., 2001; Chung et al., 2009). There has also been evidence of disturbed H I gas and high column density rings in galaxies hosting transient phenomena such as supernovae, Fast-Evolving Luminous Transients, Fast Radio Bursts and Gamma Ray Bursts (e.g. Roychowdhury et al., 2019; Kaur et al., 2022; Arabsalmani et al., 2015). Evidence of galaxy pre-processing, the entirety of evolutionary processes connected to gas removal prior to the first entry of a galaxy into galaxy clusters, (e.g. Zabludoff & Mulchaey, 1998; Poggianti et al., 1999; Kantharia et al., 2005; Catinella et al., 2013; Hess & Wilcots, 2013) has been found in the outskirts of galaxy clusters.

Roychowdhury et al. (2022) found H I gas in the intergalactic space between low-mass ($M_*\leq 10^{9.5}\ M_\odot$) galaxy groups indicative of galaxy pre-processing. In addition to this, recent high spatial resolution studies with the VLA and GMRT have revealed more evidence of interaction and H I gas accretion, among them being Beygu et al. (2013); Chengalur & Pustilnik (2013); Chengalur et al. (2017) who found triplets of gas-rich galaxies in voids and arranged in an almost a linear fashion, possibly due to material flow along the filament.

At the other end of the spectrum, we have void galaxies. Void galaxies exist in relative isolation, freeing them of the processes typical of group or cluster galaxies. These void galaxies are usually less evolved and usually have a younger stellar population than cluster or group galaxies (e.g. Aragon-Calvo & Szalay, 2013). Observations of void galaxies by Moorman et al. (2014, 2016); Rojas et al. (2004); von Benda-Beckmann & Müller (2008); Patiri et al. (2006) have shown that they tend to be smaller, bluer and have a higher star forming rate as compared to their cluster and group counterparts. However, this is not a strict rule. Studies show that for a fixed morphology and luminosity, bright void galaxies with magnitudes M $<$ -16.5 can have identical star formation rates as those from field galaxies (e.g. Kreckel et al., 2012), whereas fainter dwarf galaxies in voids tend to have higher specific star formation rate (SFR) than field dwarfs (Moorman et al., 2016; von Benda-Beckmann & Müller, 2008). In addition to this, brighter void galaxies have been found to have similar H I gas content when compared to field galaxies (e.g. Kreckel et al., 2012) whereas low luminosity galaxies in voids tend to have higher H I gas content when compared to field galaxies (Pustilnik & Martin, 2016). In terms of the H I disk extent, Kurapati (2020) found that the H I disk of galaxies in voids are $\sim 4.5-5$ times larger than their optical counterparts.

This forms the basis of the morphology-density relation (Dressler et al., 1997), where early-type galaxies are preferably found in high-density environments such as galaxy clusters, while late-type galaxies are preferably found in low-density environments such as the field. This correlation between galaxy morphology and environment indicates that a galaxy's environment can be a primary determinant of its gas content and, therefore, prompts several questions, including how galaxies evolve in the group environment in terms of their morphology, star formation rate and gas content. Therefore, we can understand galaxy evolution in dense environments by studying the removal and subsequent depletion of cold gas in galaxies (Sancisi et al., 2008a; Schawinski et al., 2014). Recent H I studies have shed light to the possibility of having H I rich galaxy groups (e.g. Ranchod et al., 2021; Glowacki et al., 2024) and a possible dissociation between H I deficiency and evolutionary phase of a compact group (Jones et al., 2023).

1.1.3 Hickson Compact Groups

The Hickson compact group (HCG) is a subset of compact galaxy groups and serves as key laboratories for examining the role and impact of the environment on galaxies. Hickson (1982) created a catalogue of 100 galaxy groups, in which they list a collection of 4 to 5 galaxies with small projected separations, examples being Stephan's Quintet and Seyfert's Sextet. Follow-up spectroscopic observations of this catalogue showed that 92 out of 100 galaxy groups had galaxies with the right redshift range, where the right range was defined as galaxies that fall within 100 $km\,s^{-1}$ of the median velocity of the group.

It is not uncommon to observe chance alignments of galaxy groups and fore- or background galaxies (e.g. Burbidge & Burbidge, 1959, 1961; Sargent, 1968). Therefore, it becomes imperative to do follow-up spectroscopic observations of the member galaxies. Other than spectroscopic observations, it is also possible to use the kinematics and morphology of these galaxies as well as X-ray emission permeating the group, albeit weak, as the compact nature of these groups more often than not results in interactions leading to kinematic and morphological changes as well as the striping of material from galaxies into the intergroup medium which ends up being the source of X-rays. To be specific, the H I morphology of HCGs appears to follow an evolutionary sequence of three main phases. H I is initially confined to galaxies, then, as galaxies interact, they gradually lose gas to the intragroup medium (Jones et al., 2019) to the point of depletion (Jones et al., 2023) while the diffuse intragroup H I becomes evaporated by the UV background and heated up over several Gyr resulting in the intragroup X-ray emission (Verdes-Montenegro et al., 2001; O'Sullivan et al., 2014).

Given that these galaxies have small projected separations, more than 40% of the galaxies in HCG show signs of interactions, while about 3/4 of them show an extended X-ray emission whose origin could possibly be hot intergroup gas, serving as evidence of a common gravitational well in the group and further evidence that the member galaxies are indeed physical neighbours in 3-dimensional space and the alignment is not due to mere projection effects(Belsole et al., 2003; Desjardins et al., 2013).

The compact nature of these groups and, consequently, high densities coupled with low-velocity dispersion should make interactions relatively strong, leading to an enhanced level of star formation compared to field galaxies, but less than strongly interacting galaxy pairs, and possible mergers. This is yet another clue that could be used to determine if a given galaxy belongs to the parent galaxy group.

However, observed velocity dispersions typically range from a few tens to several hundred $km\,s^{-1}$ with a median value of the order of 200 $km\,s^{-1}$ (Barnes, 1989). This is usually larger than can be accounted for by luminous matter alone, serving as evidence of dark matter permeating the group and dominating the group's dynamics. However, it later became apparent that even though galaxies in groups would be dynamically bound, they would be inherently unstable as galaxies' orbital decay due to dynamic friction would lead to their halos being stripped and them merging eventually.

Governato et al. (1995) also suggested that in a high-density universe, galaxy groups could be rejuvenated by new member galaxies joining the compact group. Specifically, new galaxies become trapped by the group's gravitational well and fall into the group, resulting in an increase in the group's net mass. A direct consequence of increasing the group's mass is an increase in the group's velocity dispersion. As individual galaxies move through the group's intergalactic medium, their neutral gas disk, as well as their gaseous halo, could be stripped off, resulting in an increase of the group's halo mass as well as an increase in the intergalactic diffuse gas content.

Dynamic friction plays its role as well by slowing down member galaxies as they move through the group. In this process, the member galaxies lose their energy as they move through a volume of dark matter sub-halos within the group, which slows them down. This process continues until galaxies merge on a time scale referred to as the dynamic friction timescale t_d. The dynamic friction timescale depends on the amount and distribution of dark matter but is usually ten times the average time it takes for an individual galaxy to cross a group (crossing time) and ranges from 10^{-3} to 10^{-1} Hubble time with 0.02 being the median Hubble time and 1 Hubble time being the age of the universe. As more galaxies interact and merge with each other, the fraction of elliptical and S0 galaxies increases. This process would continue until a single massive remnant resembling an elliptical galaxy is formed (Barnes, 1989).

Therefore, one would expect compact group remnants to resemble massive elliptical galaxies, as well as the current population of remnants of compact groups of galaxies, to exceed the current population of compact groups by an order of magnitude. However, the total luminosity of individual compact groups exceeds that of a typical elliptical galaxy by several magnitudes, making it difficult to understand the properties of compact group remnants (Mendes de Oliveira & Hickson, 1991). However, it is also possible that the compact groups could have survived by gaining energy when new galaxies fall into the group rejuvenating the system and increasing the group's velocity dispersion.

The possibility of revitalizing star formation in the nuclear region of galaxies or AGN activation due to group activity has been an area of interest (Keel et al., 1985). Evidence points to the possibility of nuclear activity being activated by interactions in small groups of galaxies, especially for higher-luminosity galaxies (Sabater et al., 2013). For example, a large fraction of ultra-luminous galaxies in the infrared contains Seyfert nuclei, believed to be triggered by interactions (Sanders & Mirabel, 1996). Seyfert nuclei are a type of active galactic nuclei (AGN) that are powered by accreting material into a supermassive black hole at the centre of their host galaxies. Interaction between galaxies could result in material being funnelled into the supermassive black hole at the centre of the galaxy, fuelling and activating it.

1.2 Galaxy Scaling Relations

Scaling relations refer to the observable statistical relationships between various physical properties of galaxies, such as their mass, luminosity, size, velocity dispersion, rotation velocity and so on. They are instrumental in galaxy formation models as they form an observational basis with which such models can be tested.

1.2.1 Star formation law

The relationship between the amount of gas in galaxies and their star formation rate (SFR) plays a key role in regulating star formation and, consequently, galaxy evolution. One such empirical relationship between the cold gas (H I and H_2) surface density and the SFR has been quantified by Schmidt and Kennicutt (Schmidt, 1959b; Kennicutt & Van Der Hulst, 1997):

$$\Sigma_{SFR} = A\Sigma_{gas}^{N} \quad , \tag{1.1}$$

where Σ_{SFR} is the star formation rate surface density in ($M_\odot$ kpc^{-2} yr^{-1}) and Σ_{gas}^{N} the cold gas surface density in ($M_\odot$ pc^{-2}) and A the constant of proportionality. . An equally relevant relationship between gas surface density and star formation rate is given by (Kennicutt Jr., 1998)

$$\Sigma_{\rm SFR} = B\frac{\Sigma_{\rm gas}}{\tau_{\rm dyn}} \quad , \tag{1.2}$$

where $\tau_{\rm dyn}$ is the dynamical time described as the orbital time for a star-forming disk. Taking H I and H_2 averaged gas surface densities and averaging over galactic disks, Kennicutt Jr. (1998) found an index value $N = 1.4$, as can be seen in Fig. 1.1; however, different studies have found varying values for the value of N (e.g. de los Reyes & Kennicutt, 2019; Bigiel et al., 2008). On the same note, taking only the molecular component that is more directly related to the SFR, spatially resolved studies found a value of $\sim$ 1 for N (e.g. Leroy et al., 2013; Shetty et al., 2014). In addition to this, while only considering the atomic component that is predominant in star-forming dwarf galaxies and low surface brightness galaxies, the value of N was found to be $N \sim 1.4$. This was true irrespective of whether the KS law was used with averaged values over galaxy disks or spatially resolved values (Please see Bigiel et al., 2010; Patra et al., 2016b; Roychowdhury et al., 2009, 2011, 2014; Wyder et al., 2009; Elmegreen & Hunter, 2015).

When looking at the average disk profile of a galaxy, there appears to be a threshold of 3-10 $M_\odot$ in the gas surface density, beyond which little to no star formation occurs. Kennicutt (1989) and Kennicutt Jr. (1998) found that when approaching this threshold from the centre of the galaxy, the value of N from the power law in Eqn. 1.3 becomes steeper than 1.4, and also coincides with the molecular-to-atomic transition zone in the disk. However, Boissier et al. (2007) did not find a steep decline in star formation at the threshold but rather showed an increase in the scatter.

This star formation density threshold can be explained using the Toomre criterion, which provides an expression for the critical density below which gas cannot collapse to form stars (Martin & Kennicutt, 2001). Other competing explanations include the ones by Schaye (2004), who explain the threshold as the radius with which the galaxy cold phase interstellar medium (ISM), a prerequisite for star formation, can form while Blitz & Rosolowsky (2004) focus on the gas density and argue that the threshold depends on the amount of molecular gas which is governed by hydrostatic pressure in the

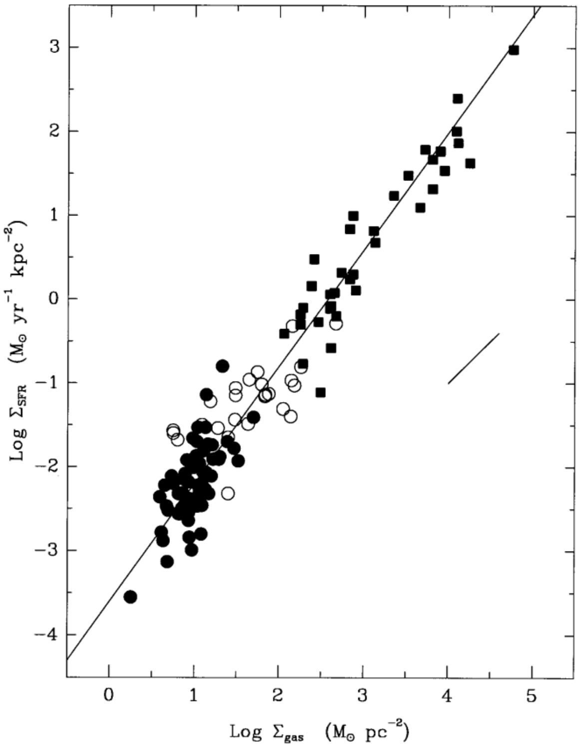

Figure 1.1: Star formation law for normal disk galaxies (filled circle) and starburst galaxies (squares). Open circles represent the centres of the normal disk galaxies, while the fit is shown in the graph as a solid black line.(Kennicutt Jr., 1998).

.

ISM.

To explain the star formation laws in Eqn. 1.3 and 1.2 Krumholz & McKee (2005) proposed a model in which the start of star formation occurs when the density of a molecular cloud rises to a point where its gravitational potential energy exceeds the kinetic energy of the turbulent motion within the cloud. When this happens, the cloud starts to collapse, and the collapsing material gets hotter and denser, eventually forming stars. This model makes analytical predictions at low gas densities of a downturn in both expressions due to a decreasing percentage of molecular gas with decreasing gas density.

This downturn exists at a threshold of ~ 9 $M_\odot$ pc^{-2} (Bigiel et al., 2008) where atomic hydrogen of higher surface density is converted to molecular gas. The atomic neutral hydrogen surface density measured at this saturation point differs by a factor of 10, or an order of magnitude, from the surface density measured at 1 $M_\odot$ pc^{-2} and thus forming the basis of the relationship between the H I size and mass.

However, Bacchini et al. (2019) found that the break in the slope seen in the Kennicutt law was a result of disc flaring rather than a drop in the star formation efficiency at low surface densities. They found this by building upon the first formulation of the star formation law proposed by Schmidt (1959a) as

$$\rho_{SFR} \propto \rho^n_{\text{H I}} \quad , \tag{1.3}$$

where ρ_{SFR} is the star formation rate per unit volume and $\rho^n_{\text{H I}}$ is the H I volume density. Assuming hydrostatic equilibrium, Bacchini et al. (2019) calculated the radial growth of the thickness of the gaseous disk, allowing them to convert the observed gas and SFR surface densities into deprojected volume densities and find a tight correlation between gas volume densities (H I + H_2) and SFR with the slope in the range of 1.3-1.9 and a significantly smaller scatter than the surface-based Kennicutt law.

1.2.2 HI size-mass relation

The relationship between a galaxy's size and mass, as determined by its amount of hydrogen gas, is known as the H I size-mass relation. The size has traditionally been represented by the disk radius at which the surface density profile drops below 1 $M_\odot$ pc^{-2} . This relationship was first parametrised by Broeils & Rhee (1997) as:

$$\log(D_{\text{H I}}) = 0.5\log(M_{\text{H I}}) - 3.32 \quad , \tag{1.4}$$

where $D_{\text{H I}}$ is the H I disk diameter in kpc, $M_{\text{H I}}$ is the H I mass in $M_\odot$ pc^{-2} and the scatter found to be as low as 0.1 dex. Wang et al. (2016) provided a revision of this relation using a sample of 562 galaxies with ranges of more than 10 B-band magnitudes and five orders of magnitudes in H I mass, as shown in Fig. 1.2, resulting in:

$$\log(D_{\text{H I}}) = (0.506 \pm 0.003)\log(M_{\text{H I}}) - (3.293 \pm 0.009) \quad . \tag{1.5}$$

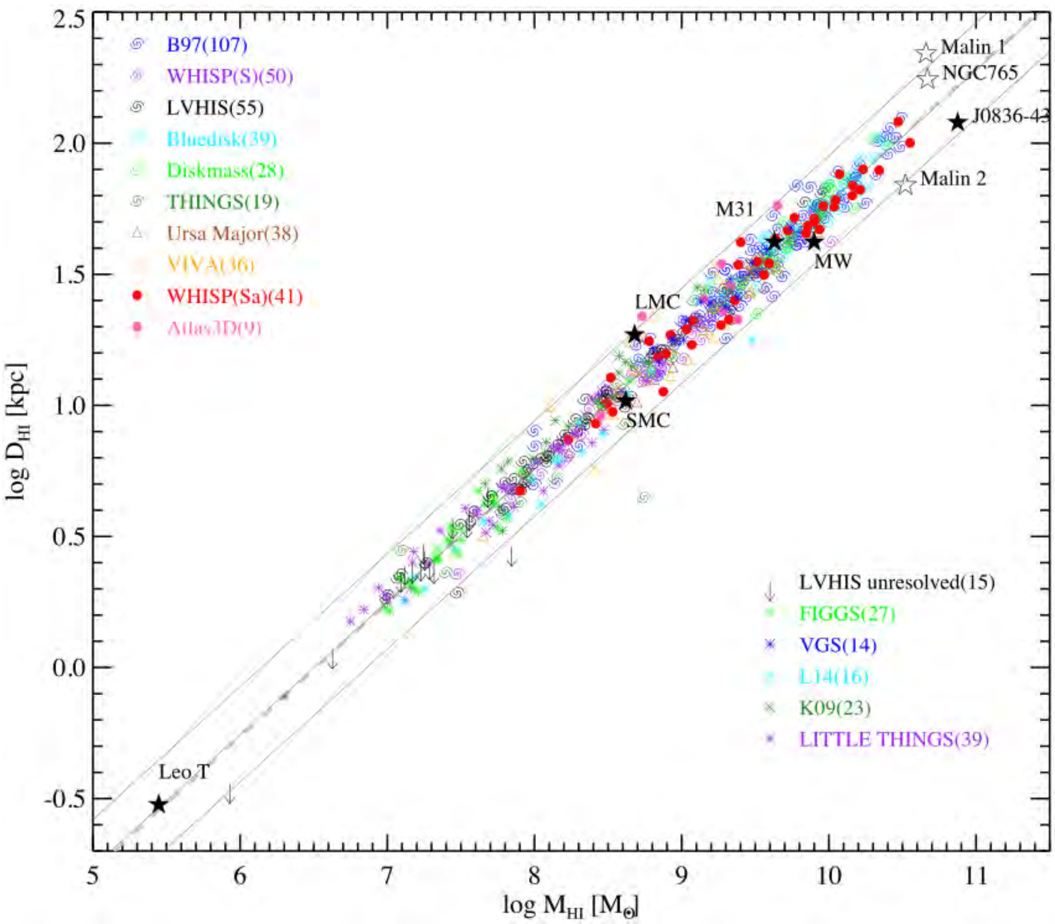

Figure 1.2: H I mass - size relation made from 562 galaxies by Wang et al. (2016). The solid line represents their best-fit line and the 3σ scatter, while the dashed line represents the fit by Broeils & Rhee (1997).

.

For comparison, Eqn. 1.4 is also shown in Fig. 1.2 as a dashed line. The scatter from this fit was found to be ~ 0.06 dex, about 14 per cent, with the 3σ shown in Fig. 1.2 as the two diagonal enclosing lines (Wang et al., 2016).

As mentioned above, the $D_{\rm H\,I}$ - $M_{\rm H\,I}$ relation has a small scatter. Since this relation was made using a wide range of galaxies, from spiral galaxies to dwarfs and early-type disc galaxies, this tightness in relation would be expected if these different galaxies had similar neutral atomic hydrogen gas surface densities ($\Sigma_{\rm H\,I}$) when normalised by radius. To further explore this, Wang et al. (2016) made $\Sigma_{\rm H\,I}$ radial plots of 9 surveys normalised by $R_{\rm H\,I} = D_{\rm H\,I}$ as shown in Fig. 1.3.

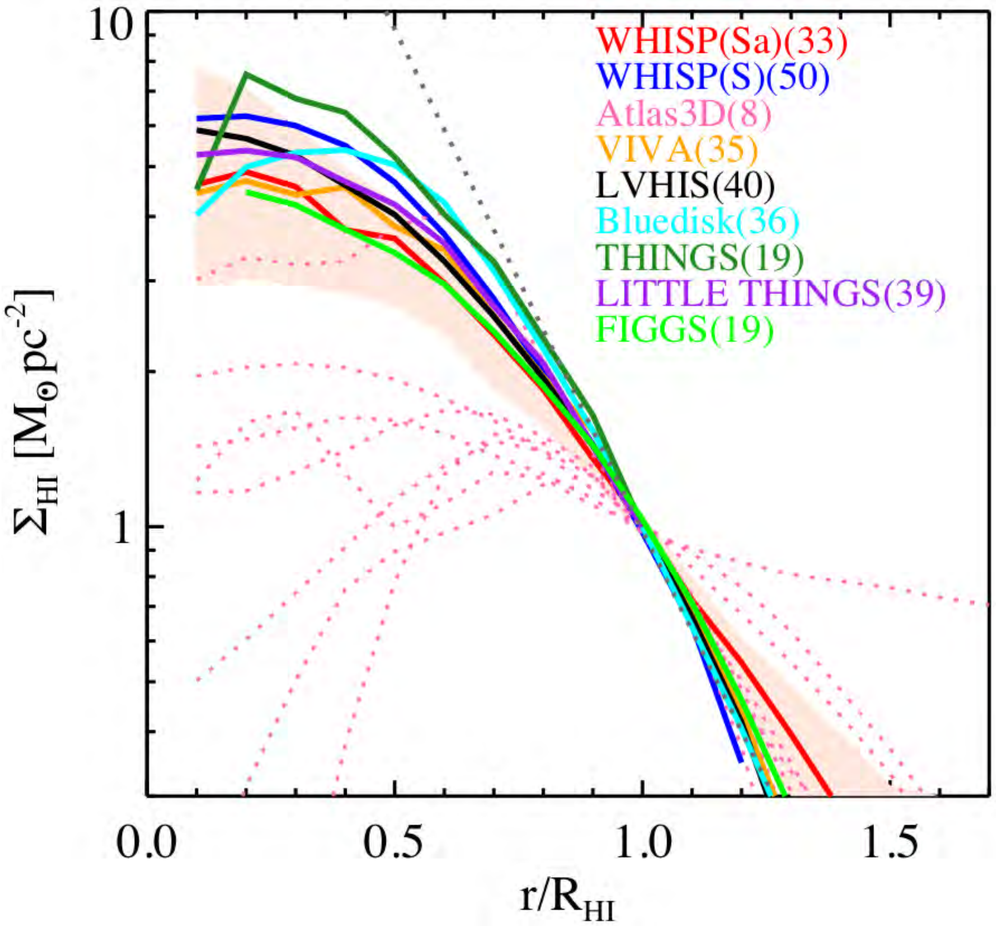

Figure 1.3: Normalized $\Sigma_{\mathrm{H\,I}}$ radial profiles of sample surveys. The median $\Sigma_{\mathrm{H\,I}}$ profiles of galaxies with diameters three times larger than the synthesized beam are shown except for ATLAS^{3D}, which shows individual profiles (Wang et al., 2016).

In fact, they found that the median profiles of both spiral and dwarf galaxies in the outer regions around the position of $R_{\mathrm{H\,I}}$ are similar and can be well described by an exponential function with a scalelength of $\sim 0.2\ R_{\mathrm{H\,I}}$ (Wang et al., 2013). This homogeneous nature of $\Sigma_{\mathrm{H\,I}}$ profiles for both spiral and dwarf galaxies suggests that both share a common mechanism that regulates the distribution of H I profile with radius. This is rather surprising because we expect the $\Sigma_{\mathrm{H\,I}}$ profiles to depend on the amount of H I gas present, which should depend on the H I to H_2 conversion process, which should vary widely with the galaxy type.

However, this $\Sigma_{\mathrm{H\,I}}$ is not always the same as the average $\Sigma_{\mathrm{H\,I}}$ as some galaxies, such as early-type galaxies, have a significant fraction of $M_{\mathrm{H\,I}}$ gas existing outside $D_{\mathrm{H\,I}}$ and hence, $D_{\mathrm{H\,I}}$ does not enclose the entire H I disk. Such early-type galaxies have a larger scale length, in units of $R_{\mathrm{H\,I}}$ compared to other galaxies and a lower $\Sigma_{\mathrm{H\,I}}$ in the inner region. This means that they have a rather extended H I distribution that is rather tenuous. This larger scale length hints at a different assembly history than dwarf and spiral galaxies and corresponds to recent accretion events.

This scenario is explained in galaxy formation models in a ΛCDM cosmology. In these models, gas being accreted onto early-type galaxies at later times acquires a larger angular momentum. This results in the gas settling on the outskirts of a disc plane much further away from the galaxy centre, hence a larger scale-length (Mo et al., 1998). Serra et al. (2014) observed kinematical misalignments between stars and H I gas, further confirming the external origin of H I gas in a large fraction of early-type disc galaxies.

The $D_{\rm H\,I}$ - $M_{\rm H\,I}$ relation has also been confirmed by subsequent surveys for late-type dwarf galaxies (e.g. Swaters et al., 2002; Begum et al., 2008a; Lelli et al., 2016), large spiral galaxies (e.g. Verheijen & Sancisi, 2001; Swaters et al., 2002; Wang et al., 2013; Ponomareva et al., 2016; Lelli et al., 2016), early spiral galaxies (e.g. Noordermeer et al., 2005) and irregulars (e.g. Lelli et al., 2016). Galaxies with extreme ratios of stellar mass to stellar scale length, or ultra-diffuse galaxies found in isolated environments, were also found to follow the H I mass size relation (Gault et al., 2021; Leisman et al., 2017). This relation has also been shown to hold in groups and clusters where we expect galaxies to lose H I through tidal interaction or ram-pressure stripping, provided that these galaxies' discs are not too disrupted and the diameter can be traced out to 1 $M_\odot$ pc^{-2}(Chung et al., 2009; Verheijen & Sancisi, 2001).

1.2.3 Tully-Fisher relation

There exists a relation between a galaxy's luminosity and circular disc velocity. This relation was first observed by Tully & Fisher (1977) using luminosity and the 21-cm H I line width of a sample of 10 galaxies. Tully & Fisher (1977) observed these galaxies exhibiting a positive correlation between the two variables. This correlation has been confirmed by several other observations, and explanations have been proposed to try to explain this correlation (e.g. Kannappan et al., 2002; Bell & de Jong, 2001; Pizagno et al., 2007). It has also been used as a distance indicator to galaxies (e.g. Tully & Fisher, 1977; Freedman et al., 2001; Tully & Pierce, 2000) and to provide constraints to galaxy formation models (e.g. Dalcanton et al., 1997; Navarro & Steinmetz, 2000).

Using luminosity in the Tully-Fisher relation in galaxy formation models comes with challenges. Specifically, when applying it to galaxy formation models, the slope changes with the observed wavelength or band. To apply the Tully-Fisher relation to these models hence becomes a challenge (Bell & de Jong, 2001). Meyer et al. (2008) observed the Tully-Fisher relation slope to steepen when longer wavelengths are considered; that is, a change of the slope as the observation bands changed from B to K bands. There were two proposed causes for this observed effect, namely the correlation between stellar population and luminosity and dust extinction and luminosity. When it comes to dust extinction, brighter galaxies in bluer bands have been observed to have a greater degree of dust extinction than galaxies observed in redder bands. If not taken into account, this effect flattens the observed Tully-Fisher relation at shorter wavelengths. Consequently, using the near-infrared wavelength to observe the Tully-Fisher relation yields the most accurate results, as the effects of dust extinction are minimised at these wavelengths. Considering the correlation between stellar population and luminosity, brighter galaxies tend to have older stellar populations, which have had more time to evolve and cool, resulting in their redder colour. Hence, brighter galaxies tend towards redder colours, and when observing at longer wavelengths, brighter galaxies appear more luminous than those observed at shorter wavelengths.

Bell & de Jong (2001) suggested a Tully-Fisher relation in which the stellar mass is used to replace luminosity. Removing the colour dependence in this way establishes a consistent way of comparing the slope in the Tully-Fisher relation in galaxy formation scenarios.

The stellar-mass Tully-Fisher relation has been a reliable correlation in determining galaxy distances and in galaxy formation models. This is true for circular velocities greater than 90 $\mathrm{km\,s^{-1}}$. However, when considering galaxies with lower rotation velocities than 90 $\mathrm{km\,s^{-1}}$, McGaugh et al. (2000) found a clear break in the optical Tully-Fisher relation; that is, all galaxies with circular velocities less than 90 $\mathrm{km\,s^{-1}}$ seemed to fall below the relation defined by brighter, faster-rotating galaxies. Such galaxies are under-luminous compared to the fit of the more rapidly rotating galaxies, as shown in Fig. 1.4.

These under-luminous galaxies tend to be gas-rich, and when considering both the stellar and gas mass of these galaxies, the Tully-Fisher relation is restored. The observed linear correlation continues down to the lowest mass galaxies. This suggests that the Tully-Fisher relation is fundamentally a relation between the total baryonic mass of the galaxy disc and the total rotation velocity and takes the form

$$M_b = AV_c^b \quad , \tag{1.6}$$

where log A $= 1.57 \pm 0.25$ and $b = 3.98 \pm 0.12$ (McGaugh et al., 2000). The total baryonic mass of a galaxy $M_b = M_* + M_{\mathrm{gas}}$ is considered to be a combination of the galaxy's stellar mass and gas mass. The total gas mass is taken to be the sum of H I , H_2 and He gas masses where He gas can be calculated assuming constant He to H I mass relation $M_{\mathrm{He}} = 0.33\ M_{\mathrm{H\,I}}$ (Bell et al., 2003). On the other hand, H_2 can be determined using the $M_{\mathrm{H_2}}/\ M_{\mathrm{H\,I}}$ ratios of Young & Knezek (1989). However, this ratio depend on the morphology of a galaxy, varying from 4.0 ± 1.9 for S0–Sa galaxies to 0.2 ± 0.1 for Sd–Sm.

Depending on the definition of rotation velocity, the Baryonic Tully Fisher relation (BTFR) changes significantly (e.g. Brook et al., 2016; Ponomareva et al., 2017; Lelli et al., 2019). Lelli et al. (2019), in an analysis of 175 spiral galaxies found in a comparison of different velocity conventions such as V_{flat}, the velocity measured at the flat part of the rotation curve, W_{50}, the velocity determined by integrating the H I spectrum,

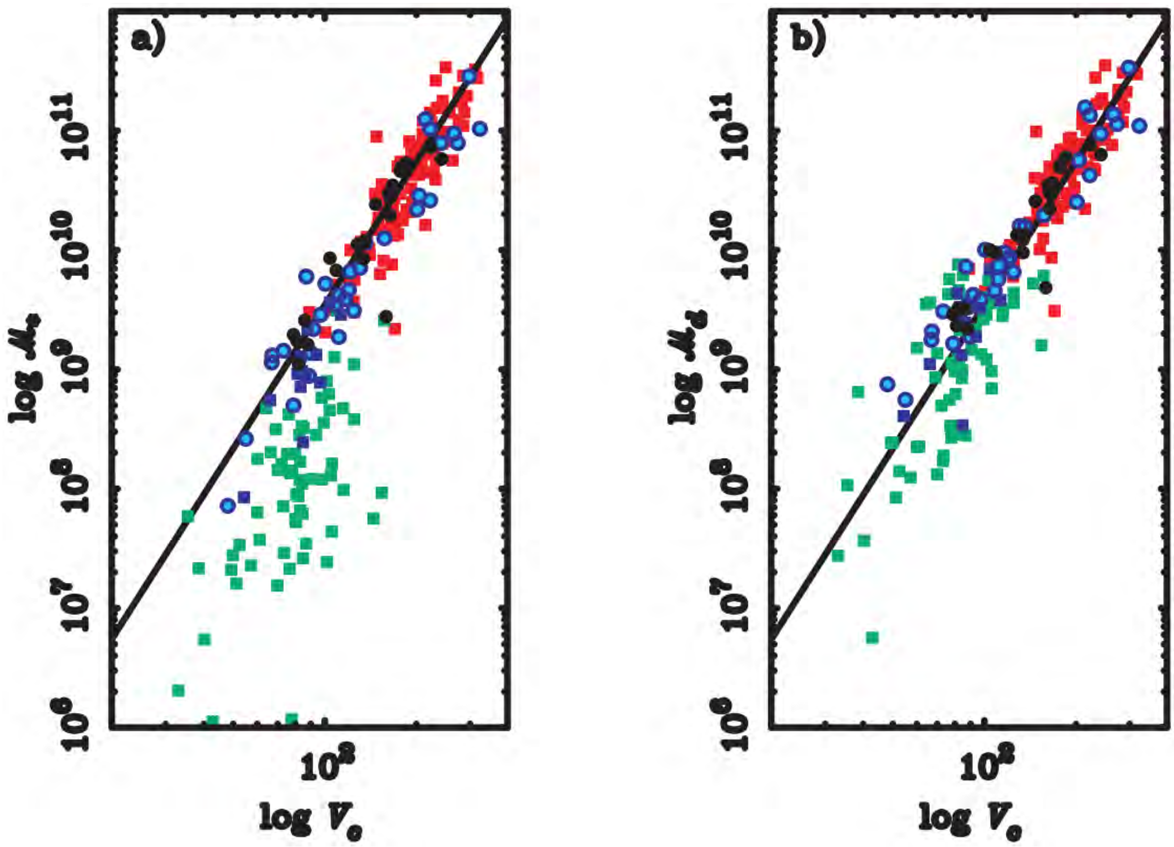

Figure 1.4: The Tully-Fisher relation for stellar mass (a) and baryonic disk (b) against rotation velocity by McGaugh et al. (2000). The squares represent galaxies where the circular velocity has been estimated from the line-width $V_c = \frac{1}{2}W_{20}$ while the circles represent galaxies whose circular velocity has been estimated from the flat portion of the galaxy's rotation curve $V_c = V_{\rm flat}$.

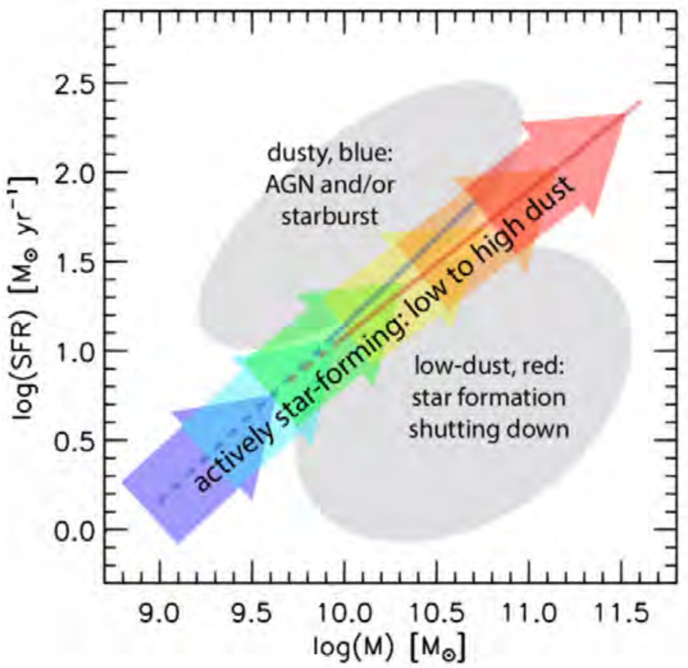

Figure 1.5: Cartoon illustration of how star-forming galaxies are distributed in the $\log(SFR) - \log(M_*)$ plane (Whitaker et al., 2012).

.

and V_{max}, the maximum rotation velocity from the rotation curve, that the tightest and steepest slope for the BTFR was provided by V_{flat}.

Therefore, the optical Tully-Fisher relation approximates this more fundamental relation. The fact that the Tully-Fisher relation holds implies that the mass-to-light ratio holds across different stellar populations. Therefore, the relation can be used to determine the mass of a galaxy given its rotation velocity, irrespective of its stellar population. The low scatter observed in the Tully-Fisher relation also implies that the Initial Mass Function must be nearly universal to achieve the observed uniform mass-to-light ratio. This relation has also been found to be stable and unaffected by galaxies' environments (Mocz et al., 2012), implying it can be used across different galaxy environments.

1.2.4 The Star Formation Sequence

A useful scaling relation observed in galaxies is the relationship between the stellar mass and the star formation rate (SFR). This is because galaxies show a correlation between these two quantities from redshifts $z \sim 0$ out to $z \sim 7$ (Whitaker et al., 2012). To illustrate this, Whitaker et al. (2012) categorised galaxies into four categories, three of which are shown in Fig. 1.5.

As Fig. 1.5 shows, there are three distinct locations in the $\log(SFR) - \log(M_*)$ plane in which galaxy populations tend to cluster . A fourth one is not shown in the figure. One cluster represents actively star-forming galaxies with normal colours and associated LIR/LUV ratios, i.e. from low to high dust content. These occupy the coloured band arrows in the figure and consist 54% of the total population (Whitaker et al., 2012). The second most abundant population is the quiescent galaxy population (28%) for $\log(M) > 10$ at $1.0 < z < 1.5$, consisting of galaxies that have little to no ongoing star formation and are not shown in the figure. These galaxy populations are followed by the red star-forming galaxy population (11%), which has low dust content (LIR/LUV ratios) and for which star formation is shutting down. Finally, the blue, dusty star-forming galaxies with high (LIR/LUV ratios) and specific star formation rates (7%) form another distinct population.

Whitaker et al. (2012) notes that the star formation sequence is not linear with SFR $\propto M_*^{0.6}$ and a constant scatter of 0.34 dex. However, exclusively blue galaxies do show a linear relation. This correlation can be described in the form of a power law.

$$\log(\mathrm{SFR}) = \alpha(z)(\log M_* - 10.5) + \beta(z) \qquad , \tag{1.7}$$

where

$$\alpha(z) = 0.70 - 0.13z \qquad , \tag{1.8}$$

$$\beta(z) = 0.38 + 1.14z - 0.19z^2 \qquad , \tag{1.9}$$

where β is the normalization while α is the slope. The slope of this power law can be used to determine the efficiency with which a galaxy is converting gas into stars and, hence, the star formation efficiency (SFE) (e.g. Polak et al., 2023; Ghodsi et al., 2024; Teng et al., 2024). This slope can be used to determine the SFR of a given galaxy, assuming the stellar mass is known or vice versa.

On average, galaxies belonging to the star formation sequence were forming stars at a higher rate in the early universe as compared to today, with a decrease of the SFR by a factor of ~ 30 from $z \sim 2$ to $z \sim 0$ (Daddi et al., 2007) and a seemingly constant SFR from $z \sim 2$ to $z \sim 7$ (González et al., 2010). Generally, galaxies tend to maintain a balance between the rate at which cold gas is accreted onto a galaxy and feedback, thereby affecting star formation (Bouché et al., 2010; Dutton et al., 2010). The slope of the star formation sequence may be affected by feedback, while the change in normalization with redshift is generally thought to be from the evolution of gas densities with redshift (Dutton et al., 2010). This normalization β decreases from $z \sim 0$ to $z \sim 2$ by a factor of 4 and the global SFR density by a factor of 6 (Hopkins et al., 2006).

1.2.5 Mass-metallicity relation

Galaxy evolution can be modelled as a balance between gas inflow into a galaxy and the outflow of gas from the galaxy. This gas flow leaves a galaxy in a state of equilibrium, with gas inflow balancing the outflow of gas over time and hence, the "equilibrium" or "bathtub" models of galaxy evolution. In these models, the outflow of gas is typically driven by processes like star formation, the ejection of gas from the galaxy through supernovae or other explosive events, while the inflow of gas into the galaxy is typically driven by processes like the accretion of intergalactic gas or the inflow of gas from the galaxy's own halo, while the halo gets its gas from the cosmic web (Sánchez Almeida et al., 2014)

This class of models has been shown to successfully predict the mass-metalicity relation (MZR) and its evolution, as well as the fundamental metallicity relation (FMR) (e.g. Peeples & Shankar, 2011; Davé et al., 2012; Lilly et al., 2013). The mass-metallicity relation (MZR) refers to the positive correlation between the gas-phase oxygen abundance (O/H) and stellar mass M_* (e.g. Tremonti et al., 2004; Lee et al., 2006; Lequeux et al., 1979; Andrews & Martini, 2013) while the FMR refers to the secondary dependence of MZR on star formation rate (SFR) such that there is a three-parameter relation among SFR, M_* and O/H (e.g. Ellison et al., 2008; Mannucci et al., 2010; Curti et al., 2020).

These relations have been shown to change with redshift. In particular, within the local universe at $z \sim 0$, the MZR at low masses ($M < 10^{10}$) is usually described by a power law that becomes asymptotic at high masses. From $z \sim 0$ to $z \sim 2.5$, the MZR slowly and steadily drops, making O/H 0.3 dex lower than at $z \sim 0$ at fixed stellar mass (Savaglio et al., 2005; Maiolino et al., 2008; Erb et al., 2006; Sanders et al., 2015); followed by a rapid metallicity evolution, a drop of 0.3-0.4 dex from $z \sim 2.5$ to $z \sim 3.5$ despite these redshifts being separated by only 1 Gyr (Mannucci et al., 2009; Onodera et al., 2016). On the other hand, the FMR has been shown to depend secondarily on the SFR up to $z \sim 2.3$ (Sanders et al., 2018), while experiencing an offset of 0.1 dex out to $z \sim 2.5$ according to some studies (Cresci et al., 2019; Curti et al., 2020). However, the FMR does not appear to be valid at redshifts $z > 3$ with metallicities 0.3-0.6 dex below predicted values (Onodera et al., 2016).

Changes in the MZR at low masses could be attributed to more effective material removal by outflows at lower stellar mass according to the bathtub models (Tremonti et al., 2004; Lilly et al., 2013) as the metal-rich gas is ejected from the disc of the galaxy into the halo, and eventually rains back down to the disc, cooling and replenishing the interstellar medium with new material (Davé et al., 2011).

1.3 Gas Accretion

In order to sustain star formation in galaxies, H I gas needs to accrete from the IGM as shown in Fig. 1.6. This accretion happens in two modes. The cold mode with T $\sim 10^4$ K occurs in low-mass galaxies (with halo mass of $M_h \leq 10^{11}$ $M_\odot$) that exist in low-density environments and the 'hot mode' with T $\sim 10^6$ K is common in high mass galaxies (with halo mass of $M_h \geq 10^{11}$ $M_\odot$) that reside in high-density environments (e.g. Dekel et al., 2009; Kereš et al., 2005). In the 'hot mode', the H I gas is shock-

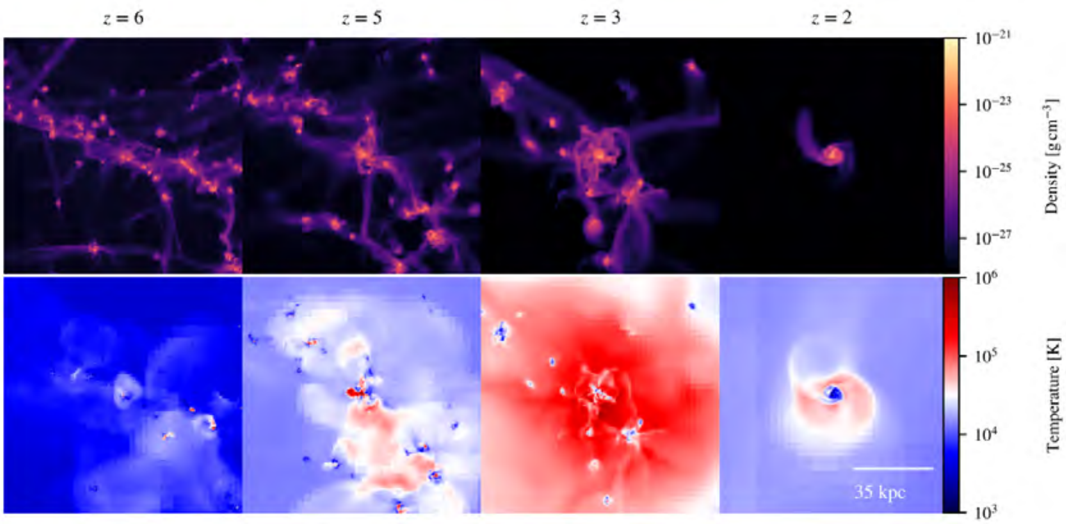

Figure 1.6: Simulations showing temperature (bottom) and gas density (top) of a galaxy at different redshifts. At higher redshifts, the galaxy gets its gas directly from the cosmic web via filamentary accretion, while at low redshifts, there is a hot halo that feeds the galaxy with gas from larger distances. (Kocjan et al., 2023).

.

heated as it enters the dark matter halo and becomes part of it. The time scales for this gas to cool radiatively and eventually settle onto the galactic disk are extremely high (Rees & Ostriker, 1977). On the other hand, in the 'cold mode', the gas accretes into a galaxy's disk along filaments, directly entering the galaxy's disk. Kinematic evidence of gas accretion onto galaxies is rare. However, there has been indirect evidence of accretion onto galaxies (Putman, 2017), e.g. extra-planar H I clouds and lopsided, warped or extended H I disks and the observations of H I filaments and tails around galaxies (e.g. Xu et al., 2021; Sancisi et al., 2008a; Leisman et al., 2016; de Blok et al., 2014).

Star-forming galaxies appear to have their gas accretion and gas removal processes at equilibrium (e.g. Noeske et al., 2007; Bouché et al., 2010; Lee et al., 2015). However, for gas deficient galaxies in group environments, gas accretion on to the galaxies suppressed while the galaxy's interstellar medium is removed resulting in a fast decline of the star formation rate and consequently, galaxy quenching. As a galaxy's gaseous halo is removed through ram-pressure stripping or tidal interactions, gas accretion onto the cold H I disk is suppressed, resulting in galaxy starvation or strangulation (Larson et al., 1980; Balogh et al., 2000) and therefore contributing to galaxy evolution.

1.4 H I emission and absorption lines

In the accretion process, H I gas cools down to the cold neutral medium (CNM) temperatures ($T \sim 100$ K), forming molecular hydrogen H_2 which eventually forms stars given sufficient mass. In order to understand this process in detail, it becomes important to study the physical conditions of the intervening gas, or the interstellar medium (ISM) phases, two such phases being the Cold Neutral Medium (CNM) and the Warm Neutral Medium (WNM).

H I 21-cm absorption line observations have been instrumental in determining the ISM phases. The cold neutral medium (CNM; $T \sim 100$ K) can be easily traced using the 21-cm H I absorption line, making it possible to trace out its evolution with redshift and, therefore, shed light on the SFR density evolution with redshift. H I 21-cm, OH 18-cm and metal absorption lines can also be used to place constraints on the variation in the fundamental constants of physics such as the proton-to-electron mass ratio, proton gyromagnetic ratio and the fine structure constant (e.g. Wolfe et al., 1976; Chengalur & Kanekar, 2003; Srianand et al., 2010; Kanekar et al., 2012; Rahmani et al., 2012; Gupta et al., 2018). In addition to this, precise 21-cm absorption line observations obtained over multiple epochs can be used to measure cosmic acceleration by determining the magnitude of the redshift drift for a galaxy at a given redshift (Darling, 2012).

For these reasons, H I and OH absorption features at $0 < z < 5$ have been the subject of many studies. However, technical limitations imposed by narrow bandwidths and hostile radio frequency interference environments made the majority of the effort be directed towards environments with higher chances of detection. Such environments include galaxies with quasar sightlines at small impact parameters or distance between the quasar sightline and foreground galaxy ($\rho < 30$ kpc), quasar sightlines with a Damped Lyman-alpha (DLA) (DLA with $N_{\rm H\,I} \geq 2 \times 10^{20}{\rm cm}^{-2}$) and a strong Mg II absorption line. However, given that these preselection methods rely on optical and ultraviolet spectroscopic surveys, they tend to be biased against sight lines through dense molecular clouds in the ISM. While some optical and ultraviolet measurements have shown that cold atomic and molecular gas can be detected in low column density absorbers ($10^{19} \leq N_{\rm H\,I} \leq 2 \times 10^{20}{\rm cm}^{-2}$) or at large impact parameters $\sim 50 - 80$ kpc (e.g. Neeleman et al., 2017), the statistical detections of H_2 absorption at $z \sim 3$ is ~ 25 times less than that of H I (Balashev & Noterdaeme, 2018; Zwaan & Prochaska, 2006). However, the detection rate of cold gas is significantly higher in strong DLAs indicative of higher column densities $N_{\rm H\,I} \geq 5 \times 10^{21}{\rm cm}^{-2}$, which probe galaxies at small impact parameters (Noterdaeme et al., 2014; Ranjan et al., 2018, 2020). This implies that cold gas is preferably located at small impact parameters, the very same regions that would experience strong dust bias for optically selected quasars, leaving these regions largely unexplored (Krogager et al., 2019).

Combining emission and absorption studies of the Milky Way reveals that a significant fraction ($\sim 20 - 50\%$) of the H I gas exists in the thermally unstable region of $T_k \sim 500 - 5000$ K, suggesting that a dynamical process such as supernovae, magnetic fields or turbulence, may be driving the gas from stable to the unstable phase (Audit & Hennebelle, 2005; de Avillez & Breitschwerdt, 2005).

Beyond the Milky Way and beyond our local universe, as motivated earlier, it becomes more difficult to observe H I 21-cm gas in emission, but it can be detected in absorption in the foreground of a bright continuum source or an Active Galactic Nuclei (AGN) independent of the distance . Depending on the AGN impact parameter to the galaxy, different regions in and around galaxies can be explored, such as the interstellar medium in the galactic disk, the extended HI disc, inflows to the galaxy and outflows from the galaxy, high-velocity clouds, or even the Circumgalactic medium (CGM). Given the small cross-section probed by absorption line studies, in order to trace out the structure of CGM, it would need a sizeable sample of pairs of foreground galaxies and background AGNs, which would enable us to map the distribution in a statistical manner. Such studies have shown that the CGM or the galaxy halo is an important component of a galaxy and observing different gas phases can be useful in placing constraints on the galaxy formation and evolution models.

There have been several surveys conducted within redshifts $z < 0.4$ and that have small impact parameters of (≤ 50 kpc) from the background radio quasar (e.g. Carilli & van Gorkom, 1992; Gupta et al., 2010; Borthakur, 2016; Zwaan et al., 2015; Reeves et al., 2016; Dutta et al., 2017b). One such study by Dutta et al. (2017a) found a weak ($\sim 3\sigma$) anti-correlation between the optical depth and impact parameter. The covering fraction also seemingly declines with increasing impact parameter with an average incidence of $\sim 20\%$ within 30 kpc for an optical depth of $\int 0.3$ dv km s^{-1}. Close to the major axis, the optical depth is found to be larger, suggesting that the gas is co-planar with the extended H I discs of galaxies since, in this case, the physical distance from the centre of the galaxy is smaller along the major axis than the minor axis for the same impact parameter.

A common practice used to search for 21-cm H I absorption lines is by selecting and using foreground sources that are responsible for the Mg II absorption lines observed in the spectra of the background AGN. Mg II doublet lines, $\lambda 2796, \lambda 2803$ have been used to extensively study galactic haloes of $z \leq 2$ galaxies (e.g. Bergeron, 1986; Steidel et al., 1994; Churchill et al., 2000; Chen et al., 2010; Nielsen et al., 2013; Rubin et al., 2018; Dutta et al., 2020, 2021). Using these Mg II systems to make H I absorption line observations in the redshift range $z \leq 1.5$, is crucial as it is the range over which the global star formation rate declines and the Lyman-α line cannot be observed from the ground. However, H I studies of samples of strong Mg II absorbers have shown that the detection rate of 21-cm H I absorption line is $\sim 10 - 20\%$ for a sensitivity of $\int \tau \, \mathrm{dv} = 0.3$ km s^{-1}. This detection rate has been found to remain constant within the redshift range $0.3 < z < 1.5$ (Gupta et al., 2012; Dutta et al., 2017a).

It is also possible to improve the chances for H I detections by observing Damped Lyman-α absorption. Damped Lyman-α absorbers generally refer to clumps of H I typically found in the redshift range $2 < z < 4$ and with a corresponding column density of $N_{\mathrm{H\,I}} \geq 2 \times 10^{20}$cm^{-2} for Damped Lyman-α absorbers (DLAs) and $N_{\mathrm{H\,I}} \sim 10^{19} - 2 \times 10^{20}$ cm^{-2} for sub-DLA. There have been several efforts (e.g. Rao et al., 2011; Péroux et al., 2012; Fumagalli et al., 2015; Chengalur et al., 2015; Srianand et al., 2016; Krogager et al., 2017; Kanekar et al., 2018; Mackenzie et al., 2019) to connect the properties (e.g., column density) of Damped Lyman-α systems to the properties of their host galaxy (Star formation rate, stellar mass, atomic and molecular mass). From such attempts, it has been found that DLAs are generally found in high metallicity galaxies at a higher success rate and are generally thought to be associated with faint, gas-rich galaxies.

DLAs are also an important source of information regarding the physical conditions of the neutral gas in galaxies towards the radio-loud quasars. A key quantity is the temperature of the 21-cm H I gas. There has been a number of DLA studies (e.g. Wolfe et al., 1985; Carilli et al., 1996; Chengalur & Kanekar, 2000; Kanekar et al., 2003; Curran et al., 2010; Srianand et al., 2012; Kanekar et al., 2014) which have indicated that the fraction of cold gas detected by 21-cm H I absorption in the redshift range $z > 2$ is low with a detection rate of $\sim 20\%$ for a sensitivity of $\int \tau dv = 0.3$ km s^{-1}. This low detection rate is consistent with the low molecular H_2 fraction seen in such DLAs (Noterdaeme et al., 2008). Upon investigating the spin temperature by comparing $N_{\rm H\,I}$ from Lyman-α absorption to $N_{\rm H\,I}$ from the 21-cm H I absorption, it has been found that a significant fraction of H I in $z \geq 2$ traces the WNM as well as having high values of the spin temperature T_s. There also exists an anti-correlation between the observed WNM and the metallicity at $z \geq 2$, hinting at fewer radiative cooling routes. The spin temperature T_s also shows a redshift evolution, with T_s at $z \leq 2.4$ being significantly different from that of $z \geq 2.4$ as well as that of the Milky Way (Kanekar et al., 2014). A larger number of DLAs at $z > 2.4$ have $T_s \geq 1000$ K, and the detection frequency of DLAs from $z < 1$ to $z > 2$ is found to decrease by a factor of 3, implying that the cold gas fraction of the universe declines with cosmic time.

Given the benefits derived from H I absorption lines, they also suffer from a disadvantage. Only the region with a sufficiently bright background continuum source can be studied, meaning that only a few galaxies with one or two chance alignments can be studied. Only the Milky Way can be studied along many sight lines. Another disadvantage is that the (H I) column density estimates from H I absorption line depend on the excitation or spin temperature (T_s) and the covering factor, which is a fraction of the continuum source that is covered by the absorbing gas (f_c). The column density is directly proportional to the spin temperature T_s and inversely proportional to the optical depth-integrated over the 21-cm H I absorption line velocity $\int \tau$dv km s^{-1}.

$$N_{\rm H\,I}[\mathrm{cm}^{-2}] = 1.823 \times 10^{18} T_s[K] \int \tau \mathrm{dv}[\mathrm{kms}^{-1}] \quad . \tag{1.10}$$

From Eq. 1.10, the optical depth τ corrected for covering factor (f_c) is given by Eq. 1.11

$$\tau = -\log[1 - \frac{\Delta S}{(f_c S)}], \tag{1.11}$$

where S is the flux density of the background continuum source while Δ S is the absorption line depth. Given an optically thin gas, Eq. 1.10 reduces to:

$$N_{\rm H\,I}[\mathrm{cm}^{-2}] = 1.823 \times 10^{18} \frac{T_s[K]}{f_c} \int \frac{\Delta S}{S} \mathrm{dv}[\mathrm{kms}^{-1}] \quad , \tag{1.12}$$

Assuming a covering factor $f_c = 1$, it is possible to constrain the spin temperature (T_s) by comparing the 21-cm absorption $N_{\rm H\,I}$ column density to the independently derived

21-cm H I emission column density (e.g. Kanekar et al., 2001; Dutta et al., 2016), the X-ray absorption derived column density (e.g. Allison et al., 2015; Moss et al., 2017) or the Lyman-α derived absorption column density (e.g. Srianand et al., 2012; Kanekar et al., 2014). However, each of these techniques has its own disadvantages. The 21-cm H I emission line can only be detected for local galaxies up to a redshift of $\sim z < 1.3$, and the angular scales for emission would be much larger than the angular scales needed for absorption studies. Deriving the total H I column density from X-rays assumes that the X-ray and H I spectra trace the same sight line through the gas. Similarly, a fundamental assumption when comparing H I and Lyman-α in absorption is that the sight lines traced by both spectra are aligned, and they trace the same gas phase.

In situations where the assumption that the covering factor (f_c) is one fails, it is possible to constrain the covering factor by making high spatial resolution (milliarcsec or parsec scale) observations using the Very Large Baseline Interferometry (VLBI) observations. However, due to the limited frequency capabilities of the VLBI, such observations would be limited to only a few sources at low redshifts (e.g. Morganti et al., 2013; Srianand et al., 2013a; Biggs et al., 2016). Vice versa, assuming that the core of the radio source is aligned with the optical source, it is also possible to constrain f_c by comparing the core component flux density observed at high spatial resolution using VLBI to the total flux density obtained from a lower spatial resolution observation (arcsec or kiloparsec scales).

1.5 Galaxy Parametrisation

When studying H I in galaxies, it is required to quantify the properties that describe such galaxies. This quantification could be in the form of both geometrical or morphological, as well as kinematic characteristics. The description and the measurement of these parameters is often only briefly discussed as they are considered common knowledge. It should be noted, however, that might sometimes lead to a certain degree of misinterpretation. To prevent this, a more comprehensive introduction of the parametrisations used in the following chapters shall be added here.

1.5.1 Galaxy orientation (in H I)

The orientation of the H I disk of a galaxy is often described using the position angle (PA), as well as the inclination (i). The position angle of the H I disk is referred to as the angle between the north and the galaxy's major axis on the approaching side of the H I disk measured counterclockwise, as shown in Fig 1.7.

The inclination is the angle between the plane of the galaxy and the line of sight from the observer to the galaxy such that a galaxy observed face-on is said to have an inclination angle of 0° while a galaxy observed edge-on is said to have an inclination angle of 90° . This is illustrated in Fig. 1.8.

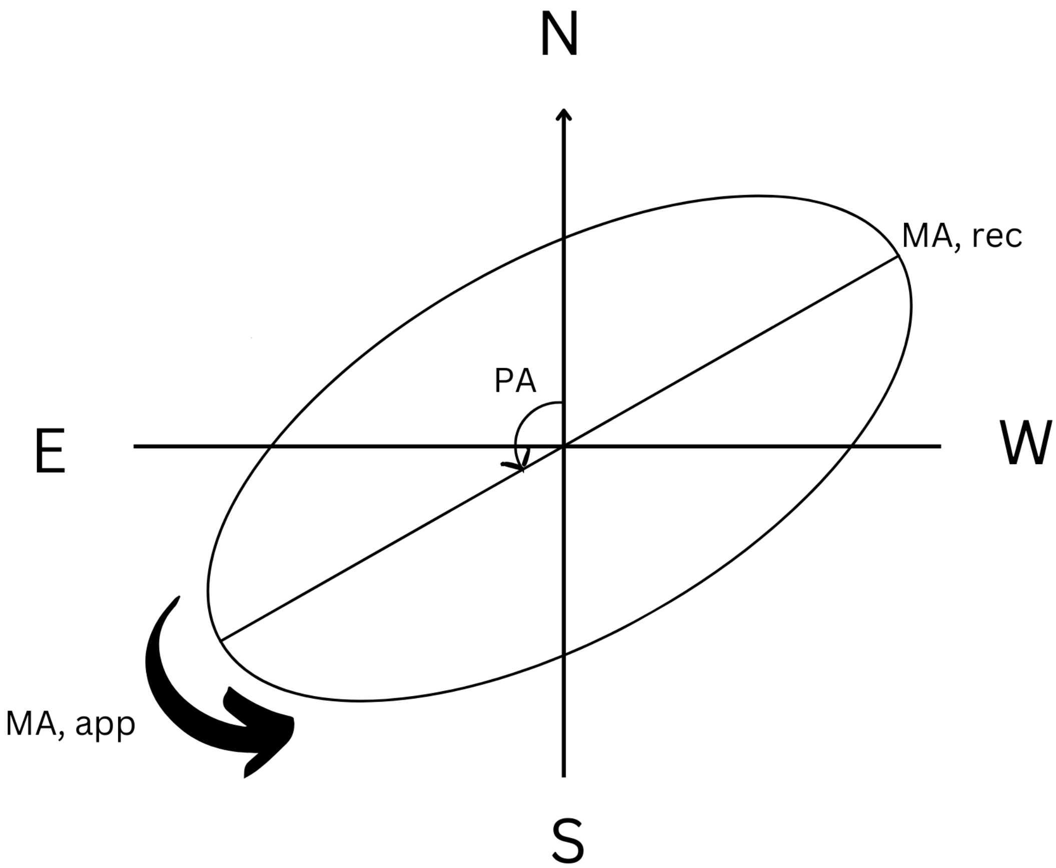

Figure 1.7: Position angle measured from North counterclockwise to the approaching side of the major axis.

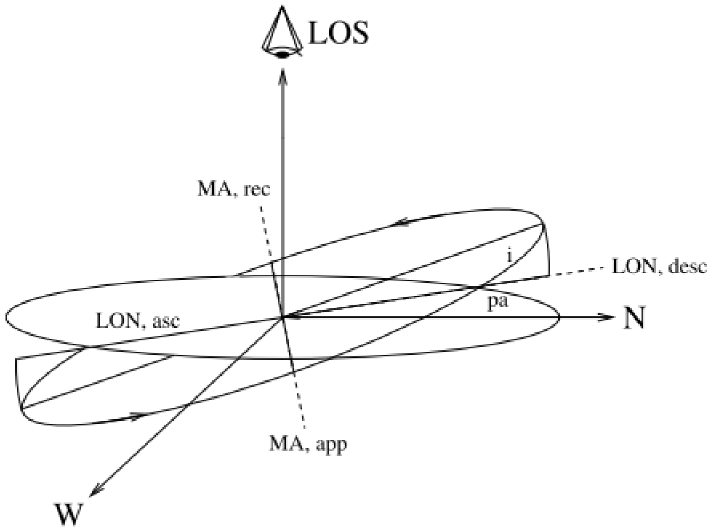

Figure 1.8: Inclination angle denoted as i from Jozsa et al. (2007)

.

Complementary to the geometric properties of the H I disk are their kinematic properties, such as rotation velocity and dispersion. These properties form the basis for kinematic analysis using spectroscopy to study and understand the dynamics of galaxies in different environments. This, in turn, enables us to understand the structure and distribution of matter in galaxies, as well as acting as a useful aid in studying interactions involving galaxies.

1.5.2 Moment analysis

A first reduction of the information available from observed data cubes is often made in a so-called moment analysis. By calculating moments, usually of up to second order, one can learn about the distribution and dynamics of the gas in the galaxy or other observed objects. Several different statistical moments can be calculated, including the integrated flux density and velocity dispersion hereafter referred to as moment 0 and 2 maps. Moment 1 maps represent the line of sight velocity in a rectangular coordinate system. The following subsections will talk about how these moment maps are calculated or made.

1.5.2.1 Moment 0 or H I intensity maps

Taking a spectroscopic data cube where the neutral H I intensity is represented by values S_j in each pixel with a spectral width ΔV and j is the pixel number, the moment 0 map can be calculated by integration along the spectral axis. Numerically, this is realised as a sum of the products of S_j and ΔV in one spatial pixel of the data cube.

$$I_{\text{H I}} = \Sigma_j S_j \times \Delta V \qquad , \tag{1.13}$$

where $I_{\text{H I}}$ represents a single pixel's value in the resulting moment 0 map with the units of Jy km s^{-1} beam^{-1} . This moment 0 map represents the total content of neutral hydrogen 21-cm H I and can be converted to the total column density map.

$$\frac{N_{\text{H I}}}{\text{cm}^{-2}} = \frac{1.104 \times 10^{24}(1+z)^3}{b_{maj} \times b_{min}} \times I_{\text{H I}} \quad , \tag{1.14}$$

where z is the redshift of the galaxy; b_{maj}, b_{min} the major and minor axes of the spectroscopic data cube's restoring beam, respectively, and $N_{\text{H I}}$ the column density in atoms per centimetre squared.

1.5.2.2 Moment 1 maps or velocity fields

Velocity fields can be extracted from spectroscopic data cubes using a variety of techniques, each having its merits as well as disadvantages depending on the signal-to-noise levels in the data cube as well as the emission structure.

The simplest method involves determining and selecting the peak positions of the velocity profiles for every spatial pixel. However, this technique is sensitive to noise as, if the signal-to-noise ratio is low, the selected peak position could be a mere artefact of noise and, therefore, not representative of the peak velocity profile of the observed object in that cube. A way to mitigate this challenge posed by noise involves calculating the Intensity Weighted Mean (IWM), or moment 1, for all pixels in the spatial coordinates and using this as the substitute for the velocity fields. The IWM of a velocity profile can be calculated:

$$< V >= \frac{\Sigma_j S_j \times V_j}{\Sigma_j S_j} \quad , \tag{1.15}$$

where $< V >$ is the intensity-weighted average velocity. Despite being a potential solution to mitigate the effects of noise, it can suffer from systematic errors when the velocity profile is skewed. To be specific, when using a skewed velocity profile, the calculated IWM will be offset from the maximum value towards the skewed side as demonstrated by Swaters (1999) in Fig. 1.9.

As demonstrated in Fig. 1.9, using a Gaussian fit to the velocity profile results in a better fit to the peak of the profile, as compared to the moment 1 calculation, especially when the profile is skewed. The Gaussian fit also stands to be more robust against noise, unlike the moment 1, as seen in Fig 1.9 (b) and as would be expected when there are low signal-to-noise ratios. However, when the signal-to-noise ratio is low, and the skewness of the velocity profile is low, the two fits can be approximately similar.

For skewed velocity profiles or those with elongated tails, an even more robust means of determining the peak of the profile intrinsic to the observed target is to fit a Gauss-Hermite curve or multiple Gaussians (e.g. Oh et al., 2018). These are the techniques used to make velocity fields, leading us to the final diagnostic map, normally used in the literature; the velocity dispersion maps.

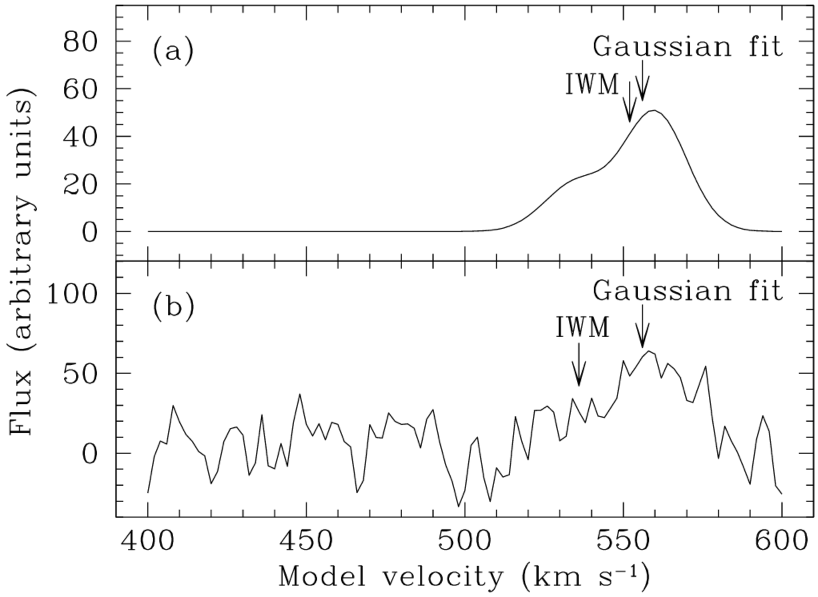

Figure 1.9: Comparison between the IWM and a Gaussian fit for both smooth (a) and noisy (b) velocity profiles. The Gaussian profile determines the peak value more accurately than the IWM (Swaters, 1999)

.

1.5.2.3 Moment 2 or velocity dispersion maps

Moment 2 maps represent the total velocity dispersion in galaxies. The velocity dispersion of a galaxy refers to the random motions of the contents of H I gas in galaxies. These maps can be calculated following Eqn. 1.16

$$\sigma_{\rm mom2} = \sqrt{\frac{\Sigma_i S_i \times (V_i - < V >)^2}{\Sigma_i S_i}} \quad . \tag{1.16}$$

$\sigma_{\rm mom2}$ can ideally be identified with the intrinsic dispersion in the observed target. This, however, requires a careful analysis, as both projection, as well as beam-smearing effects can play a role. Principally, higher-moment analyses of data cubes are possible, but as their systematical and statistical uncertainties increase with order, the dispersion or the second moment is usually the highest-order velocity information used in the analysis of galaxies or other astronomical objects.

1.5.3 Kinematic Parametrisation

The moment maps described above are instrumental in some kinematic parameterizations, specifically velocity maps. These velocity maps, as well as velocity dispersion maps characterizing the recession velocities of the atoms and molecules in the observed object, and by extension, the rotation velocity as a function of radius, can be determined using a galaxy's spectra. The recession velocity refers to the velocity with which a galaxy is moving away from the observer, the velocity dispersion being the random motions observed in galaxies, while the rotation velocity is the tangential velocity of

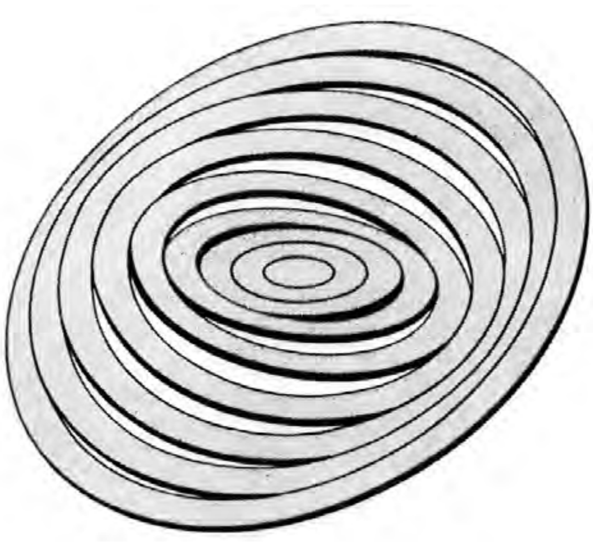

Figure 1.10: A representation of the tilted-ring model representing M83 from Rogstad et al. (1974).

.

the galaxy contents around the centre of the galaxy. As a galaxy rotates, the H I 21-cm emission from the galaxy experiences differential Doppler shifting as a direct consequence of the galaxy's rotation. This fact enables us to determine the line of sight velocity of different parts of the galaxy, ranging from the centre out to the edge and therefore determine the galaxy's rotation curve. The rotation velocity as a function of radius is called a rotation curve. Since neutral hydrogen extends further than the optical disk of galaxies, we can trace the rotation curve to larger radii, allowing us to probe the mass distribution out to larger radii, which also allows us to study the angular momentum and dark matter properties of galaxies.

Observations have confirmed that the orbits in disk galaxies without large bars have a low ellipticity (Schoenmakers et al., 1997) and can hence be approximated as circular. These circular orbits also exhibit characteristic warps at large radii where the gravitational restoring forces of the inner disk become weak. Consequently, to 0th order, the disk material's kinematics can be described as a set of three parameters, namely rotation velocity, position angle and inclination; the latter two describe the orbit's orientation with respect to a given reference. This description is called a 'tilted-ring' model, a model consisting of a set of concentric rings with relative orbital velocities to each other and in different inclinations relative to the central planes as shown in Fig. 1.10. One possibility to also describe deviations from this symmetry is to expand the tilted-ring model in a harmonic analysis (Schoenmakers et al., 1997).

1.5.3.1 The Tilted-ring model

Rogstad et al. (1974) used the tilted-ring model to successfully explain the observed deviation from co-planar motion in the H I disk of M83 and henceforth explained it as a warp in the disk structure modelled by this set of concentric rings. The tilted-ring model is based on the assumption that most of the galaxy's mass is in orbit along a given plane, the galaxy's disk, and is, therefore, a suitable model for a spiral galaxy. However, it can be an oversimplification when there are strong non-circular motions such as the case for NGC 2976 (Simon et al., 2003) or a bar (Bosma, 1978a) and would not be suitable for elliptical type galaxies without a disk as the majority of motion would be random and not confined to a disk. As discussed above, the tilted-ring model can be seen as a 0th-order approximation, which can be employed for a large class of galaxies.

The tilted-ring model can be made using two approaches. The first approach involves constructing a velocity field as discussed in section 1.5.2, then later fitting a tilted-ring model to this velocity field. A modern application of this method is represented by "2D Bayesian automated tilted-ring fitting of disc galaxies in large H I galaxy surveys" (2DBAT, Oh et al. (2018)). The second approach involves making a parameterized simulated spectroscopic data cube whose basis is the tilted-ring model and iteratively fitting it to an observed cube until the fit converges. This second approach forms the basis for three-dimensional fitting techniques implemented in software such as TiRiFiC[1] and the Fully Automated TiRiFiC (FAT[2]) (Jozsa et al., 2007; Kamphuis et al., 2015). These two approaches are discussed in detail in the following subsections.

1.5.3.2 Two dimensional fitting

After going through the procedure described in section 1.5.2 to derive the moment 1 or velocity field, one ends up with a map where each velocity component in each pixel represents the line-of-sight velocity ($V_{los}(x, y)$) at each point (x, y) in a Cartesian coordinate system. The method has been described by Begeman (1987). From this, it is possible to determine the rotation velocity ($V_{rot}(r)$) of the galaxy under the assumption of a tilted-ring geometry, which would entail decomposing the line-of-sight velocity at each radius r into its constituent terms as well as translating the Cartesian coordinate system to the polar coordinate system inherent to the tilted-ring model. In the first step, the line-of-sight velocity is decomposed into harmonic terms, the first approximation excluding other non-rotational motions aside from systemic or recessional velocity (V_{sys}) as shown in Eqn. 1.17

$$V_{los}(x, y) = V_{sys} + V_{rot}(r)\cos\theta\sin i. \tag{1.17}$$

When the velocity in the radial direction, or the expansion velocity ($V_{exp}(r)$) is included,

$$V_{los}(x, y) = V_{sys} + \sin i(V_{rot}(r)\cos\theta + V_{exp}(r)\sin\theta). \tag{1.18}$$

The second step comes in when the (x, y) coordinate of the galaxy is translated to polar coordinates (r, θ) following Eqn. 1.19 and 1.20

[1] http://gigjozsa.github.io/tirific/
[2] https://github.com/PeterKamphuis/pyFAT-astro?tab=readme-ov-file

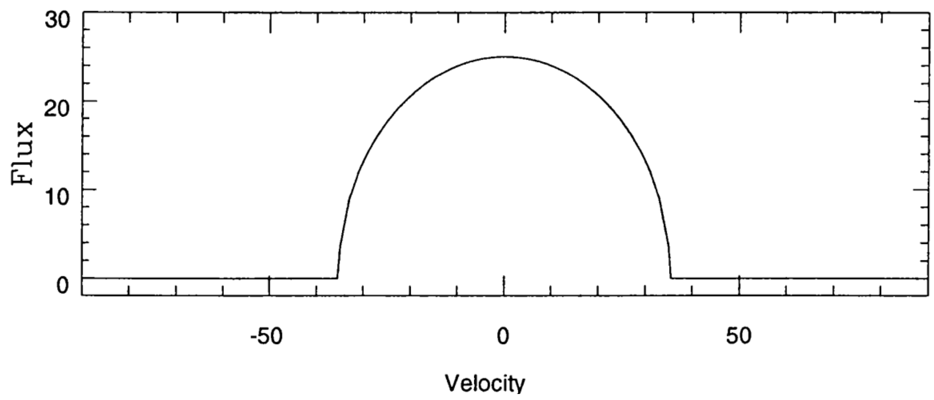

Figure 1.11: Global profile of a galaxy with a uniform solid body distribution of H I gas with a maximum rotation speed of 50 $\mathrm{km\,s^{-1}}$ (Skillman, 1996).

.

$$\cos\theta = \frac{-(x-x_c)\sin\phi + (y+y_c)\cos\phi}{r} \tag{1.19}$$

$$\sin\theta = \frac{-(x-x_c)\cos\phi - (y-y_c)\sin\phi}{r} \quad , \tag{1.20}$$

where r is the distance from the galaxy's centre, (x_c, y_c); θ, the azimuth angle measured counterclockwise from the galaxy's major axis in the disk plane, and ϕ is the position angle of the galaxy and i is the inclination angle of the galaxy disk.

In summary, as seen from Eqns. 1.17 and 1.18, the line of sight velocity $(V_{los}(x,y))$ can be decomposed into the rotation velocity $(V_{rot}(r))$, systemic velocity (V_{sys}) and expansion velocity $(V_{exp}(r))$. It is important to note that the contribution of the rotation velocity component $(V_{rot}(r))$ to the line of sight velocity $(V_{los}(x,y))$ becomes zero along the minor axis of a galaxy. This also happens when a galaxy's inclination approaches zero, i.e., when a galaxy is being observed face-on.

As the inclination angle increases, the contribution to the measured line-of-sight velocity from the rotation velocity increases, resulting in the characteristic double-horned profile. This double-horned spectral profile is a consequence of the differential rotation shown by larger galaxy disks.

Interestingly, Skillman (1996) also noted that the distribution of H I gas could influence the shape of the H I global profile, an example being a solid body galaxy whose H I distribution falls off as the inverse of the radius, shown in Fig. 1.12 or a solid body galaxy with uniform H I distribution over the entire disk, shown in Fig. 1.11.

Once the rotation velocity has been successfully determined, the next step is done by fitting a tilted-ring model to this velocity map with the aim of deriving the aforementioned kinematic and morphological parameters.

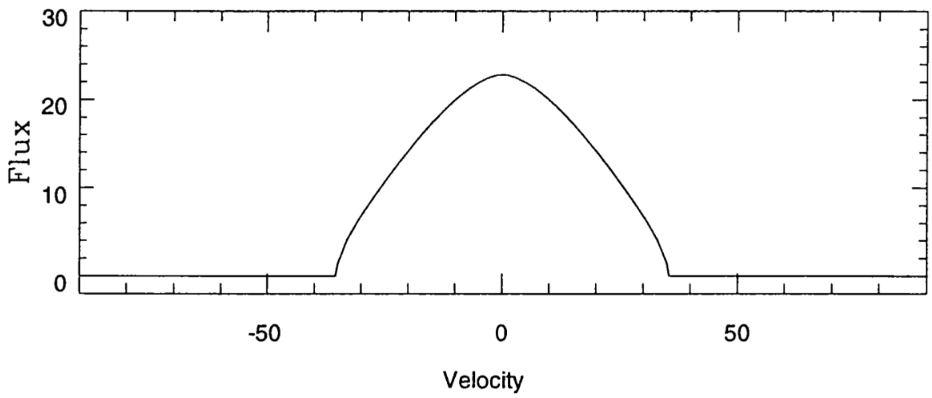

Figure 1.12: Global profile of a solid body galaxy with a maximum rotation speed of 50 km s^{-1} and whose distribution falls off as the inverse of the radius (Skillman, 1996).

.

There are several software options to fit a tilted-ring model to a velocity field. The most commonly used is the ROTCUR routine (Van Albada et al., 1985); implemented in NEMO, GIPSY, and AIPS, among others, which fits a set of inclined rings, the tilted-ring model, to a velocity field. There are also a number of variants of the ROTCUR routine, among them the GIPSY routine RESWRI, which performs a harmonic decomposition of the line-of-sight velocity along the azimuthal angle tracing the projected ellipse of a ring. This can be used to study the effect of non-axisymmetric potentials on the kinematics of the rotating disk (Binney, 1978; Franx et al., 1994; Teuben, 1991). RINGFIT (Simon et al., 2003) also allows for azimuthal variations in the rotation velocity, but in the context of a flat disk and has been used by Simon et al. (2005) to check the reliability of their rotation curves. ROTCURSHAPE, implemented in NEMO (Teuben, 1995), performs a global fit of the velocity field in which the ring parameters are not fitted independently, but rather all at once. On the other hand, KINEMETRY (Krajnović et al., 2006) reduces higher-order terms in a harmonic expansion in order to find the best-fitting solution for a tilted-ring model. A more recent approach includes 2DBAT (Oh et al., 2018). 2DBAT is a Bayesian method for fitting tilted rings to the velocity field of disc galaxies in large H I surveys in order to study their rotation and structural properties.

These two-dimensional-based fitting techniques usually benefit from their low computational cost while fitting for the tilted-ring model. However, they have their shortcomings, including projection effects such as beam smearing. The projection effect adversely affects this method when the target galaxies are either seen edge-on or have large warps. This is because the line-of-sight intersects the disk twice or more, making it impossible to derive a single representative velocity field from such a galaxy even if its geometry is known. Beam smearing is another limitation encountered by the 2-dimensional based fitting algorithms. This limitation has been demonstrated by Bosma (1978b) before by comparing low-resolution H I velocity field maps observed by single dishes to H I high-resolution velocity field maps made by interferometers. They were able to show how beam smearing makes the velocity gradients towards the centre a little bit flatter, mimicking a solid body rotation while, at the same time, converting bits

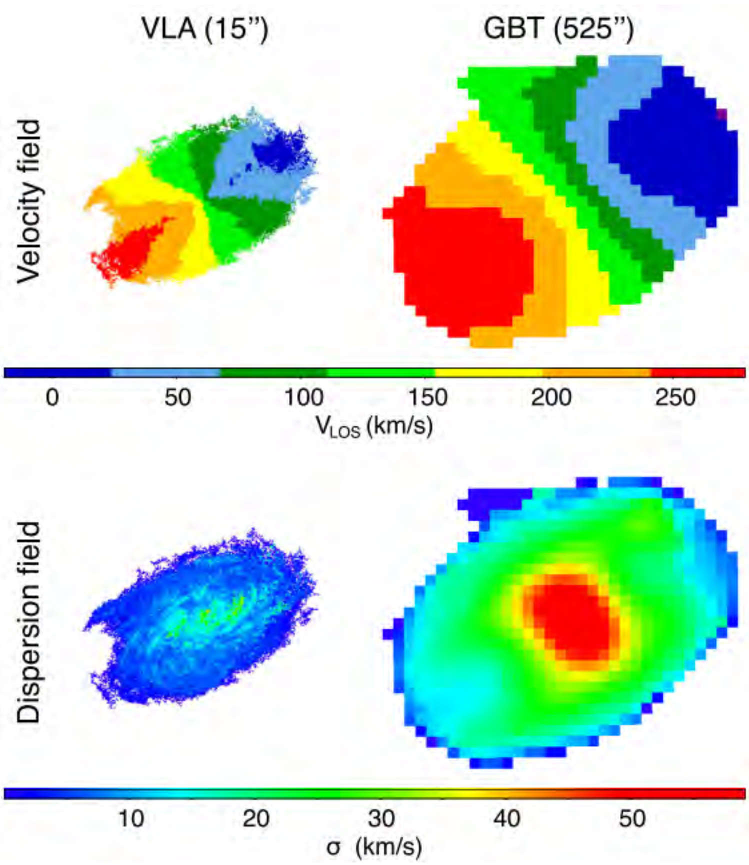

Figure 1.13: Comparison between the velocity fields (Top) and dispersion velocities (bottom) for NGC2403's observations using a single dish (GBT, right) and interferometer (VLA, left) in an effort to show the effects of beam smearing (Di Teodoro & Fraternali, 2015).

.

of this rotation velocity to dispersion velocity. This has a direct effect on the central regions of the velocity dispersion maps, showing an increase in velocity dispersion, as shown in Fig. 1.13.

Beam smearing is referred to as the effect a finite beam has on the derived velocity field. In detail, when fitting a rotation curve to a velocity field of a galaxy, the rotation velocities may be underestimated in regions where the rotation curve is rising and overestimated in regions where it is falling. This bias towards regions of higher surface brightness is due to the fact that when the measured intensity is not constant over the beam area, the measured velocity profile at a given position is a convolution of the beam with the true intensity distribution, causing asymmetry in the 'smeared' profile. This means that the resulting 'smeared' profile becomes asymmetric as regions with higher intensities contribute more to it. Hence, the maximum position is dragged toward velocities with greater associated surface brightness. This is the case even if the observed velocity profile would have been symmetric had it been observed with a pencil beam.

Beam smearing is not easy to address because it also depends on how velocities change within the beam. To mitigate the impact of beam smearing, a section of the velocity field is often excluded from the analysis (by specifying a "free angle"), and data points are weighted. An extreme choice for a free angle would be only to consider velocities along the major axis of the galaxy and correct for inclination, which is equivalent to extracting a rotation curve from a long-slit observation. While this improves results in the outer parts of the galaxy, it worsens them in the inner parts. This necessitates either utilizing three-dimensional methods to analyze low-resolution single-dish data or using interferometers to observe galaxies at high resolution.

1.5.3.3 Three dimensional fitting

As an alternative to using velocity fields, three-dimensional fitting techniques exist that make use of all information in spectroscopic data cubes to create the tilted-ring model. In general, they have as an input a set of morphological and kinematic parameters that describe a disk, which they use to construct a simulated data cube as their initial model. Once these parameters are supplied and a simulated cube is made, the simulated cube then becomes convolved with an artificial observational beam, approximated as a Gaussian, whose major and minor axes resemble the observations. These convolved cubes are compared to the original using Chi-Square, and model parameters are adjusted in response. This process continues in a loop until the best model parameters describing the tilted-ring model are found; that is, the simulated cube becomes as similar as possible to the observed cube.

This method of deriving the tilted-ring parameters has the advantage over two dimensional methods in that it is less affected by both projection effects and beam smearing. The benefit results from fitting the tilted-ring model directly to the spectroscopic data cube, from which the parameters characterizing the ring model are obtained. This method of fitting becomes more reliable because it does not require the construction of velocity fields where information is lost. The other advantage that comes from this method is the possibility to model kinematic asymmetries as well as warps in galaxies and galaxies that are nearly edge-on or face-on, as well as, depending on the implementation, extraplanar gas.

As mentioned above, due to their sensitivity to extremely faint features, 3D models can greatly outperform those obtained from a velocity field. Even if a galaxy's H I disk is substantially warped, it shows a significant change in the projected centre of rotation. Whether a galaxy is seen edge-on or is intersected by the line of sight more than twice, the software can still successfully recover the parameters. In addition to the orientational parameters and the rotation curve, it also provides the analyzed galaxy's surface-brightness profile. There are several 3D tilted-ring codes in use such as TiRiFiC, Jozsa et al. (2007); 3DBAROLO, Di Teodoro & Fraternali (2015); FAT, Kamphuis et al. (2015).

FAT (Fully Automated TiRiFiC; Kamphuis et al., 2015) is an automated procedure that fits the tilted-ring model to H I data cubes by building on the Tilted Ring Fitted Code (Jozsa et al., 2007). To be specific, it starts by applying SoFiA source finder (Serra et al., 2015) to the input cube to get the initial parameters for this source. Thereafter, it automatically initializes TiRiFiC using these parameters and then iteratively applies TiRiFiC, sometimes with increasing complexity, until a satisfactory fit is achieved. FAT begins with a flat disc model where the fitted parameters are independent of the radius but has the functionality to explore radial variations in these parameters. Should one proceed with fitting parameters that vary with radius, at the end of the fit, these radial variations are smoothed by a polynomial fit to avoid artificial fluctuations from TiRiFiC, with differences between smoothed and unsmoothed returned as uncertainties for some parameters. FAT can reliably model the geometry and kinematics of H I disks with an extent of eight beams across the major axis and inclinations ranging from 20° to 90° Kamphuis et al., 2015.

On the other hand, 3DBAROLO (Di Teodoro & Fraternali, 2015) is a tilted-ring code similar to FAT, the key differences being the parameter initialisation, model optimisation and flux normalisation. When it comes to initialising parameters, 3DBAROLO can use its built-in source finder based on DUCHAMP (Whiting, 2012) or the user can specify the initial parameters directly. Once the source(s) are found, the Nelder-Mead algorithm (Nelder & Mead, 1965) is used to optimise the model on a ring-by-ring basis, and the beam effects are applied by convolving each velocity channel with a 2D kernel. During model optimisation, the radial variations of the geometric parameters can be computed using a number of techniques, such as Bezier interpolation, and polynomial fits or can return median values if a flat disk model is specified. Flux normalisation is done in 2D using the observed moment 0 map on an azimuthal ring or pixel-by-pixel basis, and uncertainties are estimated using a Monte Carlo approach, where some model parameters are varied around the best fit until the residuals increase by $\sim 5\%$. 3DBAROLO can recover H I disc parameters that are resolved by as few as 2 beams along the major axis while the inclination ranges from 45° to 75°. In the following, we refer to a specific implementation of the tilted-ring model, TiRiFiC (Jozsa et al., 2007).

In order to create a TiRiFiC tilted-ring model, a set of parameters that vary with radius and a set of global parameters are needed. The set of parameters belonging to a given radius is referred to as a “ring”. To calculate a model, these ring-specific parameters are linearly interpolated to form a number of sub-rings with a user-specified width. Then, using a Monte Carlo integration, these sub-rings are modelled to rotate with the same tangential velocity and a specific orientation with respect to the observer, which is determined by the position angle and inclination. After that, the model is projected onto a cube whose dimensions are determined by the input data cube and later convolved with a 3D-Gaussian, representing the internal dispersion in a galaxy’s tracer material as well as the instrumental effects of a finite observing beam and finite resolution in the frequency domain.

With regard to the ring-specific parameters, the user supplies the radius, circular velocity, scale height, surface brightness, inclination, position angle, as well as the (central) right ascension, declination and systemic velocity of the rings. It is important to note that the position angle in TiRiFiC is measured from the meridian to the minor axis counterclockwise, with the north being zero degrees and the East at ninety degrees left. On the other hand, the global parameters supplied by the user include the global isotropic velocity dispersion, including instrumental dispersion, a parameter that accounts for the vertical distribution of the gas density, the total flux of a single point source or cloud where the number of Monte-Carlo point sources is roughly equal to the model's total flux divided by this quantity. In order to keep the flux of the subring accurate, the cloud flux is changed by a tiny fraction when calculating point sources for a subring. It is this point source model that is gridded into a model cube and convolved with a 3D Gaussian as described above. This 3D Gaussian is simply a product of 2D (anisotropic) Gaussian, representing the observing beam (CLEAN beam) of the input cube and can be defined by the user, and a 1D Gaussian representing the total velocity dispersion.

1.5.4 Vertical structure of H I disks

The kinematic and morphological parametrisation methods discussed in section 1.5 can be used to determine the 3-dimensional structure of a galaxy. However, it is also possible to do the same by numerically solving the joint Poisson-Boltzman equation of the hydrostatic equilibrium of the stellar, atomic and molecular gas components of a galactic disk and considering the external force contribution from the dark matter halo (Patra et al., 2014; Banerjee & Jog, 2008; Banerjee et al., 2010; Narayan & Jog, 2002). Taking a constant vertical gas velocity dispersion of 8 $\mathrm{km\,s^{-1}}$ as a function of radius, Banerjee & Jog (2008) estimated the vertical scale heights for four dwarf galaxies from the FIGGS Survey and found them to have thick H I disks that flare out as a function of radius. This was observed to be true even when taking a varying velocity dispersion with radius, an example being Patra et al. (2016b) who modelled 23 dwarf galaxies from the LITTLE THINGS survey and found that dwarf galaxies had a scale height that varied from a few hundred parsecs at the centre to a few hundred-kilo parsecs towards the edge. This variation in the scale height also holds for spiral galaxies modelled using a varying vertical velocity distribution (e.g. Patra et al., 2016a) who modelled 8 spiral galaxies from the THINGS survey and found the spiral galaxies H I scale height increasing from a few hundred parsecs at the centre to $\sim 1-2$ kpc at the edge.

1.6 The MeerKAT Absorption Line Survey

H I observations by single dish surveys have been used to provide reliable measurements of integral properties of the H I in galaxies, like mass and velocity width, and consequently statistical information like the H I mass density (Zwaan et al., 2005). Previous single dish H I surveys can be grouped into the southern and northern hemisphere surveys. The H I Parkes All-Sky Survey (HIPASS; Barnes et al., 2001; Meyer et al., 2004) surveyed the southern hemisphere while the Northern HIPASS catalogue (NHICAT; Wong et al., 2006), and the Effelsberg Bonn H I Survey (EBHIS; Kerp et al., 2011) surveyed the northern hemisphere. The Arecibo Fast Legacy ALFA survey (ALFALFA; Giovanelli et al., 2005) and the H I Parkes All Sky Survey (HIPASS; Meyer et al., 2004) have been instrumental in measuring the global H I properties of nearby galaxies such as the distribution function of galaxies as a function of H I mass or the H I Mass Function (HIMF) (e.g. Martin et al., 2010; Zwaan et al., 2003; Haynes et al., 2011). These single-dish surveys have aided in determining various aspects of the HIMF, such as the contribution of different galaxy populations to the HIMF (e.g. Dutta & Khandai, 2021) as well as the HIMF environmental dependence (e.g. Jones et al., 2018a; Moorman et al., 2014; Said et al., 2019). Other aspects determined by single dish measurements are the H I velocity width function (e.g. Moorman et al., 2014), scaling relations of the atomic gas component (e.g. Catinella et al., 2010, 2013) as well as the H I selected galaxies' clustering (e.g. Martin et al., 2012; Guo et al., 2017).

In order to understand the details of the structure and dynamics of nearby galaxies, spatially resolved observations are required. To this end, there have been several spatially resolved H I emission surveys such as the Faint Irregular Galaxies GMRT survey (FIGGS; Begum et al., 2008b), the Local Volume H I survey (LVHIS; Koribalski et al., 2018), The H I Nearby Galaxy Survey (THINGS; Walter et al., 2008), Survey of H I in Extremely Low Mass Dwarfs (SHIELD; Cannon et al., 2011) as well as the Local Irregular Galaxies That Trace Luminosity Extremes, The H I Nearby Galaxy Survey (LITTLE THINGS; Hunter et al., 2012). SKA pathfinder surveys have also been used to study thousands of spatially and spectrally resolved galaxies. The MeerKAT H I Observations of Nearby Galactic Objects; Observing Southern Emitters survey (MHONGOOSE; de Blok et al., 2016) aim to detect H I at low column densities in an attempt to probe the connection between galaxies and the intergalactic medium in nearby, well-resolved galaxies. On the other hand, The MeerKAT International GigaHertz Tiered Extragalactic Exploration survey (MIGHTEE; Maddox et al., 2021) is a medium-wide, medium-deep survey that aims to extend our knowledge of H I emission to $z = 0.6$ and therefore enable us to study the evolution of H I over the past 5 billion years as well as explore H I as a function of galaxy environment given that there are massive groups and galaxy clusters within its survey volume. In addition to these surveys, The Widefield ASKAP L-band Legacy All-sky Blind Survey (WALLABY; Koribalski et al., 2020) aims to survey three-quarters of the sky to a redshift of $z \leq 0.26$ in an attempt to study the influence of the environment on galaxy evolution in groups and clusters, while the Apertif surveys (Verheijen et al., 2009) consists of a large-area, medium deep imaging of H I with the aim to investigate the connections between the gas and total mass distribution of galaxies as well as investigate how these connections vary with environment and what role gas accretion and removal play.

Since the flux density scales with distance squared, and the H I mass function limits the H I masses of galaxies to a maximum of 10^{11} $M_\odot$, the range of observations of H I in emission is limited to the local universe. The most sensitive observations to date are conducted in the MeerKAT's LADUMA survey, with an expected redshift limit of $z = 1.4$ (Blyth et al., 2016) and widefield surveys, such as the H I emission project within the MeerKAT International GHz Tiered Extragalactic Exploration (MIGHTEE) survey and the FAST all sky H I survey (FASHI), have much lower redshift limits (Verheijen et al., 2007; Catinella et al., 2008; Maddox et al., 2021; Zhang et al., 2024).

Taking H I 21-cm observations in the local universe and combining them with Lyman alpha absorbers (Lyα) at high redshifts can also enable constraining the H I mass density, $\Omega_{\rm HI}$ of the universe in the redshift regions $z < 0.2$ and $2 < z < 4$. Comparing the H I mass density to the SFR density over the same redshift range, there is a modest decrease of $\Omega_{\rm HI}$ (factor of 2) compared to the order of magnitude decrease in the SFR necessitating direct observation of cold atomic and molecular gas in order to understand the processes that lead to the conversion from cold atomic to molecular and eventually to stars (Crighton et al., 2015; Neeleman et al., 2016).

Therefore, 21-cm H I absorption becomes necessary to complement emission line observations and trace the evolution of the atomic gas component of galaxies since 21-cm absorption is not limited by distance, only by the flux density of the background source. It can also be used to trace circumnuclear disks (Gallimore et al., 1999; Struve & Conway, 2010; Morganti et al., 2011), reveal infalling clouds potentially related to the feeding of supermassive black holes (Morganti et al., 2009; Maccagni et al., 2014; Tremblay et al., 2016) and trace outflows which could potentially indicate the interaction between jets and the surrounding interstellar medium (Aditya & Kanekar, 2018; Schulz et al., 2021).

When it comes to wide field surveys, the First Large Absorption Survey in H I (FLASH; Allison et al., 2022) utilizes the Australian Square Kilometre Array Pathfinder (ASKAP) telescope's wide field of view and large spectral bandwidth to search for H I absorption lines in the radio spectra of bright continuum sources that belong to intervening 21-cm absorbers associated to host galaxies of radio sources at $0.4 < z < 1.0$. The aim is to provide valuable kinematical information for models of gas accretion and jet-driven feedback in radio-loud active galactic nuclei.

The MeerKAT Absorption Line Survey (MALS) is designed to use the MeerKAT's UHF and L-band receivers to carry out sensitive ($N_{\rm H\,I} > 10^{19}{\rm cm}^{-2}$) dust-unbiased search for intervening H I and OH absorption lines at $0 < z < 2$. This is because the observables associated with H I and OH absorption lines, as well as the volume filling factor of the interstellar medium phases, depend on in situ star formation through various stellar feedback processes. Consequently, observations of H I and OH over the redshift range of the survey provide reliable measurements of the evolution of cold atomic and molecular gas cross-sections of galaxies, as well as aiding in understanding the evolution of the Star Formation Rate (SFR) density with redshift. To this end, these intervening absorbers detected from the survey are important for a variety of science themes as discussed in Gupta et al. (2017), with this thesis focusing on the third theme titled Galaxy Evolution through H I and OH Emission. This theme aims to conduct a substantial blind emission line survey with the aim of detecting thousands of galaxies in order to study the distribution and kinematics of atomic and molecular gas in galaxies and, therefore, provide insights into the gas content and dynamics of galaxy disks and their relation to star formation processes.

1.7 Thesis outline

This thesis makes use of the MALS H I absorption and emission line observations to derive H I properties of galaxies in two galaxy groups, Klemola 31 and UGC 439 with the aim to understand the processes that govern galaxy formation and evolution. It examines not only anomalous cold H I gas in the galaxies but also the effects of group environments. Chapter 2 discusses the Klemola 31 galaxy group, starting with a description of our observations, data reduction, and source finding. Thereafter, it explores the HI morphology and kinematics of this group. Chapter 3 focuses on the UGC 439 galaxy group and organizes it in a similar manner. A summary and comparison of the two groups is presented in Chapter 4.

Chapter 2

HI 21-cm Emission and Absorption of Galaxies in the Klemola 31 Group

This chapter is an adaption of Maina et al. (2022), the publication of which was part of the PhD project on which this thesis is based. It presents a detailed H I 21-cm absorption and emission line study of the Klemola 31 galaxy group using data from the MeerKAT Absorption Line Survey (MALS) project. It starts by giving an overview of the group in section 2.1. It then discusses the observation, calibration and source finding details in sections 2.2 through 2.4. H I emission and absorption is analysed and discussed in sections 2.5 through 2.6 while the discussion and summary is given in section 2.7. The following sections were added to the thesis and were not part of the original publication. Figure 2.1 was added to show the group without H I contours. The Data Reduction and `SoFiA` Source Finding sections 2.3 and 2.4 were also added to give a bit more detail on the data processing steps. In Table. 2.2, columns 14 and 15 have been added, representing the logarithm of the expected H I mass based on stellar mass and H I deficiencies based on stellar mass as described in Bok et al. (2020). The integrated flux density and corresponding uncertainty have been added as Eqns. 2.13 and 2.14. The H I deficiency section 2.5.2, the H I mass size relation Eqn. 2.20, Eqns. 2.25 and 2.26 under subsection 2.7.2.1 titled Argument for ram pressure stripping as well as subsection 2.7.2.2 titled Argument for past tidal interaction have also been added to the thesis.

This work was the result of a collaborative effort among all listed authors below. Each author contributed to various aspects of the published article. The contributions were interdependent, and the final product reflects the collective work of the team.

] E. K. Maina[11], Abhisek Mohapatra,[2] G. I. G. Józsa,[3,1] N. Gupta,[2] F. Combes,[4] P. Deka,[2] J. D. Wagenveld,[3] R. Srianand,[2] S. A. Balashev,[5,6] Hsiao-Wen Chen,[7] J.-K. Krogager,[8] E. Momjian,[9] P. Noterdaeme,[10,11] and P. Petitjean[10]

[1]Department of Physics and Electronics, Rhodes University, P.O. Box 94, Makhanda, 6140, South Africa

[2]Inter-University Centre for Astronomy and Astrophysics, Post Bag 4, Ganeshkhind, Pune 411 007, India

[3]Max-Planck-Institut für Radioastronomie, Auf dem Hügel 69, D-53121 Bonn, Ger-

many
[4] Observatoire de Paris, LERMA, College de France, CNRS, PSL University, Sorbonne University, Paris, France
[5] Ioffe Institute, Politekhnicheskaya 26, 194021 Saint Petersburg, Russia
[6] HSE University, Saint Petersburg, Russia
[7] Department of Astronomy & Astrophysics, The University of Chicago, 5640 South Ellis Avenue, Chicago, IL 60637, USA
[8] Université Lyon1, ENS de Lyon, CNRS, Centre de Recherche Astrophysique de Lyon UMR5574, F-69230 Saint-Genis-Laval, France
[9] National Radio Astronomy Observatory, P.O. Box O, Socorro, NM 87801, USA
[10] Institut d'Astrophysique de Paris, Sorbonne Université and CNRS, 98bis boulevard Arago, F-75014 Paris, France
[11] Franco-Chilean Laboratory for Astronomy, IRL 3386, CNRS and U. de Chile, Casilla 36-D, Santiago, Chile

2.1 Klemola 31 Galaxy Group

Klemola 31 galaxy group is a small group of galaxies located in the Sagittarius constellation in the Southern hemisphere (Klemola, 1969). The group comprises six galaxies with varying masses, gas distribution and morphological types, as summarised in Table 2.1 and seen in Fig. 2.1. These galaxies are within an angular separation of $\sim 5'$ from Klemola 31A, which corresponds to a projected distance of ~176 kpc at the mean redshift of the group, $z_{\rm grp} = 0.029$ (see last column of Table 2.1). There is a background quasar, PKS 2020-370, that is at an angular separation of $18.7''$, i.e., 10 kpc at z_{grp}, from Klemola 31A, and at an angular separation of $45''$ from Klemola 31B. This background quasar is at a redshift of $z = 1.048$.

Each member of the Klemola 31 galaxy group has its redshift, shown in column 4 of Table 2.1, determined either in the publicly available optical spectra from the 6dF Galaxy Survey (6dFGS)[2] or from previous observations. Specifically, ESO 400-11 and LEDA 631562 have their redshifts based on the prominent Hα (λ6565 Å) emission line; while for the early type galaxies, ESO 400-13, Klemola 31B and LEDA 2807038, the Mg (λ5177 Å) and Na (λ5896 Å) absorption lines have been used. However, Klemola 31A ($z_g = 0.0288$), has no public spectra available and therefore has its redshift taken from Boksenberg et al. (1980) and Carilli & Van Gorkom (1987).

H I emission from the group had been detected using the Nançay radio telescope (Boisse et al., 1988). The telescope beam covers four members of the group: Klemola 31A, Klemola 31B, ESO 400-11 and LEDA 2807038. Using the morphology and inclinations of these galaxies, Boisse et al. (1988) argued that the detected H I emission signal (integrated flux, $S = 0.78$ Jy km s^{-1}) corresponds to Klemola 31A ($M_{\rm H\,I} = 6 \times 10^9\,{\rm h}^{-2}\,{\rm M}_\odot$). Later, Carilli & van Gorkom (1992) using the Very Large Array (VLA of the NRAO[3])

[2]http://www.6dfgs.net/
[3]The National Radio Astronomy Observatory is a facility of the National Science Foundation

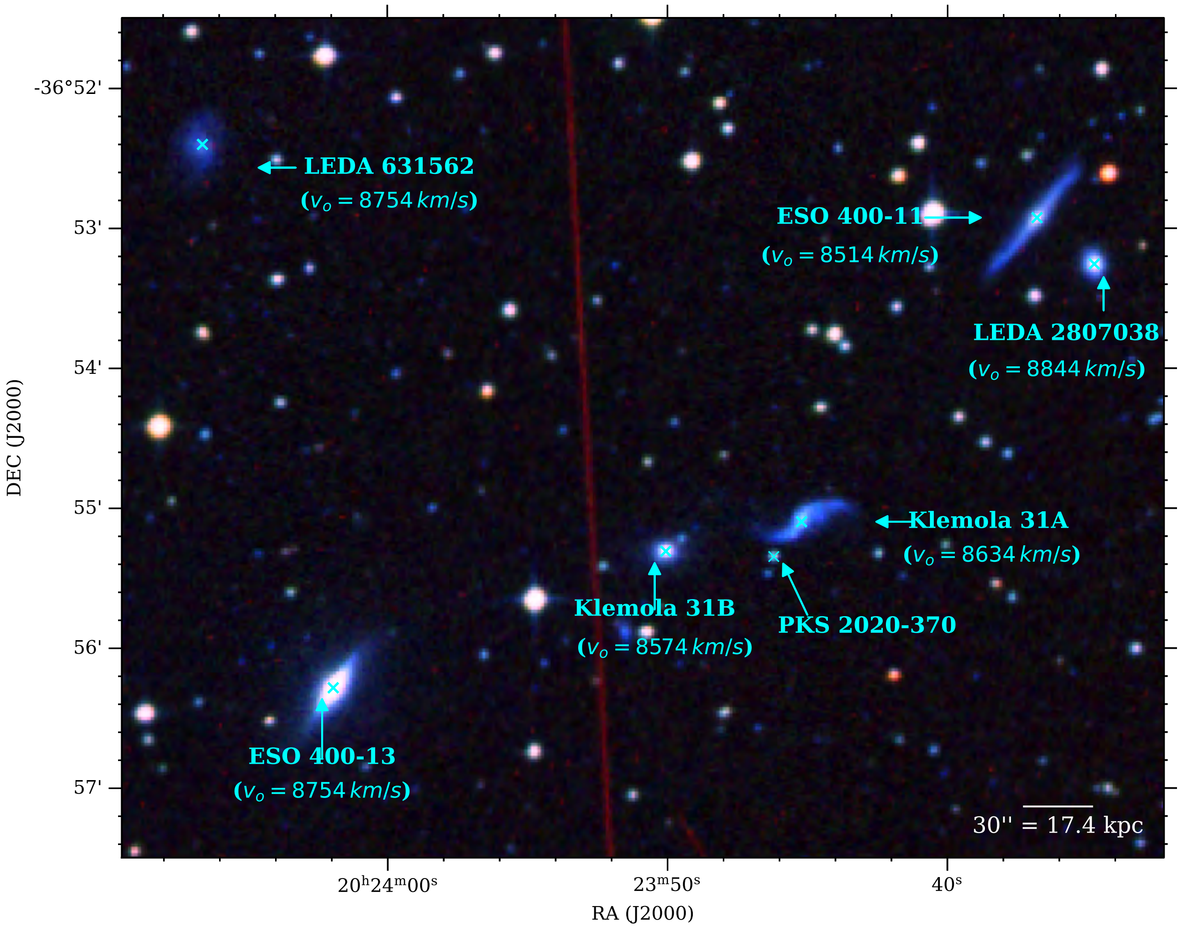

Figure 2.1: SDSS image of Klemola 31 group. The background optical image comes from the Digitized Sky Survey (DSS) B_j, R and I colour composite image. The recession velocities (v_0 in km s^{-1}) corresponding to z_g are written below the name of the galaxy. The cyan crosses correspond to the optical centres of these galaxies.

in BnA and CnB configurations, constrained the H I masses of Klemola 31A and Klemola 31B to be $M_{\rm H\,I}= 1.16 \times 10^9$ h^{-2} $M_\odot$ and $M_{\rm H\,I} < 10^9$ h^{-2} $M_\odot$ respectively. For the H I mass upper limit, they assumed a velocity width of 200 km s^{-1}.

Spectra are also taken in the line-of-sight towards the quasar PKS 2020-370. The spectra show evidence of Ca II H & K absorption lines at $z_{\rm abs}= 0.0287$ (Boksenberg et al., 1980), serving as evidence of gas extending well outside the optical disks/halos of Klemola 31A and Klemola 31B. H I emission line observations by both the Nançay radio telescope and the Very Large Array subsequently showed the gas to be associated with the extended H I disk of Klemola 31A. Junkkarinen & Barlow (1994) detected Na I absorption lines and showed that the ratio N(Ca II)/N(Na I) is rather consistent with the 'halo-like' gas (see also Cherinka & Schulte-Ladbeck, 2011). Both Boisse et al. (1988) and Carilli & van Gorkom (1992) have reported the detections of H I 21-cm absorption from Klemola 31A. However, the best available constraint on integrated H I 21-cm optical depth ($\int \tau {\rm dv} = 0.22 \pm 0.05$ km s^{-1}) is based on VLA A-configuration observations (spectral resolution ∼10 km s^{-1}per channel) that resolve out the extended H I emission signal (Carilli & Van Gorkom, 1987). This corresponds to a H I column density, $N_{\rm H\,I} = 4.0 \times 10^{19} (T_s/100\,{\rm K})$ cm^{-2}.

The availability of a variety of H I 21-cm emission and absorption line information motivated the use of the Klemola group as a target for MALS science verification observations. At the same time, the H I 21-cm emission line properties of the other four members of the galaxy group, i.e., ESO 400-11, LEDA 2807038, LEDA 631562 and ESO 400-13, have not been discussed at all in the literature, and the absorption signal towards PKS 2020-370 although unambiguously detected, albeit as a single pixel, is not well characterized due to the low spectral resolution. Thus, it is also an intriguing target to follow-up using the large field-of-view, excellent sensitivity and high spectral resolution of MeerKAT observations presented here.

2.2 Observation Details

2.2.1 uGMRT

The Klemola 31 group had been observed using upgraded Giant Metrewave Radio Telescope (uGMRT) from the 28th to the 29th of May 2018 with a total on-source time of 6.3 hours with a bandwidth of 4.17 MHz split into 512 channels. The flux density scale and bandpass calibrator source observed was 3C 48, while the compact radio source PKS1954-388 was also observed for 7 minutes every ∼ 50 minutes. This observation was planned to complement the MeerKAT observations of PKS2020-370 carried out from November 7 to 9, 2017, using only 16 antennas from the MeerKAT array with the sole purpose of detecting the absorption for verification purposes.

operated under cooperative agreement by Associated Universities, Inc.

Table 2.1: List of galaxy members of Klemola 31 group.

Name	RA	DEC	z_g^+	B mag†	$D_{25}^\dagger$	$i_{opt}^\dagger$	Morph.†	Angular separation	Impact parameter	Stellar Mass
				(mag)	(kpc)			(arcmin)	(kpc)	(log M_*)
(1)	(2)	(3)	(4)	(5)	(6)	(7)	(8)	(9)	(10)	(11)
ESO 400-11	20:23:36.81	-36:52:55.48	0.0284	15.79	42.7 ± 4.0	79°	Sc	2.75	96	10.48
ESO 400-13	20:24:01.94	-36:56:16.99	0.0292	14.98	41.6 ± 4.2	64°	S0	3.55	124	11.09
Klemola 31A	20:23:45.21	-36:55:05.87	0.0288	15.91	31.5 ± 3.9	68°	Sc	-	-	9.68
LEDA 631562	20:24:06.06	-36:52:24.00	0.0292	16.52	21.5 ± 4.3	46°	Sbc*	5.06	176	9.17
Klemola 31B	20:23:50.06	-36:55:18.54	0.0286	16.80	19.2 ± 6.7	55°	E*	0.99	35	10.46
LEDA 2807038	20:23:34.76	-36:53:15.31	0.0295	16.80	15.2 ± 6.3	39°	E*	2.79	97	10.21

Columns 1 − 3: Galaxy name, position i.e., right ascension and declination (J2000) from SIMBAD[a]. Column 4: redshift of the galaxy obtained from the optical spectra of 6dF Galaxy Survey (6dFGS); for Klemola31A see Boksenberg et al. (1980) and (Carilli & van Gorkom, 1987). Column 5: Total B-band magnitude. Column 6: the extinction-corrected optical diameter measured at the 25th mag arcsec^{-2} isophote from HyperLeda. Column 7: inclination angle calculated from the axis ratio of the isophote at 25 mag arcsec^{-2} in the B-band. Column 8: Morphological type of the galaxy. Column 9: Angular separation from Klemola 31A. Column 10: Projected distance from Klemola 31A using average redshift of the group, $z_{grp} = 0.0290$. Column 11: Stellar masses calculated using WISE W1 (3.35μm) and W2 (4.6μm) magnitudes as described in Cluver et al. (2014)

†from HYPERLEDA; * from visual classification based on the optical image.

[a] http://simbad.u-strasbg.fr/simbad/

Following these observations, the uGMRT data was processed using `ARTIP` (Gupta et al., 2021), resulting in a STOKES-I image made using ROBUST=0 weighting of the visibilities and a restoring beam of $3.9'' \times 1.8''$ with a position angle of 29.4°. At this resolution, PKS2020-370 remained unresolved and therefore compact with a deconvolved size of $0.7'' \times 0.1''$, a position angle of $45 \pm 2°$ and a peak and total flux density of 407 ± 0.4 mJy beam^{-1} and 419.3 ± 0.8 mJy respectively. From this STOKES-I cube, an absorption spectrum at the position of PKS2020-370 was extracted. This absorption spectrum had a spectral resolution and rms[4] noise of 1.88 km s^{-1} and 1.7 mJy beam^{-1} channel^{-1} respectively. This spectrum was used in the subsequent sections.

2.2.2 MeerKAT

A follow-up observation of the Klemola 31 A galaxy group was made from April 1 2020, using 60 Antennas of MeerKAT-64 array and 32K mode of the SKA Reconfigurable Application Board (SKARAB) correlator. This observation was part of the science verification observing run with a total duration of 184 minutes. However, the array's pointing centred on PKS2020-370 had a total on-source time of 56 minutes. This total time of 56 minutes was split into three scans of different hour angles so as to improve the UV coverage. 3C286 and PKS 1939-638 were observed and used as the delay, flux density scale and bandpass calibrators, while the compact radio source J2052-3640 was regularly observed for complex gain calibration.

This resulted in an observation with a total bandwidth of 856 MHz centred on 1283.9869 MHz that was split into 32,768 channels. In the region close to the H I 21-cm line frequency at the redshift of $z = 0.029$, the channel width corresponded to a velocity resolution of 5.7 km s^{-1}. Data from all four polarisations, labelled XX, YY, XY and YX, was obtained with a correlator dump time of 8 seconds. Since we were only interested in the Stokes-I properties of the target, only XX and YY polarisation products were processed through the Automated Radio Telescope Imaging Pipeline (`ARTIP`) (Gupta et al., 2021).

2.3 Data Reduction

The Automated Radio Telescope Imaging Pipeline (`ARTIP`) (Gupta et al., 2021) is a radio interferometric data calibration pipeline developed for the MeerKAT Absorption Line Survey (MALS). It is written in Python and extensively uses the Common Astronomy Software Application (`CASA`) tasks and tools. The main objective of the pipeline is to produce full Stokes spectral line cubes as well as radio continuum images with as little manual intervention as possible. In spite of having been designed for the MALS dataset, `ARTIP` is general enough to be able to process data from other radio interferometers such as the Karl G. Jansky Very Large Array (VLA) as well as the uGMRT. This generalized ability to process data from different radio interferometers

[4] The rms of an image is defined as the average fluctuations or noise in an image.

informed and allowed for the testing and optimisation of algorithmic choices that are used in MALS data processing. Consequently, `ARTIP` follows a modular design, allowing flexibility and the ability to extend various processing steps. Specifically, each stage can be configured through a `JavaScript Object Notation` (`JSON`) or the `YAML Ain't Markup Language file` Ben-Kiki et al. (`YAML`; 2009) and can also be entirely replaced by external software.

`ARTIP` can be used as a single node application on a workstation or as a part of a cluster, where it can fully utilize its capabilities through the Pipeline Manager. The Pipeline Manager Service can be launched either through the command line, where it operates in a standalone environment, or using the uWSGI server in a production-like environment. It is designed to be intuitive and to allow for collaborative `ARTIP` execution, monitoring and management of the end products of the pipeline. Consequently, the Pipeline Manager allows a MALS user to:

1. Set up the different CAL, CUBE, CONT and Diagnostic stages.

2. Trigger `ARTIP` and monitor its progress using the traffic light status where Blue represents finished, Yellow is in progress, Grey means not started, and Red means failed. A user can also monitor the processing using the logs generated.

3. Reset `ARTIP` to a particular stage and restart the processing should need to be.

4. Push the right diagnostic plots to the database for quality control and potentially to the medium-term storage in MALS for archiving.

`ARTIP` follows a stage-driven architecture where outputs from one stage serve as inputs for the subsequent stages. Specifically, at the highest level, `ARTIP` is split into the following four sections:

1. ARTIP-CAL: The purpose of ARTIP-CAL is to calibrate the input raw visibilities and output the target source visibilities. This section can also handle multiple target sources and calibrators.

2. ARTIP-CUBE: Takes the output of ARTIP-CAL and does spectral-line imaging on it. This includes any necessary RFI-flagging, self-calibration, continuum subtraction, as well as spectral line imaging or cube imaging. This results in spectral-line cubes that can be used to generate H I moment maps and absorption-line catalogues.

3. ARTIP-CONT: Takes the output of ARTIP-CAL and does wide-band radio continuum imaging with the option to flag and self-calibrate as needed.

4. ARTIP-Diagnostic: Acts on the outputs of ARTIP-CAL, ARTIP-CONT and ARTIP-CUBE with the purpose of generating diagnostic plots and statistics. The pipeline status and logs can be used to monitor and debug the processing if need be while the diagnostic plots and statistics can be used to assess the quality of flagging, calibration and data products.

The following sub-section expounds on the various sections mentioned above.

2.3.1 ARTIP-CAL

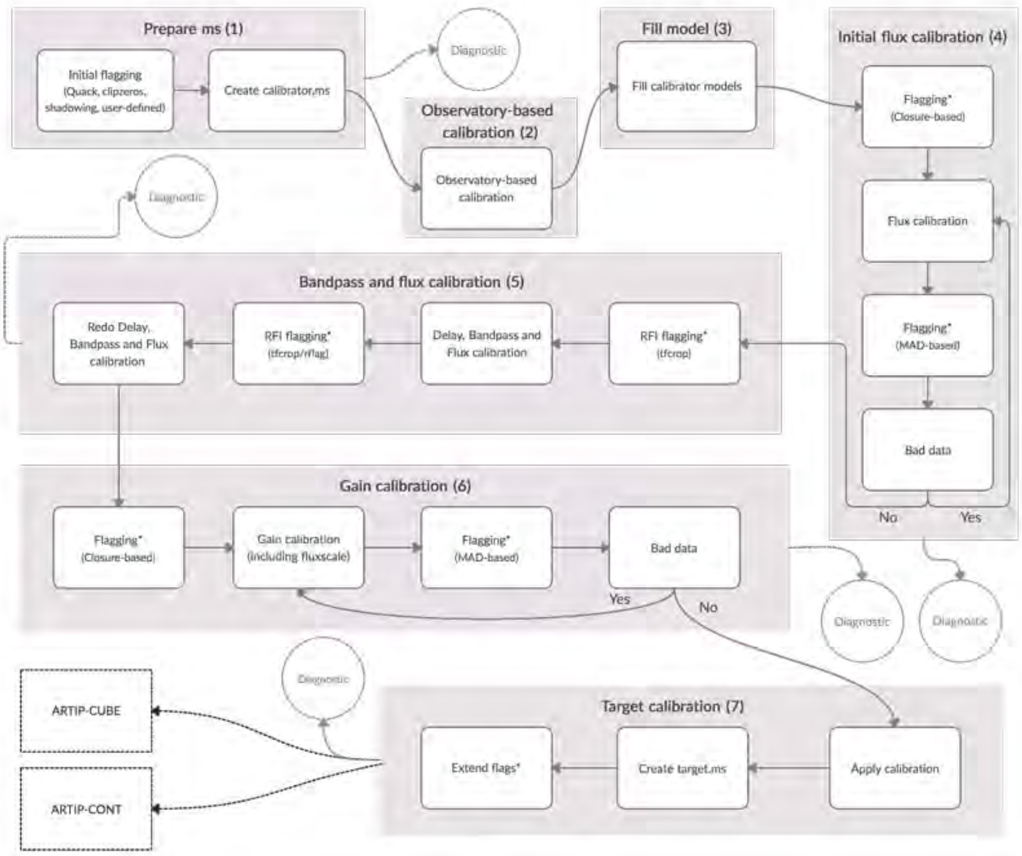

Figure 2.2: Seven stages of ARTIP-CAL processing. The * indicates that the step is optional while the Diagnostic, represented by dashed lines, may be triggered at the end of each stage or after all the stages at the very end of the processing (Gupta et al., 2021).

ARTIP-CAL has seven stages implemented as Python classes (please see Fig. 2.2). These stages can be toggled on or off as required and are further split into substages, which are either subclasses or functions.

The initial observatory-based flagging was applied to the data in stage 1, prepare ms, resulting in a measurement set containing only the calibrator data, the *calibrator.ms*. The flagging consisted of the following steps:

I. RFI masking to eliminate persistent interference.

II. Clipping scans and the edges of spectral windows.

III. Flagging data that corresponded to faulty antennas, zeros and NANs, as well as shadowing.

Following the observatory-based flagging, the observatory-based calibration results in calibration tables that correct for the atmospheric optical depth, ionospheric effects and variation in the gains of antennas and electronics. This calibration is stage 2 on the *calibrator.ms* data that subsequently fed into stage 3, where the model visibilities for the primary flux calibrators were filled in *calibrator.ms*.

Thereafter, the flux density calibrator was used to identify bad data for all spectral windows, e.g. bad baselines and time ranges and non-working antennas. This happened in stage 4, where RFI-free channels of the raw visibilities were analysed for phase dispersion and closures, and the time ranges, antennas or baselines beyond a given threshold were flagged. Following this flagging was the flux calibration process, which was followed by examining the flux calibrator data using the median and median absolute deviation (MAD) statistics to identify bad time ranges. This process was repeated until no bad data beyond a given threshold was found.

Once it was ascertained that there was no more bad data left, the processing proceeded to stage 5, where it went through the delay, bandpass and flux-density calibration with RFI flagging.

Following this was stage 6, where the secondary calibrator gains were determined and finally, stage 7, where all the calibration solutions determined were applied to target sources, which were then split into separate target sources, i.e. one MeasurementSet (ms) per pointing.

2.3.2 ARTIP-CUBE

The measurement set file containing our target source proceeded to the next stage, ARTIP-CUBE, where it was partitioned into 15 spectral windows (SPW-0 to SPW-14) with an overlap of 256 frequency channels in stage 1 of Fig. 2.3. SPW-9 covered the relevant frequency spectrum of 1351 - 1411 MHz for this study and was consequently selected for RFI flagging in stage 2. In stage 3, the data set was averaged in frequency to generate continuum datasets that were later imaged and later self-calibrated. These self-calibrated solutions from Stage 3 were applied to the RFI-flagged line datasets from Stage 2 in Stage 4. This was followed by continuum subtraction, where model visibilities determined from the continuum source model were subtracted from the dataset, followed by fitting a polynomial, i.e., the UVLIN or UVCONTSUB approach.

2.3.3 Imaging

Both the self-calibrated continuum image from stage 3 of ARTIP-CUBE and the continuum subtracted data cube from stage 4 of ARTIP-CUBE were imaged. The continuum image was obtained using ROBUST=0 weighting of the visibilities in the CASA TCLEAN task and had a resolution of $11.6'' \times 7.0''$ with a position angle of -85.8° and an rms noise measured close to the quasar of $\sim 80\mu$Jy beam^{-1} at the reference frequency of 1380.8 MHz. This quasar was unresolved and had a total column flux density of 404.1 ± 1.1 mJy, with this flux density and uncertainty determined by fitting a single

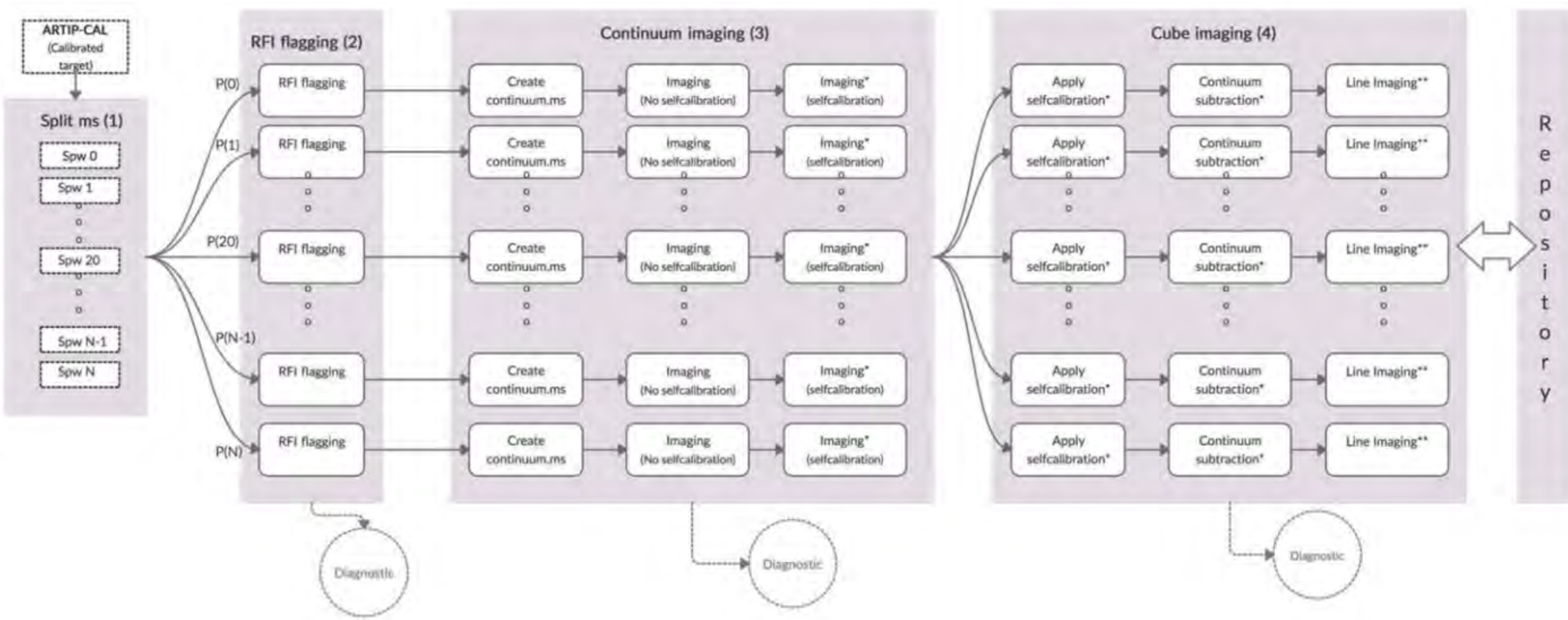

Figure 2.3: Four stages of ARTIP-CUBE processing. The * indicates that the step is optional, while the diagnostic, represented by dashed lines, may be triggered at the end of each stage or after all the stages at the very end of the processing. ** indicates that the substage may be run any number of times as needed while P(1), P(2), ..., P_n represent processes split across n worker nodes (Gupta et al., 2021).

Gaussian component to the continuum image.

When it came to the continuum-subtracted data cube, only the central 34′ portion centred on PKS 2020-370 was imaged, as this was adequate to cover the galaxy group Klemola 31. The imaging was done by setting the ROBUST parameter to zero, resulting in a data cube with 1024 × 1024 spatial pixels of size 2″ each and 2304 frequency channels, each channel having a resolution of 5.7 $\mathrm{km\,s^{-1}}$. This imaged FITS cube had a common restoring beam of 11.9″ × 7.6″ (6.9 kpc ×4.4 kpc at the group redshift) with a position angle of −82.7° and an rms of 0.79 $\mathrm{mJy\,beam^{-1}\,channel^{-1}}$. This data cube was further deconvolved using the Common Software Applications (`CASA`) package task TCLEAN down to five times the single channel rms value. This deconvolved data cube was later analysed with `SoFiA 2` (Westmeier et al., 2021).

`SoFiA` is a software application used to detect and parametrise sources in 3D spectral line datasets commonly referred to as the Flexible Image Transport System (FITS) files (Pence et al., 2010). `SoFiA 2` is a reimplementation of the original `SoFiA` pipeline in C programming language, making use of OpenMP for parallel processing and is consequently faster and more memory efficient (Westmeier et al., 2021). Therefore, we shift our focus to using `SoFiA 2`.

2.4 SoFiA Source Finding

2.4.1 Input Data Cube

Following the steps in the algorithm shown in Fig. 2.4, `SoFiA 2` was given the FITS cube.

2.4.2 Flagging

From the FITS cube, `SoFiA 2` measured the noise levels, $\sigma_{rms}(i)$, in each spatial and spectral channel. It then calculated the median (μ) of the rms values and the Median Absolute Deviation (MAD $\overline{\mu}$) from these median values. Taking in a user-specified threshold *flag.threshold=5.0* from the parameter file, it flagged all channels or pixels satisfying Eqn. 2.1

$$|\sigma_{rms}(i) - \mu| = C \times \upsilon \times \overline{\mu} \qquad , \tag{2.1}$$

where υ is the user-supplied threshold mentioned above, and constant C ∼ 1.4826 was used to convert MAD to normal standard deviation.

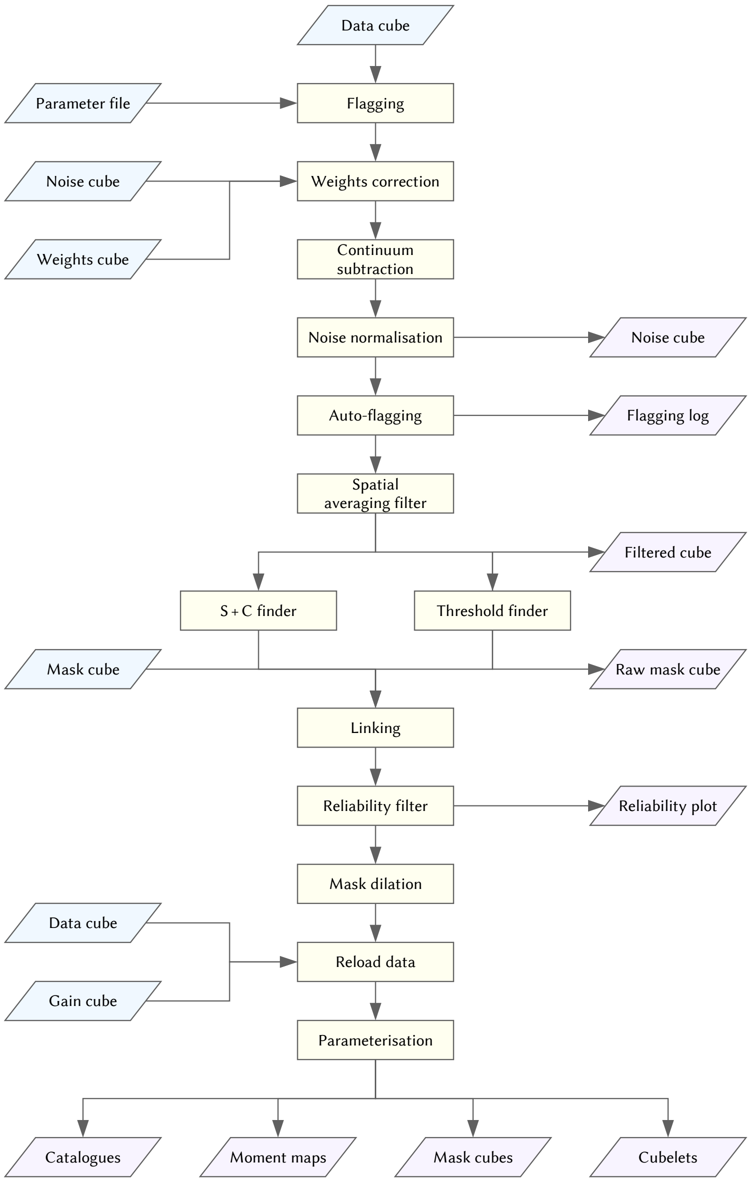

Figure 2.4: `SoFiA 2` algorithm shown in the form of a flow chart with inputs represented as blue, steps as yellow and outputs as purple (Tobias Westmeier, 2021).

.

2.4.3 Continuum Subtraction

Once the cube was flagged, `SoFiA 2` extracted a spectrum at each spatial position in the datacube. This spectrum was shifted in two directions, that is, in one direction by +*contsub.shift=4.0* and the opposite direction by -*contsub.shift=4.0* where the *contsub.shift=4.0* parameter was supplied by the user in the input parameter file. These two shifted spectra were subtracted from each other, the noise levels measured from the subtracted spectrum and all channels with the absolute value exceeding the user-supplied value of *contsub.threshold=2.0* were flagged. As a safety margin, an additional padding of ±*contsub.padding=3.0* was applied around the flagged channels. This was followed by fitting a polynomial of *contsub.order=1.0* to the remaining channels of the original spectrum. This polynomial was subtracted from the original cube in the process of continuum subtraction. This was done to ensure that any residual continuum sources were adequately dealt with before noise normalisation and, thereafter, source finding.

2.4.4 Noise Normalisation

In order to deal with any and all noise variations across the FITS cube both spatially and spectrally, the noise normalisation algorithm for `SoFiA 2` was switched on by setting *scaleNoise.mode=local*. This was followed by supplying the user-specified parameter values *scaleNoise.windowXY=71* and *scaleNoise.windowZ=71*. Thereafter, `SoFiA 2` made a shifting window across all three dimensions of the data cube on a grid that was half the window size since the grid size was not specified. `SoFiA 2` measured the rms value in each window and divided the corresponding grid cell by that rms value. To make sure that there were no sharp boundaries between the grid cells, linear interpolation between the grid cells was enabled by setting *scaleNoise.interpolate=True*.

2.4.5 S+C finder

Following noise normalisation was the source finding where `SoFiA 2` followed the following steps.

1. `SoFiA 2` created a copy of the noise-normalised data cube.
2. All pixels already detected in the previous iteration had their values replaced by *scifind.replacement=2.0* × *rms*.
3. All blanked pixels had their values set to 0 before smoothing.
4. The FITS cube was later convolved by a combination of N spatial filters × M spectral filters. The FWHM of the spatial Gaussian kernels were specified by *scifind.kernelXY=(0, 3, 6, 9)* and were assumed to be symmetric in the two spatial directions, whereas the widths of the spectral boxcar filters were specified using *scifind.kernelZ=(0, 3, 7, 15)*.
5. After convolution, all pixels with value 0 were changed back to NANs.

6. The rms noise levels were measured in the convolved FITS cube.

7. All pixels with values greater than *scifind.threshold=3.5* × rms had their positions marked in the source mask.

8. The smoothed fits cube was deleted, and this process was repeated until the full combination of N × M kernels was used to smooth the cube and find detections.

Once the complete number of detections had been made in the source mask, the next process involved grouping these detections into sources and discarding false detections based on parameters, as explained in subsections 2.4.6 and 2.4.7 below.

2.4.6 Linking

In the grouping process, the linking algorithm looped over the mask cube and detected the first pixel marked as a detection but has not been associated with a source. This pixel was assigned a new source ID and then the algorithm recursively searched all neighbouring pixels within a certain merging volume, defined in Eqn. 2.2, for additional pixels. All additional pixels found within this merging volume were then assigned the same source ID. Once all pixels within the merging volume were found and assigned the same ID and correctly labelled, the algorithm moved on to find the next source in a friend-of-friends algorithm manner. The merging volume is given by:

$$\frac{(x-x_0)^2}{r_{xy}^2} + \frac{(y-y_0)^2}{r_{xy}^2} + \frac{(z-z_0)^2}{r_z^2} \leq 1 \qquad , \tag{2.2}$$

where (x_0, y_0, z_0) are the central pixel coordinates of the merging volume and the values (x, y, z) were supplied as *linker.radiusXY=1* and *linker.radiusZ=2* in `SoFiA 2` parameter file. All linked sources found to be smaller than *linker.minSizeXY=8* and *linker.minSizeZ=5* were assumed to be false detections and were consequently removed and not included in the parametrisation section.

2.4.7 Reliability filter

Of the remaining detections, the procedure that followed involved determining their reliability. Since a very low source finding threshold of 3.5 was used, the reliability filter enabled filtering out a large number of detections which could not be verified. This involved comparing the density of positive and negative detections in parameter space $s_{sum}, s_{max}, s_{min}$ where $s_{sum} = S_{sum}/\sigma_{rms}$ is the summed rms, $s_{max} = S_{max}/\sigma_{rms}$ is the peak flux density and $s_{mean} = s_{sum}/n_{pix}$ is the mean flux density across the source. The distribution of positive (blue) and negative (sources) in parameter space is shown in Fig. 2.5 for our case, where the black dots occupying a different region in parameter space compared to false detections are black in colour and represent our genuine detections.

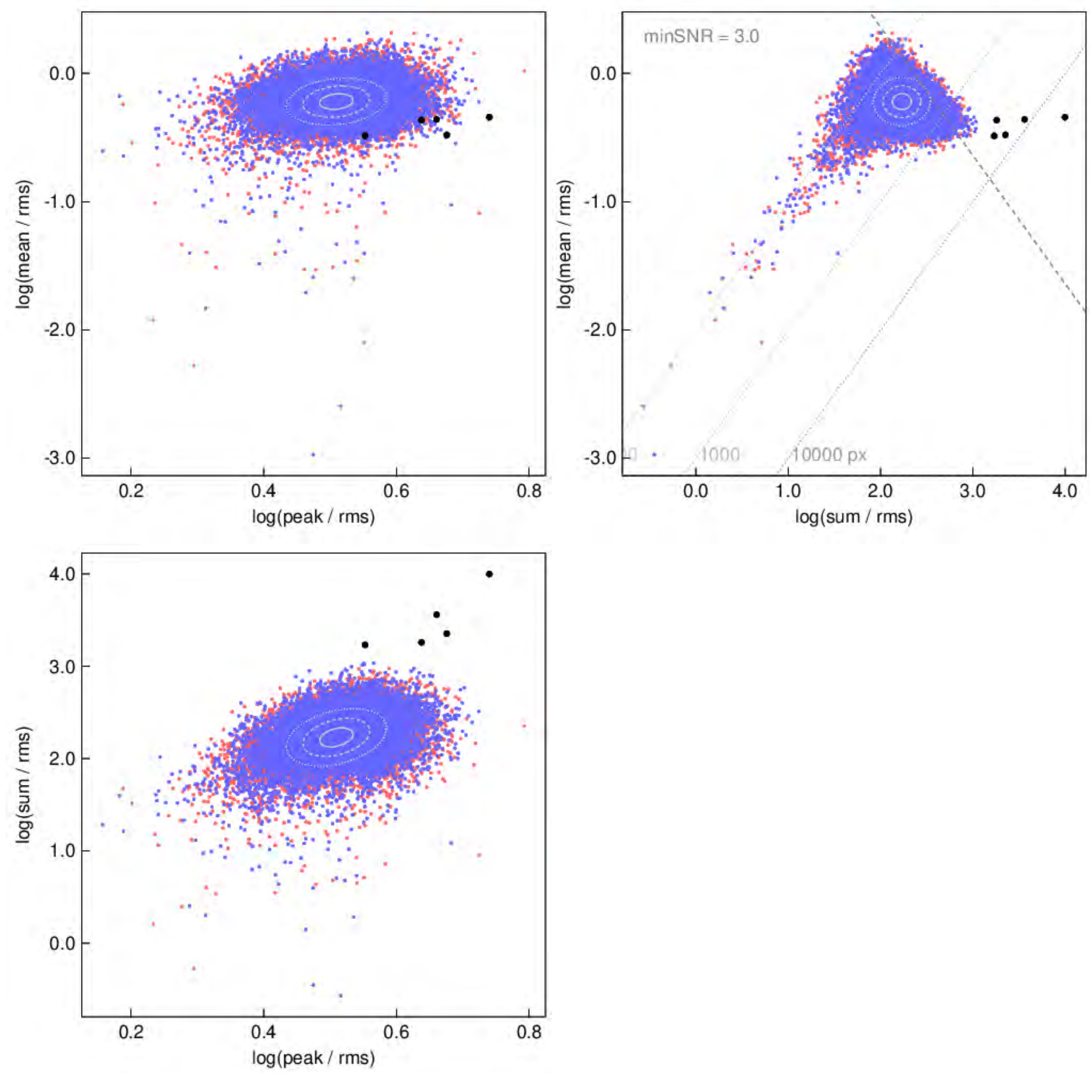

Figure 2.5: Three projections of the three-dimensional parameter space in which SoFiA calculates the reliability of detections. Each projection represents the distribution of positive (blue) and negative (red) sources in parameter space with the black dots representing our genuine sources. The grey dashed line represents the integrated constant signal-to-noise ratio limit of 3.0 below which sources are deemed unreliable and consequently are discarded and light grey ellipses are $1\sigma, 2\sigma$ and 3σ contours of the 3D Gaussian function used in the kernel density estimator (KDE).

The density of positive and negative sources was measured by performing a Gaussian kernel density estimation (KDE) on the individual sources in parameter space in Fig. 2.5. The relative size of the Gaussian kernel used in the KDE was set as *reliability.scaleKernel=0.38*. Upon setting the kernel size, the densities of positive and negative sources were later fed into Eqn. 2.3 to determine positive detections reliability R.

$$R = \begin{cases} \frac{n_{pos}-n_{neg}}{n_{pos}}, & \text{for } n_{pos} \geq n_{neg}, \\ 0, & \text{otherwise} \end{cases} \tag{2.3}$$

where n_{pos} and n_{neg} represent positive and negative detections and are marked blue and red in colour, respectively. This resulted in the black genuine sources in Fig. 2.5, our positive sources, to be found with a reliability threshold of above 95%.

The integrated signal-to-noise ratio was also used to filter out a majority of unreliable detections, as shown by the grey dashed line in Fig. 2.5. This $\mathrm{SNR_{min}}$ was set to *reliability.minSNR=3.0* and calculated using:

$$\frac{S_{sum}}{\sigma_{rms}\sqrt{N_{pix}\Omega_{PSF}}} < \mathrm{SNR_{min}} \quad , \tag{2.4}$$

where S_{sum} is the sum of all flux densities across the detection, σ_{rms} the global rms level of the data cube and Ω_{PSF} the restoring beam solid angle in pixels. All sources falling below this SNR threshold were filtered out.

2.4.8 Parametrisation

Once reliable sources were determined, `SoFiA 2` proceeded to measure a range of source parameters across the source mask. The total flux, S_{sum}, was found by summing the flux density values, typically in units of Jy/beam, across all spatial and spectral pixels representing a given source.

$$S_{sum} = \Sigma_i S_i \quad , \tag{2.5}$$

Since the parameter *parameter.physical* was enabled, `SoFiA 2` multiplied S_{sum} by the spectral channel width, Δz, and divided by the solid angle, Ω_{PSF}, of the beam:

$$S_{sum} = \frac{\Delta z}{\Omega_{\mathrm{PSF}}}\Sigma_i S_i \quad , \tag{2.6}$$

where the solid angle, Ω_{PSF}, of the beam was calculated as

$$\Omega_{\mathrm{PSF}} = \frac{\pi\theta_a\theta_b}{4\ln 2} \quad , \tag{2.7}$$

and θ_a, θ_b are the Full Width at Half Maximum (FWHM) of the major and minor axis of the Gaussian restoring beam in pixel units. The statistical uncertainty of the integrated flux was derived by applying the error propagation law to Eqn. 2.5, hence

$$\sigma^2_{S_{sum}} = \Sigma_i \sigma^2_{S_i} = N_{\mathrm{pix}\sigma^2_{rms}} \quad , \tag{2.8}$$

where N_{pix} is the total number of pixels across the detected source (Westmeier et al., 2021). On applying the error propagation law to Eqn. 2.6, we obtain

$$\sigma_{S_{sum}} = \sqrt{\frac{N_{\mathrm{pix}}}{\Omega_{\mathrm{PSF}}}} \Delta z \sigma_{\mathrm{rms}} \quad . \tag{2.9}$$

These parameters were produced in a catalogue format alongside moment maps and mask cubes, and used to derive values in Table. 2.2.

The output 3-dimensional `SoFiA 2` mask was further used to deconvolve the data cube down to a single channel rms. This cube was later corrected for primary beam attenuation using the model from KAT-BEAM library[5] where the data cube was divided by the Katbeam primary beam pattern using `CASA` command IMPBCORR. The resultant cube was used for generating H I moment maps using `SoFiA`, as discussed above.

2.5 H I emission

After calibration, imaging and source finding, H I emission was detected in four out of the six members of the Klemola 31 group. All the galaxies observed in H I were spatially resolved above 3 beam elements along the projected major axis, as well as spectrally resolved at ~ 5.7 km s^{-1} . The detected emission resides in the frequency range 1379.4 - 1382.2 MHz, corresponding to the redshift range of $z_{\mathrm{H\,I}} \sim 0.0276 - 0.0297$ or a recession velocity range of $v_0 = cz_{\mathrm{H\,I}} \sim 8274.3 - 8903.8$ km s^{-1} ; estimated from the centres of the global H I emission profiles of individual galaxies. Fig. 2.6 shows these four galaxies, which were detected in H I as well as the remaining two galaxies undetected in H I . The figure was made using the DSS B_j, R and I colour composite image as the background with names obtained from SIMBAD[6] and contours representing H I column densities of $2^{\mathrm{n}} \times 5 \times 10^{10}$ cm^2.

The total H I intensity map $\int I(v)dv$ Jy km s^{-1} beam^{-1} from `SoFiA` was converted to the column density map ($N_{\mathrm{H\,I}}$) using:

$$\frac{N_{\mathrm{H\,I}}}{\mathrm{cm}^{-2}} = \frac{1.104 \times 10^{24}(1+z)^3}{b_{maj} \times b_{min}} \int \frac{I(v)}{\mathrm{Jy\,beam}^{-1}} \frac{dv}{\mathrm{km\,s}^{-1}}. \tag{2.10}$$

where b_{maj} and b_{min} represent the major and minor axes of the restoring beam, $\int I(v)dv$ the total H I intensity in Jy km s^{-1} beam^{-1} , v, the line of sight velocity in the reference frame of the target, and z the redshift of the target. Taking a channel width of 15 km s^{-1} , the 3σ calculated rms was found to be 3.1×10^{20} cm^{-2} (please see section 1.5.2 for futher details).

[5] https://github.com/ska-sa/katbeam
[6] This research has made use of the SIMBAD database, operated at CDS, Strasbourg, France

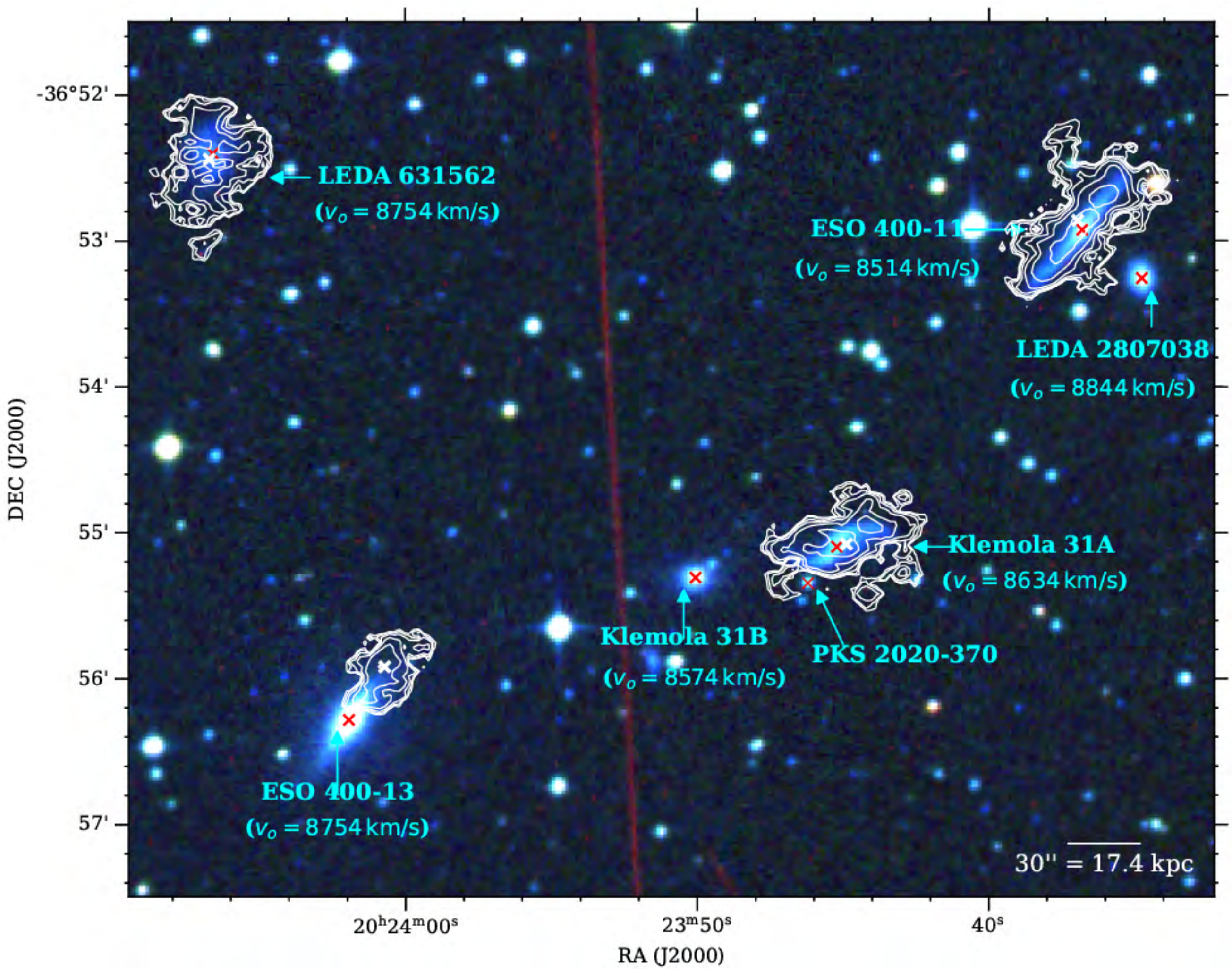

Figure 2.6: Klemola 31 group in H I. The H I column density contours are derived from the moment-0 map and correspond to H I column densities of $2^n \times 5 \times 10^{19}\text{cm}^2$ ($n = 0, 1, 2, 3, ...$). The background optical image comes from the Digitized Sky Survey (DSS) B_j, R and I colour composite image. The radio image has a restoring beam of ($11.9'' \times 7.6''$) with a position angle of $-82.7°$. The recession velocities (v_0 in km s^{-1}) corresponding to z_g are written below the name of the galaxy. The red and white crosses correspond to the H I and optical centres of these galaxies.

Table 2.2: Properties of Klemola group members based on H I 21-cm emission line

		ESO 400-11	ESO 400-13	Klemola 31A	LEDA 631562	Klemola 31B	LEDA 2807038
(1)	R.A.	$20^h 23^m 36\overset{s}{.}96$	$20^h 24^m 0\overset{s}{.}72$	$20^h 23^m 44\overset{s}{.}88$	$20^h 24^m 6\overset{s}{.}72$	$20^h 23^m 50\overset{s}{.}16$	$20^h 23^m 34\overset{s}{.}8$
(2)	Declination	$-36° 52' 51''.6$	$-36° 55' 55''.2$	$-36° 55' 4''.8$	$-36° 52' 26''.4$	$-36° 55' 19''.2$	$-36° 53' 16''.8$
(3)	$z_{\rm H\,I}$	0.02867	0.02861	0.02872	0.02927	-	-
(4)	$v_{\rm H\,I}$ (km s^{-1})	8595	8577	8610	8776	-	-
(5)	S (Jy km s^{-1})	2.03 ± 0.13	0.32 ± 0.06	0.86 ± 0.08	0.40 ± 0.07	< 0.14	< 0.14
(6)	log $M_{\rm H\,I}$ ($M_\odot$)	9.86 ± 0.03	9.05 ± 0.09	9.50 ± 0.04	9.20 ± 0.08	< 8.7	< 8.7
(7)	MAJ_s (arcsec)	38.7	19.2	32.7	24.6	-	-
(8)	MIN_s (arcsec)	15.5	11.8	15.1	18.7	-	-
(9)	PA_s (°)	−47.1	−42.3	−65.9	−8.1	-	-
(10)	$D_{\rm H\,I}$ (kpc)	44.7	23.4	38.0	28.8	-	-
(11)	$D_{\rm H\,I}/D_{25}$	1.04	0.56	1.21	1.34	-	-
(12)	log $M_{\rm H\,I}^{\rm exp}$ ($M_\odot$)	9.98 ± 0.21	9.89 ± 0.21	9.72 ± 0.21	9.28 ± 0.21	9.17 ± 0.21	9.20 ± 0.21
(13)	DEF ($M_\odot$)	0.12	0.84	0.22	0.08	-	-
(14)	log $M_{\rm H\,I}^{\rm exp}$ ($M_\odot$)	9.80 ± 0.33	10.07 ± 0.33	9.45 ± 0.33	9.22 ± 0.33	-	-
(15)	DEF ($M_\odot$- M_*)	−0.06	1.02	−0.05	0.02	-	-

Columns 1-4: Right ascension, declination, redshift and systemic velocity for every member of the galaxy group detected in H I. Column 5: Integrated flux. Column 6: H I mass. Columns 7-9: H I discs major axes, minor axes and position angles from `SoFiA 2` in arcseconds. Column 10: H I disc diameters in kpc from an ellipse fitted to the H I column density contour maps corresponding to 1 $M_\odot$ pc^{-2} = 1.25×10^{20} cm^{-2}. Column 11: Ratios of the H I to optical disk diameters. Column 12: Logarithm of the expected H I mass. Column 13: H I deficiencies. Column 14: Logarithm of the expected H I mass based on stellar mass as described in Bok et al. (2020). Column 15: H I deficiencies based on stellar mass as described in Bok et al. (2020).

The Baldwin, Philips, & Terlevich (BPT) diagnostic was also determined for Klemola 31 group; from RCSED2[7]. The N [II]/Hα versus [O III]/Hβ ratios for LEDA 631562 are consistent with ionization through a power-law spectrum, i.e., an active galactic nucleus (Chilingarian et al., 2017); while the BPT diagnostic for ESO400-11 and ESO400-13 is consistent with these two galaxies being normal star-forming galaxies.

In addition to this, ESO400-11 is the only galaxy that is clearly detected in the MALS wideband image (rms noise $\sim 30\ \mu$ Jy beam^{-1}) with a total flux of $L_{1.4\mathrm{GHz}} = 3.1$ mJy. From this flux and the co-moving distance of 114 Mpc, a star formation rate (SFR) of 2.8 M$_\odot$ yr^{-1} was calculated using Eqn. 2.11 from Bell (2003):

$$\psi(\mathrm{M_\odot yr^{-1}}) = \begin{cases} 1.57\times 10^{-22} L_{1.4\mathrm{GHz}} & L > L_c \\ \frac{5.52\times 10^{-22}}{0.1+0.9(L/L_c)^{0.3}} L_{1.4\mathrm{GHz}} & L \leq L_c \end{cases} , \quad (2.11)$$

where $L_c = 6.4\times 10^{21}$W Hz^{-1} is the radio luminosity at 1.4 GHz of a galaxy whose total infra-red luminosity at $8 - 1000\mu$m $\sim 2\times 10^{10}$ L$_\odot$.

2.5.1 H I mass and morphology

The total H I intensity map $\int I(v)dv$ Jy km s^{-1} beam^{-1} from `SoFiA` was used to determine the H I masses ($M_{\mathrm{H\,I}}$) for Klemola 31 group, as shown in Table 2.2, by following Eqn. 2.12

$$\frac{M_{\mathrm{H\,I}}}{\mathrm{M_\odot}} = \frac{2.356\times 10^5}{1+z_{\mathrm{H\,I}}} \times \left(\frac{D_L}{\mathrm{Mpc}}\right)^2 \int \frac{S(v)}{\mathrm{Jy}} \frac{dv}{\mathrm{km\,s^{-1}}} , \quad (2.12)$$

where D_L is the cosmological luminosity distance and $S(v)$ Jy km s^{-1} determined by dividing the total H I intensity map ($\int I(v)dv$ Jy km s^{-1} beam^{-1}) by the beam solid angle Ω_{PSF}:

$$\frac{S(v)}{\mathrm{Jy\ km\,s^{-1}}} = \frac{\frac{\int I(v)dv}{\mathrm{Jy\ km\,s^{-1}\ beam^{-1}}}}{\Omega_{\mathrm{PSF}}} . \quad (2.13)$$

Uncertainities in $M_{\mathrm{H\,I}}$ were determined by applying `SoFiA 2` uncertainties from Eqn. 2.9 to $M_{\mathrm{H\,I}}$ calculation in Eqn. 2.12 and applying error propagation when determining their logarithmic values

$$\log \sigma_{M_{\mathrm{H\,I}}} = \frac{\sigma_{M_{\mathrm{H\,I}}}}{M_{\mathrm{H\,I}} \ln 10} . \quad (2.14)$$

For the galaxies undetected in H I , 3σ upper limits on H I masses ($< 5\times 10^8$ M$_\odot$) were estimated assuming a linewidth of 200 km s^{-1}.

From these results, the galaxy with the highest H I mass in the group is ESO400-11 on the north-eastern side of Fig. 2.6. The galaxy is an edge-on spiral galaxy with an observed H I flux of 2.03 ± 0.13 Jy km s^{-1} and a corresponding $M_{\mathrm{H\,I}}$ of $M_{\mathrm{H\,I}} = 6.82\times 10^9$

[7] https://rcsed2.voxastro.org/

$M_\odot$. This galaxy also shows a disturbed morphology, a sign of galaxy interaction, and also has a companion, gas-poor galaxy (LEDA 2807038) with a $M_{\rm H\,I}$ upper limit of $M_{\rm H\,I} < 1.57 \times 10^7$ $M_\odot$.

Following this galaxy in H I mass is Klemola 31 A (ESO400-12). Klemola 31 A has a morphology of a barred ocular spiral galaxy with a central oval-shaped region and double spiral arms emanating from both ends of the major axis away from Klemola 31 B. Ocular spiral galaxies are usually short-lived (one rotation) and are sensitive to gravitational tidal effects making them useful for studying galaxy interactions (Elmegreen et al., 1990). Klemola 31 A has a total H I line flux of 0.86 ± 0.08 Jy km s^{-1}, which is consistent with the reported total H I line flux of 0.78 Jy km s^{-1} from Boisse et al. (1988). Klemola 31 A also appears to have a warped H I disk with a large reservoir of hydrogen trailing the far side arm from spiral galaxy B, which is a sign of recent tidal interaction.

The galaxy with the third highest H I mass is LEDA 631562, an optically faint galaxy with a H I flux and mass of 0.40 ± 0.07 Jy km s^{-1}and 1.41×10^9 $M_\odot$ respectively. It has a central H I hole, possibly resulting from the central AGN.

Finally, this brings us to the galaxy with the lowest H I mass in the Klemola 31 group, ESO400-13. ESO400-13 is a lenticular galaxy (S0), an intermediate galaxy between a spiral and elliptical galaxy that has a H I emission line flux and the corresponding H I mass of 0.32 ± 0.06 Jy km s^{-1} and 1.06×10^9 $M_\odot$ respectively. Interestingly, this galaxy also has its H I disk systematically offset from its stellar disk by ~ 14 kpc. Such offsets have been observed in the past in NGC4438 in the Virgo cluster and Arp 105 (Combes et al., 1988; Duc et al., 1997), and shows evidence of its interaction with its environment.

Although the gravitational perturbations in the H I content of the member galaxies of Klemola 31 galaxy group are detected, there is no detection of any intragroup H I. The Klemola 31 galaxy group is an example of a galaxy group at the early stages of evolution, with each member being a different type of galaxy with different morphologies. The morphology of these member galaxies appears to be affected by the interaction with each other or with the environment (Gupta et al., 2018), both processes which may lead to depletion in their H I content and, therefore, the galaxies become deficient.

2.5.2 H I deficiency

A galaxy becomes deficient in H I through mechanisms such as ram pressure stripping or tidal interaction. This deficiency can be quantified as the difference between the expected H I mass ($\log M_{\rm H\,I}^{\rm exp}/M_\odot$) and the observed H I mass ($\log M_{\rm H\,I}/M_\odot$) and can be defined as

$$\mathrm{DEF}_{\rm H\,I} = \log M_{\rm H\,I}^{\rm exp}/M_\odot - \log M_{\rm H\,I}/M_\odot \qquad , \qquad (2.15)$$

where the observed H I mass, $\log M_{\rm H\,I}/M_\odot$, results from measurements and expected

H I mass, $\log M^{\rm exp}_{\rm H\,I}/{\rm M}_\odot$, from the B-band luminosity ($L_{\rm B}$) in the scaling relation (Jones et al., 2018a)

$$\log M^{\rm exp}_{\rm H\,I}/{\rm M}_\odot = {\rm X}\log\left[L_{\rm B}/{\rm L}_\odot\right] + Y \qquad , \tag{2.16}$$

where X and Y are the gradient and intercept for different galaxy morphologies determined from Jones et al. (2018a) while ${\rm L}_\odot$ is the solar luminosity. The B-band Luminosity ($L_{\rm B}$) can be derived from

$$\log\left[L_{\rm B}/{\rm L}_\odot\right] = 10 + 2\log\left[D_L/{\rm Mpc}\right] + 0.4(M_{{\rm bol},\odot} - B^{\rm c}) \qquad , \tag{2.17}$$

where $D_{\rm L}$ is the luminosity cosmological distance, and the bolometric absolute magnitude of the Sun is $M_{{\rm bol},\odot} = 4.88$ (Lisenfeld et al., 2011). The corrected B-band magnitude ($B^{\rm c}$), obtained from HyperLeda[8], is the B-band magnitude (B) that has been corrected for galactic extinction (ac), internal extinction (ai) and k-correction as detailed in Eqn. 2.18

$$B^{\rm c} = {\rm B} - {\rm ac} - {\rm ai} - {\rm ak(t).v}/10000 \qquad . \tag{2.18}$$

For comparison, a second approach to determining the expected H I mass, $\log M^{\rm exp}_{\rm H\,I}/{\rm M}_\odot$, from the stellar masses calculated using WISE W1 (3.35μm) and W2 (4.6μm) magnitudes (Cluver et al., 2014) and shown in Table. 2.1 was taken (Bok et al., 2020)

$$\log\left[M^{\rm exp}_{\rm H\,I}/{\rm M}_\odot\right] = 0.44\times\log M_\star/{\rm M}_\odot + 5.19 \qquad . \tag{2.19}$$

The deficiency parameter (${\rm DEF}_{\rm H\,I}$) can be either positive or negative, with negative values implying an observed H I excess, whereas a positive value acts as a sign of H I deficiency. In order to account for the intrinsic scatter in literature, a galaxy is considered deficient when its deficiency parameter ${\rm DEF}_{\rm H\,I} > 0.2$ - 0.3 dex.

In our most extreme case, ESO400-13 shows the maximum H I deficiency with ${\rm DEF}_{\rm H\,I} = 0.84$ from the B-band luminosity and 1.02 from the stellar mass calculation. This comes as no surprise, considering it is the same galaxy exhibiting a H I displacement from its optical disk.

2.5.3 H I mass size relation

The H I mass size relation can visually show this galaxy or group deficiency by checking for truncation in these galaxies. To check for truncation, the measured H I diameters of these galaxies, red (filled), are compared to the expected H I diameters, blue (open), as shown in Fig. 2.7.

In order to determine H I diameters, an ellipse was fitted to the H I column density contour maps corresponding to 1 ${\rm M}_\odot$ pc^{-2} = 1.25×10^{20} cm^{-2}. From this fit, albeit

[8] http://leda.univ-lyon1.fr/

not perfect (Fig. 2.13), ESO400-11 has the largest H I diameter = 44.7 kpc, followed by Klemola 31A or ESO400-12 with a H I diameter of 38.02 kpc; a value consistent with measurements from Carilli & van Gorkom (1992). LEDA 631562 has a H I diameter of 28.8 kpc, and ESO400-13 came in last with a H I diameter of 23.4 kpc.

The expected H I diameters were computed using Equation 2 from Broeils & Rhee (1997)

$$\log D_{\mathrm{H\,I}} = (1 \pm 0.03) \log D_{25} + (0.23 \pm 0.04) \qquad , \tag{2.20}$$

where the optical diameters D_{25}, shown in Table 2.1, were adopted from HyperLeda. The D_{25} values were calculated from the extinction-corrected logdc diameter; derived from the homogenized logd25 diameter standardized at the isophotal level B = 25 mag arcsec^{-2}.

From Fig. 2.7, the members of the Klemola 31 galaxy group are significantly truncated with respect to their optical disk, with the largest discrepancy seen in ESO400-13 whose $D_{\mathrm{H\,I}}$ / D_{25} = 0.56 further supporting the notion that H I gas is being removed from this galaxy at a much faster rate.

2.5.4 H I kinematics

To assess kinematics, the global spectra of each galaxy, detected in H I and centred on each galaxy's optical redshift, were compared as shown in Fig. 2.8.

These global velocity profiles were derived using `SoFiA`. However, in principle, they can also be determined from a subcube centred on a H I detected galaxy by summing along the right ascension (i) and declination (j) axes of the spectral subcube:

$$V_i = \Sigma_{i=1}^{M} \Sigma_{j=1}^{N} S(i, j) \qquad . \tag{2.21}$$

As can be seen in Fig. 2.8, ESO400-13 is only detected on the blue-shifted side albeit having a double horned profile, further supporting the notion that the H I gas in ESO 400-13 is experiencing more severe interaction effects compared to the other member galaxies of Klemola 31. Klemola 31A and ESO400-13 also have a kinematic asymmetry compared to the two other galaxies. Such asymmetries could arise due to one of the three different environmental mechanisms: (i) ram-pressure stripping, (ii) gas accretion from the neighbouring filaments, and (iii) galactic interaction (e.g. de Blok et al., 2014; Elagali et al., 2019).

ESO400-13 is also seen to have an irregular spectrum and a velocity field in Fig. 2.9. Fig. 2.9 shows the first three moments of individual H I data cubes. These moments correspond to the surface density, velocity field and velocity dispersion.

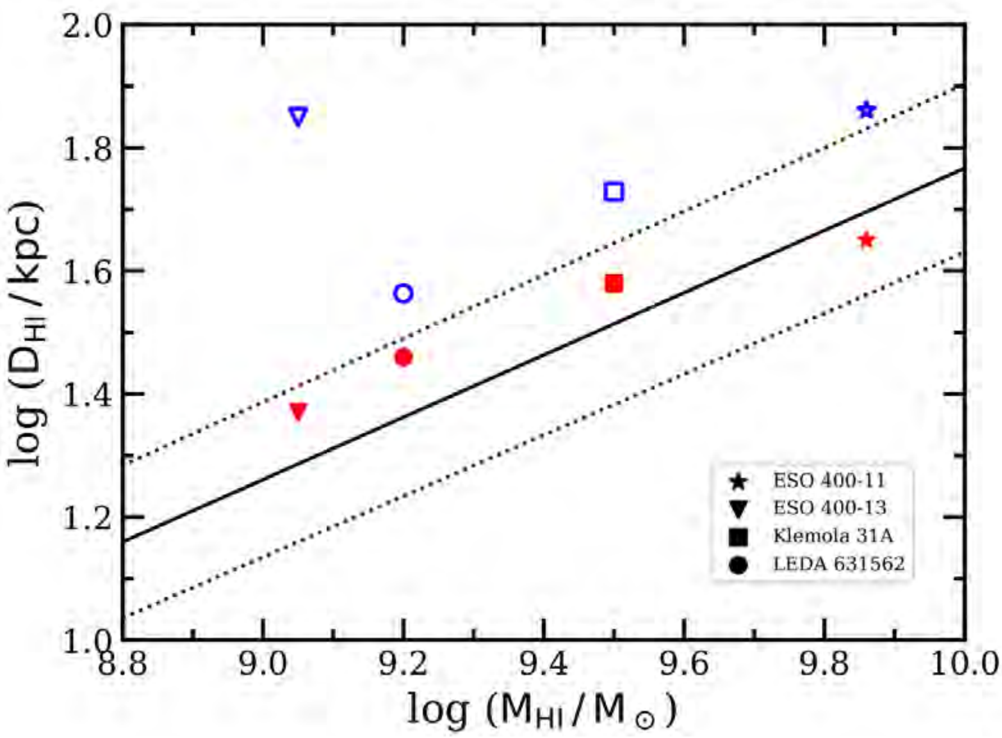

Figure 2.7: H I mass-size relation for H I detections. The solid line represents the best-fit linear relation from Wang et al. (2016) while the dashed lines represent the 3σ scatter. The red (filled) symbols represent $D_{\mathrm{H\,I}}$ and $M_{\mathrm{H\,I}}$ based on our measurements. The blue (open) symbols represent the predicted $D_{\mathrm{H\,I}}$ from the D_{25} based on the relation in Broeils & Rhee (1997).

.

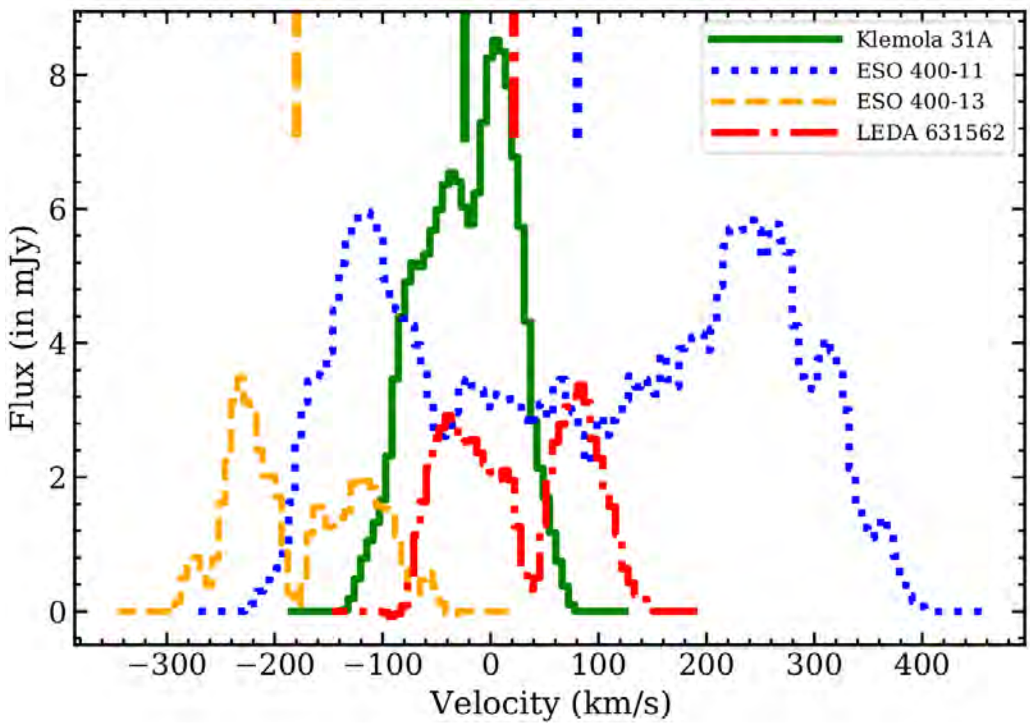

Figure 2.8: Global velocity profiles for ESO400-11, Klemola 31A, ESO400-13 and LEDA 631562. The velocities of these galaxies have been shifted with zero corresponding to z_g (shown in Table 2.1) while the dashed vertical lines represent $z_{\text{H I}}$.

.

Regarding Klemola 31A, there is a characteristic distortion in its southeast extension, possibly due to the concurrence of emission and absorption in front of PKS2020-370. Klemola 31A also has a South West tidal extension displaying recession velocities (red in the middle column of Fig. 2.9) and therefore suggesting that the extension is not in the same plane as the galaxy. It is possible that the interaction with Klemola 31B dragged out H I gas from Klemola 31A that now appears as this tidal extension.

ESO400-11 also has tidal extensions seen on the surface density map in Fig. 2.9. These tidal extensions show signs of tidal interaction between ESO400-11 and LEDA 2807038.

In contrast to these galaxies, LEDA 631562 has the most regular velocity field of the four galaxies, despite the central depression in H I.

2.5.4.1 The Tilted-Ring Model

To further investigate the morphology and kinematics of Klemola 31A, a tilted-ring model was made using `TiRiFiC` as discussed in the tilted-ring subsection 1.5.3.1. In order to model Klemola 31A, a cutout (sub-cube) around the galaxy's position was made, as shown in Fig. 2.11, in order to isolate the galaxy from the galaxy group to increase the processing speed. The Fully Automated `TiRiFiC` (Kamphuis et al.,

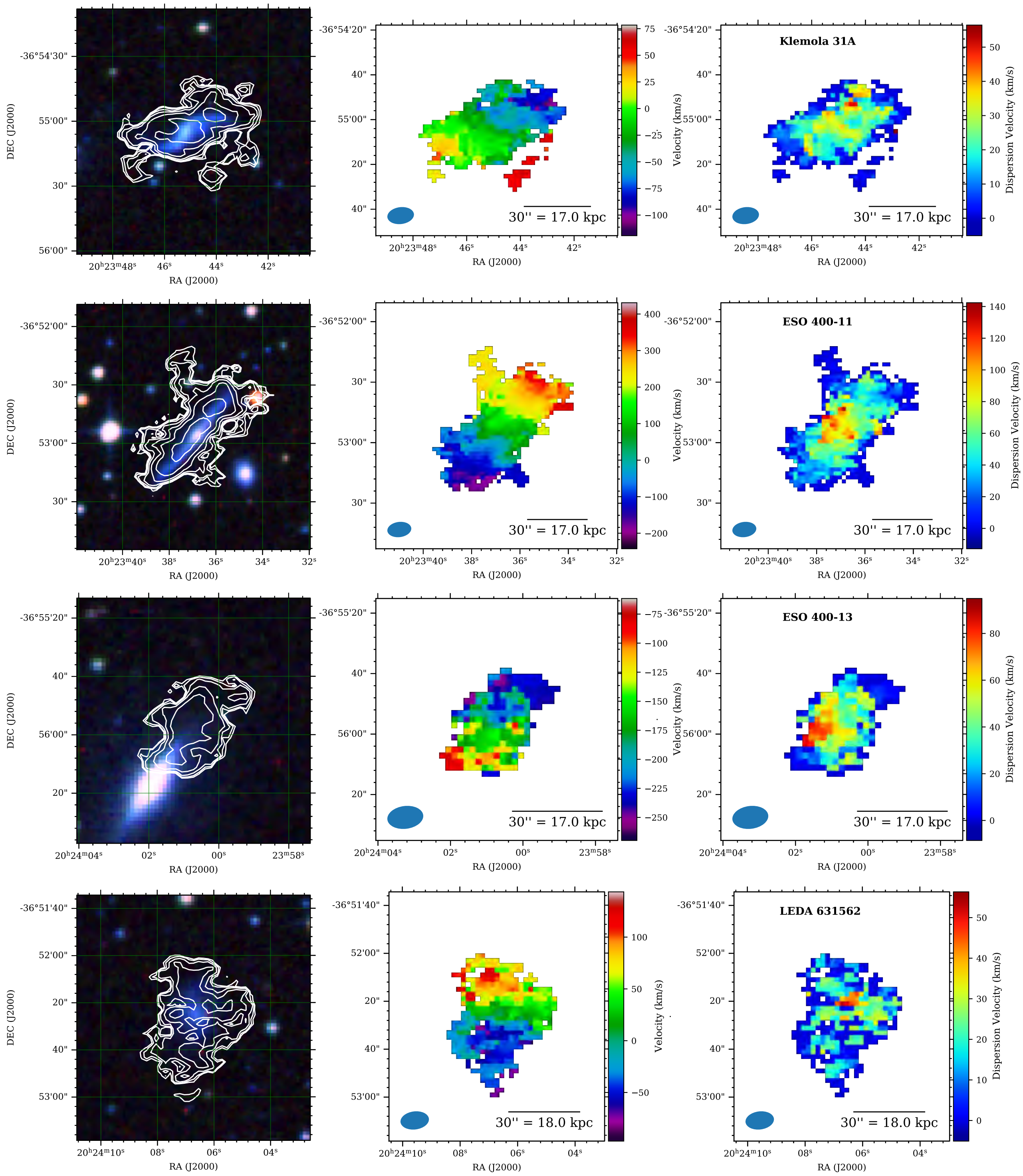

Figure 2.9: Moment maps representing the H I column density (moment-0) contours plotted over RGB cutouts from the optical DSS image (left), moment-1 maps (middle) and moment-2 maps (right) of four detected H I sources, Klemola 31A, ESO 400-11, ESO 400-13, and LEDA 631562. The zero of the velocity scales in middle panels are defined with respect to z_g based on the optical spectra (Table 2.1). The contours in the middle panels correspond to H I column densities of $2^n \times 5 \times 10^{19}$ cm^{-2} (n = 0, 1, 2, 3, ...). The MeerKAT restoring beam of 11.9″ × 7.6″ (6.9 kpc × 4.4 kpc) and a spatial scale bar of 30″ are also shown in the middle and right panels.

2015) software was later applied in order to get the initial kinematic and morphological parameters that would be subsequently optimised in `TiRiFiC` (Jozsa et al., 2007) by simulating a spectroscopic 3D data cube in the following manner.

The four tilted-ring parameters, rotation velocity, inclination angle, position angle, and surface brightness, were distributed on nodes at radii between $R = 0''$ and $R = 56''$ and automatically optimised. Akima interpolation was used in between single nodes while the nodes at the edge of the disk, that is, $R = 0''$ and $R = 56''$ were chosen to assume the value of the closest nodes, implying that the rotation curve is approximately flat. This was done for rotation velocity, inclination angle and position angle. The surface brightness was chosen to taper off to a value of 0 at the outermost radius $R = 56''$. Finally, the systemic velocity, dispersion and central position were fitted to be constant with radius.

The final values and corresponding errors were estimated using a bootstrap method that involved shifting the single nodes of the converged model multiple times by a random value and then re-starting the fitting process. Thereafter, the means and standard deviations were calculated for each model parameter as described in Józsa et al. (2021). After several combinations of parameters and calculating errors as described above, we arrived at a slightly warped disk parametrised as shown in Fig. 2.10. This slightly warped disc model was simulated and overplotted on top of the original data as shown in Fig. 2.11.

Fig. 2.11 shows every second channel of the MeerKAT data cube with the `TiRiFiC` model data cube overlaid on top (pink contours) and the continuum image of PKS2020-370 shown in green. For comparison, the MeerKAT contours are also plotted in blue, while the absorption is seen in red. The light blue and dashed contours from the MeerKAT data cube correspond to $2\sigma_{\rm rms}$ whereas the blue and pink MeerKAT and `TiRiFiC` contours correspond to $1, 2$ and $4\sigma_{\rm rms}$. The green radio continuum contours correspond to 200 and 400 mJy beam^{-1}. Because of the high signal-to-noise ratio in the cube, attributed to the cube's high spectral resolution, we get a reasonable match with the data.

2.6 H I Absorption

H I absorption is also detected in the sightline of PKS2020-370 in both the MeerKAT and GMRT spectra. The spectrum extracted from GMRT data had a much higher spectral resolution of 1.88 km s^{-1} compared to MeerKAT's $\sim$ 5.7 km s^{-1}. Consequently, the GMRT spectrum was smoothed by three channels to match the MeerKAT spectral resolution. The smoothed GMRT spectrum, as well as MeerKAT's spectrum, have been plotted in the top and middle panels of Fig 2.12 respectively.

As can be seen, the absorption signal in the MeerKAT spectrum is contaminated by the emission line from neutral H I 21-cm (middle panel of Fig. 2.12). This contamina-

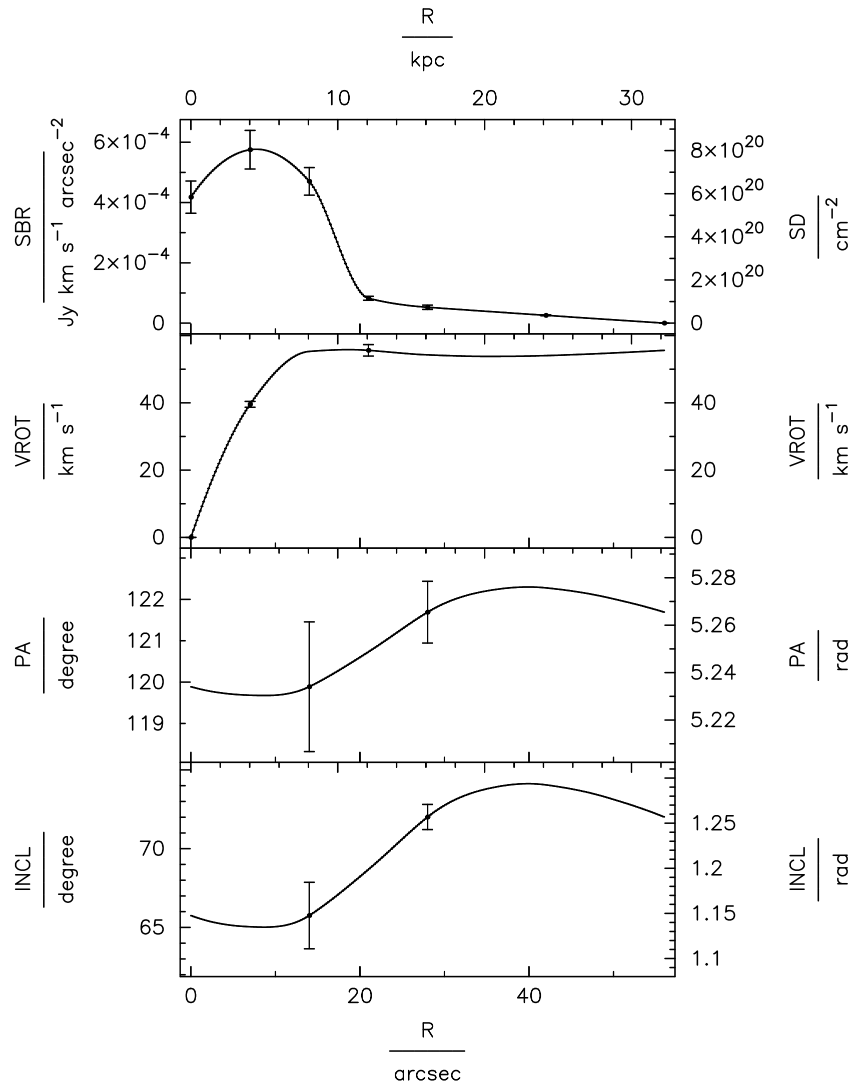

Figure 2.10: `TiRiFiC` tilted-ring model of the H I disk of Klemola 31A. The curves are spline fits, the edge points having the same value as the last data point for each parameter. SBR: surface brightness. SD: surface column density. VROT: rotation velocity. PA: position angle. INCL: inclination.

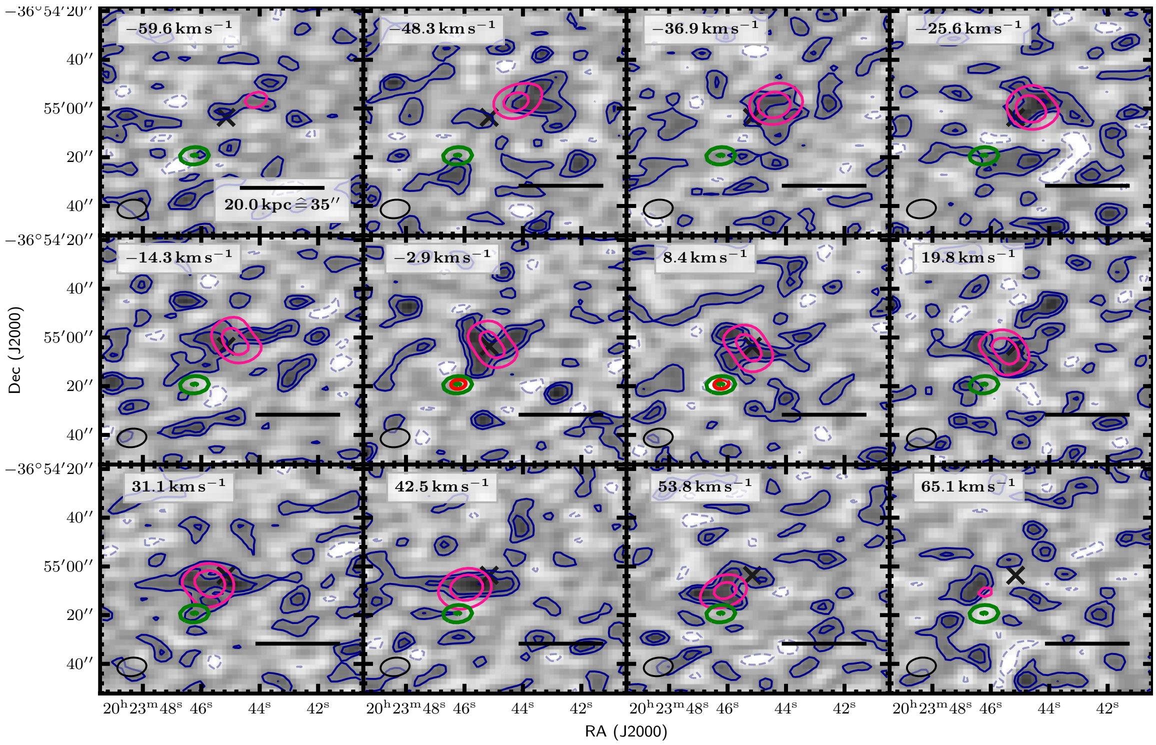

Figure 2.11: H I data cube resulting from the MeerKAT observations (blue contours and greyscale), `TiRiFiC` model data cube (pink contours), and continuum image of PKS 2020-370 (green contours). Every second channel of the data cube is shown. The velocity is measured relative to $z = 0.0287$ at the peak velocity of the absorption feature against PKS 2020-370. The red ellipses mark channels in the velocity range of the absorption feature ($FWHM \approx 16\,\mathrm{km\,s^{-1}}$). Dark grey cross: centre of `TiRiFiC` model. Contours corresponding to line emission scale by $\sigma_{\rm rms} = 0.79\,\mathrm{mJy\,beam^{-1}}$. Light blue and dashed contours (MeerKAT data cube): $-2\,\sigma_{\rm rms}$. Blue and pink contours (MeerKAT data cube and `TiRiFiC` model): 1, 2, $4\,\sigma_{\rm rms}$. Green contours (radio continuum): 200, $400\,\mathrm{mJy\,beam^{-1}}$. The black ellipse in the lower left corners of the channel maps denotes the synthesized beam at half power.

tion is less evident in the GMRT spectrum (top panel of Fig. 2.12). Simply using the frequency regions marked in blue in the top GMRT and middle MeerKAT spectra in Fig. 2.12 results in an optical depth measurement of $\int \tau dv = 0.13 \pm 0.04$ km s^{-1} and $\int \tau dv = 0.09 \pm 0.02$ km s^{-1} respectively.

Given that MeerKAT is more sensitive to H I emission than GMRT, we focused on using MeerKAT data. The contamination within MeerKAT data was accounted for by first masking the frequency channels detected in absorption, as shown in the shaded blue regions of Fig. 2.12 middle panel. Once masked, the emission was estimated by modelling emission in the remaining channel using a single Gaussian component shown as a dotted line in the middle panel of Fig. 2.12. This modelled Gaussian emission was subtracted from the original MeerKAT absorption profile, resulting in the bottom panel profile giving an optical depth measurement of $\int \tau dv = 0.26 \pm 0.03$ km s^{-1} . This

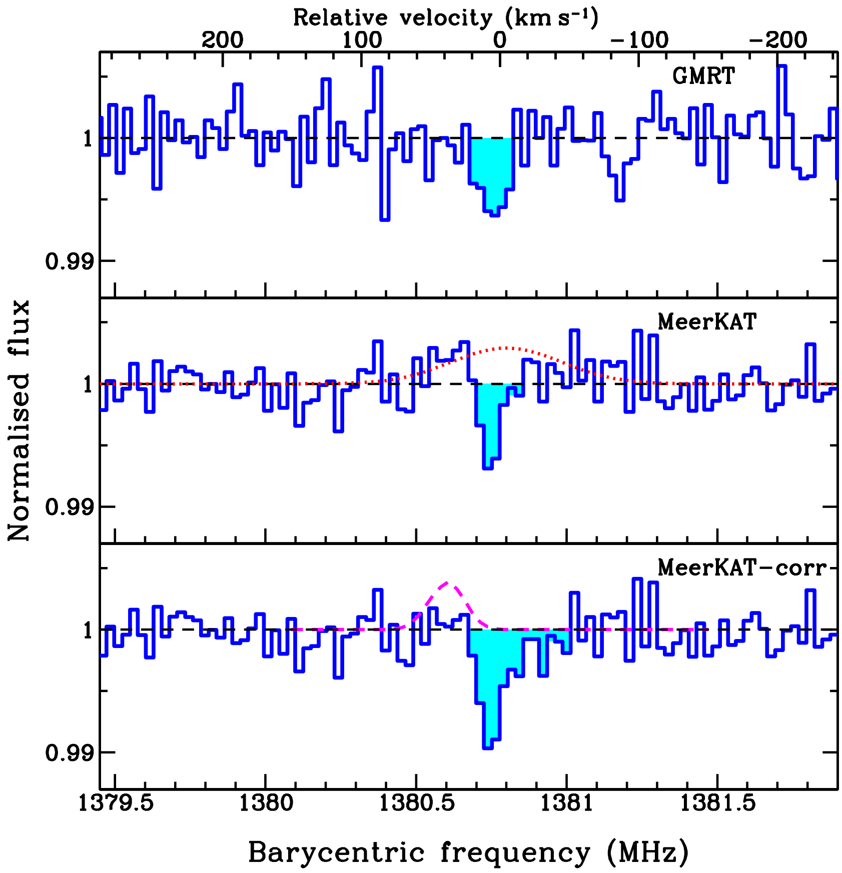

Figure 2.12: H I 21-cm absorption towards PKS 2020-370 (spectral resolution $\sim$5.7 km s^{-1}). The zero of the velocity scale is defined with respect to the peak of the absorption i.e., $z_{21cm} = 0.0287$. The dashed line in the middle panel represents the model for the H I emission. The bottom panel shows the absorption profile corrected using this model (see text for details). Overplotted in magenta is a predicted emission line profile based on the model of a regularly rotating disk. The model has been constructed by fitting a tilted-ring model to the data cube, as described in Sect. 2.5.4.1.

integrated absorption matches well with the VLA-A configuration measurements to within 1 σ (Carilli & van Gorkom, 1987).

Given the calculated optical depth value from MeerKAT observations, the spin temperature of the intervening H I gas was then derived by determining the column density and covering factor. Specifically, assuming that the observed H I gas is optically thin, the H I 21-cm optical depth is related to the spin temperature T_s, covering factor f_c and optical depth through

$$\frac{N(\mathrm{H\,I})}{\mathrm{cm}^{-2}} = 1.823 \times 10^{18} \frac{T_s}{\mathrm{K}} \frac{1}{f_c} \int \tau(v) \frac{dv}{\mathrm{km\,s}^{-1}} \quad . \tag{2.22}$$

Based on the WISE mid-infrared colours, PKS 2020-370 can be classified as a blazar (D'Abrusco et al., 2019; Gupta et al., 2021). It also has a flat spectral index, $\alpha \approx 0.2$, over 0.8 - 20 GHz. Both of these suggest that the radio emission is core-dominated. The milliarcsecond scale images at 2.3 GHz recovers 85% of the total flux density (Petrov & Kovalev, 2017), of which 90% is in the central 'core-jet' component with an extent of $0.015''$ (9 pc at $z_{grp} = 0.029$). The typical sizes of Cold Neutral Medium (CNM) clouds producing H I 21-cm absorption is > 5 pc and they may be part of cold gas structures that extend beyond ~35 pc (Gupta et al., 2018). Further, constraints on the covering factor can only be obtained through milliarcsecond scale resolution spectroscopy (see also Srianand et al., 2013b).

Here, assuming a covering factor of $f_c = 1.0$ and taking the single Gaussian component fitted in the middle panel of Fig. 2.12 to have a column density of H I 21-cm column density $N_{\mathrm{H\,I}} = 1.4 \times 10^{21}$ cm^{-2}, and the corrected optical depth of $\int \tau dv = 0.26 \pm 0.03$ km s^{-1} , we derive a spin temperature limit of $T_s < 2950$ K. Given that MeerKAT data had a spatial resolution of 6.9 kpc $\times$ 4.4 kpc, the spin temperature cannot be compared with absorption if there are inhomogeneities and clumpiness and therefore only acts as a conservative upper limit.

This necessitated another approach where `TiRiFiC` was used to simulate an artificial, high-resolution spectroscopic data cube from the model parameters fitted for in section 2.5.4.1. This simulated data cube has a pixel size of $0.2''$ and a half-power-beam-width of $0.6''$ allowing us to make a column density map unaffected by beam smearing effects, Fig. 2.13, and later determined the column density in the sightline of PKS2020-370 as $N_{\mathrm{H\,I}} = 2.5 \times 10^{20}$cm^{-2}. With this H I 21-cm column density and an optical depth of $\int \tau$dv $= 0.26$ km s^{-1} and in combination with Eqn. 2.22, we get a spin temperature $T_s = 530$ K for a homogenous regularly rotating disk. The spin temperature assumes that the absorbing gas is in the galaxy disk at the sightline of the quasar and, hence, only takes into account the morphology and not the kinematics.

To verify whether the absorption profile arises from the galaxy disc, an emission profile was taken from the simulated column density data cube at the sightline of the quasar PKS2020-370 and plotted next to the MeerKAT absorption profile corrected for emission (bottom panel of Fig. 2.12).

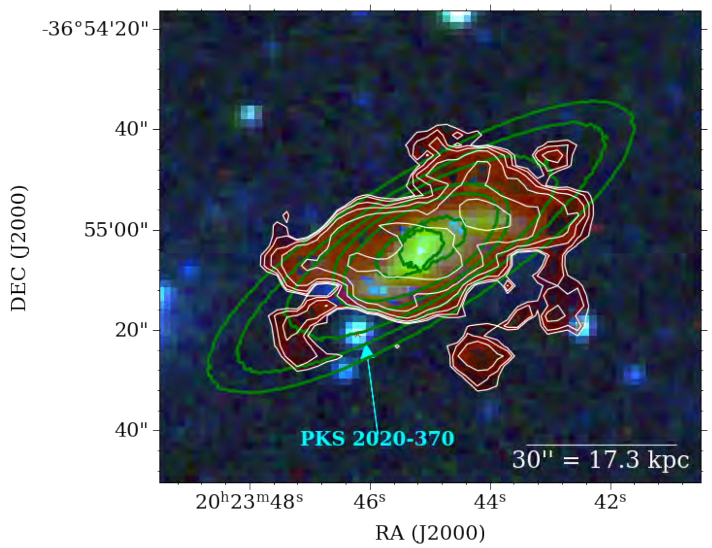

Figure 2.13: Observed moment-0 map of Klemola 31A in autumn colour gradient (increasing N(H I) from brown to yellow) overlaid on the RGB cutout of DSS image. We also show the observed (white) and `TiRiFiC` tilted-ring model (green) moment-0 contours with the same levels as Fig. 2.9.

Table 2.3: Metal absorption components of Klemola 31A toward PKS 2020-370.

z_{abs}	b (in km s^{-1})	log N(Ca II) (in cm^{-2})	log N(Na I) (in cm^{-2})	Notes
(1)	(2)	(3)	(4)	(5)
0.028661	2.02 ± 1.77	12.08 ± 0.26	11.12 ± 0.11	Tied-b
0.028713	4.47 ± 0.70	12.32 ± 0.09	11.76 ± 0.04	Tied-b
0.028787	3.21 ± 0.70	12.15 ± 0.11	11.74 ± 0.04	Tied-b
0.028611	1.12 ± 1.10	12.44 ± 1.25	–	
0.028840	2.16 ± 1.73	12.14 ± 0.26	–	

This emission profile had a peak value corresponding to a column density of $N_{\rm H\,I}$ $= 2.5 \times 10^{20}$ cm^{-2} and a dispersion velocity of 12.9 km s^{-1}. The peak emission was also found to have an offset to the MeerKAT's corrected peak absorption of 38.0 km s^{-1}. This offset can also be seen in Fig. 2.11, where there is an offset between the spatial positions of the pink contours (`TiRiFiC` model) and the red contour (H I 21-cm absorption) in the central panels. From Fig. 2.11, it can be seen that the absorption line feature has a velocity corresponding to the systemic velocity but not corresponding to the receding (southeast) portion of the disk, as would be expected from our tilted-ring model. The absorption line feature would occur at the edge of the receding side of the disk. This serves as evidence that the absorption line feature is a result of H I gas that is extragalactic.

2.7 Discussion and Summary

2.7.1 Klemola 31A

There are two possible explanations for the anomalous velocity of the absorption feature. Firstly, it might come from a combination of streaming motions due to the spiral arms and velocity perturbations due to tidal interaction. In this scenario, the spin temperature ($T_s = 530$ K), as well as the column-density estimate from our tilted-ring model, might still be valid. However, given a maximal rotation velocity of 56 $\mathrm{km\,s^{-1}}$, and an estimated projected rotation velocity of 53 $\mathrm{km\,s^{-1}}$ (for an inclination of 72°), a velocity offset of 38 $\mathrm{km\,s^{-1}}$ is significant and therefore difficult to justify the occurrence of such strong streaming motions along the spiral arms for a lower mass galaxy.

Alternatively, the gas responsible for absorption may not come from the disc and, therefore of extraplanar origin. In this case, the H I column density would remain unknown and, consequently, the spin temperature. The tidal extension of Klemola 31A towards the SW and seen in recession velocities in Fig. 2.9 might provide an explanation for the source of this extraplanar material in the sightline of the quasar. Assuming there exists a stream of H I debris occurring between Klemola 31A and Klemola 31B with the visible part being the extension to Klemola 31A, the stream should have a velocity between the systemic velocity of Klemola 31B and the tidal feature. Klemola 31B is blueshifted with respect to the absorption line and the tidal feature redshifted.

To further explore the distribution of gas along the line of sight towards PKS2020-370, the Keck/HIRES (High-Resolution Echelle Spectrometer) raw data of PKS2020-370 was obtained from Keck Observatory Archive KOA[9]. This data was processed using `IRAF` to obtain the continuum normalized spectrum. From this spectrum, the Ca II and Na I metal lines associated with Klemola 31A were identified and fitted Voigt profiles using VPFIT[10]. These absorption profiles for both Ca II and Na I and their best fitted Voigt profiles are shown in Fig. 2.14. The Doppler parameter (b) and the column densities of the fitted components are in Table 2.3.

From Fig. 2.14, the Ca II absorption profile is seen in 5 distinct components spanning a velocity range of $\sim$ 80 $\mathrm{km\,s^{-1}}$ that is, from +40 $\mathrm{km\,s^{-1}}$ to -40 $\mathrm{km\,s^{-1}}$ with respect to the absorption $z_{\rm abs} = 0.028725$. In addition to this, Na I absorption is visible in the three central components, two of which coincide with the H I 21-cm absorption. Therefore, the measured velocity spread supports the presence of additional gas components with anomalous velocities compared to the H I disc.

Ca II and Na I absorption is believed to be associated with neutral gas near star-forming regions. In addition to this, the ratio of the column densities of Ca II and Na I can be used to investigate the physical conditions in the neutral gas. For instance, in the Milky Way, we typically observe $N(\mathrm{Na\,I}) > N(\mathrm{Ca\,II})$ (see fig. 9 of Welty et al., 1996).

[9] https://koa.ipac.caltech.edu/
[10] http://www.ast.cam.ac.uk/rfc/vpfit.html

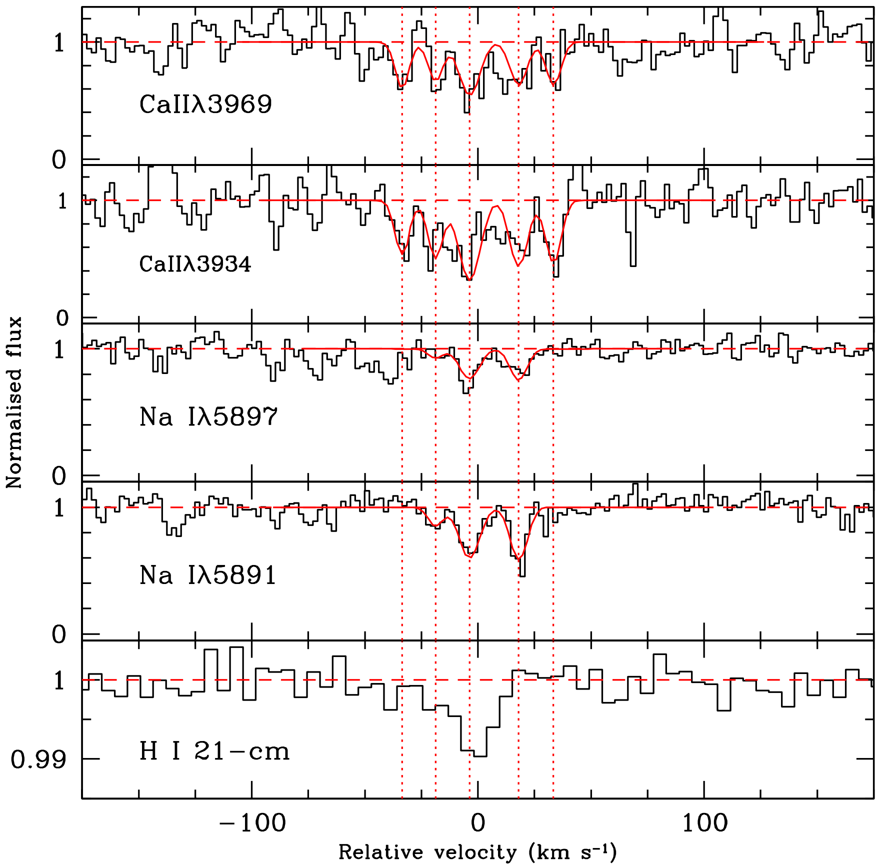

Figure 2.14: Comparison of the absorption profiles Ca II, Na I and H I 21-cm absorption associated with Klemola 31A towards PKS 2020-370. The best-fitted Voigt profiles (components identified with red vertical dotted lines) are over-plotted. The zero velocity scale is defined at $z_{\rm abs} = 0.028725$.

It is common to observe high values of $N(\text{Na I})/N(\text{Ca II}) \geq 1$ in the cold, dense ISM with temperatures $T \leq 100$ K as Ca usually depletes onto interstellar dust grains. This contrasts regions with warmer, diffuse gas with temperatures $T \geq 1000$ K where Ca is mostly in the gas phase.

We observe low $N(\text{Na I})/N(\text{Ca II})$ ratio towards PKS2020-370. Since Na I is not shielded from ionizing radiation, it is possible that the low $N(\text{Na I})/N(\text{Ca II})$ ratio towards PKS2020-370 reflects low radiation field as compared to the Galactic background radiation (Dutta et al., 2017a). Thus, based on the H I kinematics and velocity spread, as well as the observed line ratios, it is possible that the gas responsible for absorption is unrelated to the H I disc.

2.7.2 ESO400-13

ESO400-13 has peculiar characteristics serving as evidence of interaction with its environment. It has its H I disk systematically offset from the stellar disk by ~ 14 kpc. However, it is possible that there is low column density gas below our sensitivity limits in the southeast region devoid of H I. In addition to this, ESO400-13 shows the maximum H I deficiency with $\text{DEF}_{\text{H I}} = 0.84$, and the expected H I size is strikingly larger than its measured size (Fig. 2.7). This comes as no surprise, considering it is the same galaxy exhibiting a H I displacement from its optical disk.

When it comes to kinematics, ESO400-13 has an irregular spectrum and velocity field (Fig. 2.9). It is also only detected on the blue-shifted side (Fig. 2.8) albeit having a double horned profile, shows kinematic asymmetry in the global H I profile, and the velocity dispersion map is unusual and strongly perturbed. This further supports the notion that the H I gas in ESO 400-13 is experiencing more severe interaction effects compared to the other member galaxies of Klemola 31.

2.7.2.1 Argument for ram pressure stripping

From our observations, we do not see a prominent H I bridge/tail that would arise from tidal interactions or minor mergers with other group members. However, there are signs of ram-pressure stripping from ESO400-13, evidenced by significant compressed gas (by a factor of ~ 2) in the receding velocity direction towards Klemola 31A. This is a characteristic signature of ram-pressure stripping, and therefore, ESO400-13 serves as an extreme case of ram-pressure stripping as a result of moving at high velocities in a hot and weak intra-galactic gas (IGM). In addition to this, the H I disk is systematically offset from the optical counterpart.

Chen et al. (2020) show examples of galaxies with H I disks detected on only one side of the galaxy in the Coma Cluster, one example being NGC 4911. However, such observations are unique in galaxy groups as the galaxy would need to cross the group at high velocities due to the low-density IGM in groups, as is our case with ESO400-13. Such a galaxy would experience the ram-pressure (P_{ram}) to be greater than the anchoring self-gravity Π; two quantities that can be modelled following Gunn & Gott III (1972) as

$$P_{ram} = \rho_{\rm IGM} \times v_{\rm gal}^2 \tag{2.23}$$

and

$$\Pi = 2\pi G \Sigma_s \Sigma_g \quad , \tag{2.24}$$

where $\rho_{\rm IGM}$ and $v_{\rm gal}^2$ are the intra-galactic medium density and galaxy velocity; Σ_g and Σ_s are the gas and stellar surface densities of the galaxy, respectively. The stellar surface density can be calculated given the apparent corrected B-band magnitude (B^c) and a co-moving distance of 117 Mpc derived from NED[11] and converted to parsecs (D). We start by calculating the absolute B-band magnitude using Eqn. 2.25

$$M = B^c - 5\log_{10}(\frac{D}{10}) \quad . \tag{2.25}$$

and thereafter proceed to calculate the B-band luminosity, taking the B-band solar magnitude value of 5.48 ($M_{\odot,\rm B}$) as detailed in Eqn. 2.26

$$L_B = 10^{(M_{\odot,\rm B} - M)/2.5} \quad . \tag{2.26}$$

Given its B-R colour of ∼ 1 and using Fig. 1 (d) from Bell & de Jong (2001) to estimate a mass-to-light ratio of unity, we can convert luminosity to stellar mass and finally calculate the stellar surface density, $\Sigma_s \sim 16$ M$_\odot$ pc^{-2} by dividing the stellar mass by the galaxy area given $D_{25} \sim 41.6$ kpc.

When it comes to the gas surface density, we assume the galaxy before stripping had its expected H I mass ($M_{\rm H\,I}^{\rm exp}$) distributed over D_{25} which results in $\Sigma_g \sim 8$ M$_\odot$ pc^{-2}. Taking a typical density of the hot intra-galactic gas of 3×10^{-3} cm^{-3} (Freeland et al., 2008; Rasmussen et al., 2008; Borthakur et al., 2010) and applying Eqns. 2.23 and 2.24 results in a relative velocity of ∼ 200 km s^{-1}. Therefore, ESO400-13 would have to be moving through the group at a relative velocity of ∼ 200 km s^{-1} for the ram-pressure effects to occur in the galaxy.

2.7.2.2 Argument for past tidal interaction

It is worth noting that Zuo et al. (2022) had observed a greater tendency for the H I central velocity of galaxies to deviate from the systemic optical velocity after studying the H I properties of galaxy mergers selected from the Great Observatories All-sky LIRG Survey. We observe this deviation for ESO400-13 in Fig. 2.8. However, we do not observe the single-peaked H I profile expected from such a merger event. In contrast to this, we observe an asymmetrical double-horned profile.

[11] The NASA/IPAC Extragalactic Database (NED) is funded by the National Aeronautics and Space Administration and operated by the California Institute of Technology.

H I asymmetry can be caused by a number of factors in non-merger galaxies, including gas accretion from the galaxy environment, ram-pressure stripping, influence from the dark matter halo, as well as flyby events (please see Mapelli et al., 2008; Sancisi et al., 2008b; Lagos et al., 2018).

The extreme H I deficiency we observe for ESO400-13 makes the gas accretion event unlikely. However, Mapelli et al. (2008) studied NGC 891, a lopsided, edge-on galaxy. From their analysis of its global H I spectrum, it was concluded that the asymmetry observed in the spectrum agreed only with the scenario of ram-pressure and a flyby interaction event. It is possible that ESO400-13 also experienced a flyby event, as well as experiencing ram-pressure as it moved through Klemola 31 group.

2.7.3 Summary

In summary, we have used the wide field of view and large instantaneous bandwidth of the MeerKAT array to identify with high spatial resolution the interstellar medium responsible for the H I absorption in front of the quasar PKS 2020-370. Located in the outer parts of the H I disk of Klemola 31A, the line of sight reveals both emission and absorption, perturbing significantly the derived H I surface density and velocity field of the foreground galaxy. Out of the six identified galaxies of the Klemola 31 group, in the MeerKAT field of view, four are detected and well resolved in H I. Three of them are only slightly perturbed, two through tidal interactions with small companions. They reveal tidal extensions and out-of-the-plane velocities but not significant gas depletion. The fourth one, ESO 400-13, is strongly H I-deficient and reveals a totally asymmetric H I distribution characteristic of ram-pressure stripped galaxies. H I is detected only on the approaching side of the galaxy. This suggests that the galaxy is crossing the group with a high velocity, mainly in the plane of the sky.

Using symmetry arguments and tilted-ring modelling of Klemola 31A, we derive a spin temperature of $T_{\mathrm{s}} = 530\,\mathrm{K}$ for the gas absorbing in front of PKS2020-370. This assumes that the absorption arises from a symmetric disk. This rather high value, unexpected for a disk, as well as the velocity offset of the absorption feature from the expected radial velocity of the disk model, might indicate an extraplanar origin of the absorption feature. One explanation could be that we observe tidal debris as indicated by asymmetric kinematics and morphology of the group members. The same interaction, however, might be responsible for a deviation of the kinematics of Klemola 31A from the assumed circularity of orbits, in which case the discrepancy of the velocities might be due to streaming motions.

Chapter 3

HI gas properties of galaxies in the UGC439 Group from MeerKAT observations

This chapter aims to look at the distribution of the H I content of the galaxy group around UGC 439 in comparison to previous GMRT Telescope studies such as Dutta et al. (2016) using data from the MeerKAT absorption line survey (MALS). It starts by giving an overview of the group in section 3.1. It then discusses the observation, data reduction and source finding in sections 3.2 through 3.4. H I emission and absorption is analysed and discussed in sections 3.5 through 3.6 while the summary is given in section 3.7.

3.1 UGC 439 Galaxy Group

The UGC 439 galaxy group consists of eight galaxies with varying masses, gas distribution and morphological types, as summarised in Table 3.1 and seen in Fig. 3.1. Two of the group members are within a projected distance of ∼150 kpc, at the mean redshift of the group $z_{grp} = 0.0184$, from UGC 439.

The two members are UGC 435 and CGCG 383-072, with a redshift of $z = 0.01826$ and $z = 0.01852$, respectively. H I emission from these two members had been detected using the GMRT radio telescope (Dutta et al., 2016). Using these observations, UGC 435 has an integrated flux of $\int S \mathrm{d}v = 0.52 \pm 0.15$ Jy km s^{-1} and heliocentric velocity of $v_{\mathrm{H\,I}} = 5438$ km s^{-1}, while CGCG 383-072 has an integrated flux of $\int S \mathrm{d}v = 0.76 \pm 0.20$ Jy km s^{-1} and heliocentric velocity of $v_{\mathrm{H\,I}} = 5503$ km s^{-1}. UGC 435 had also been studied using the Nançay radio telescope by Theureau et al. (2007) who found the integrated emission to be $\int S \mathrm{d}v = 2.57 \pm 0.47$ Jy km s^{-1}.

The third member, UGC 439, had been observed as part of the Near Field Galaxy Survey. Jansen et al. (2000b,a) found, in the B-band, a luminosity of $L_B \sim 10.4$ L$_\odot$, an absolute magnitude of $M_B \sim -20.6$, and an optical radius calculated at the 25 mag

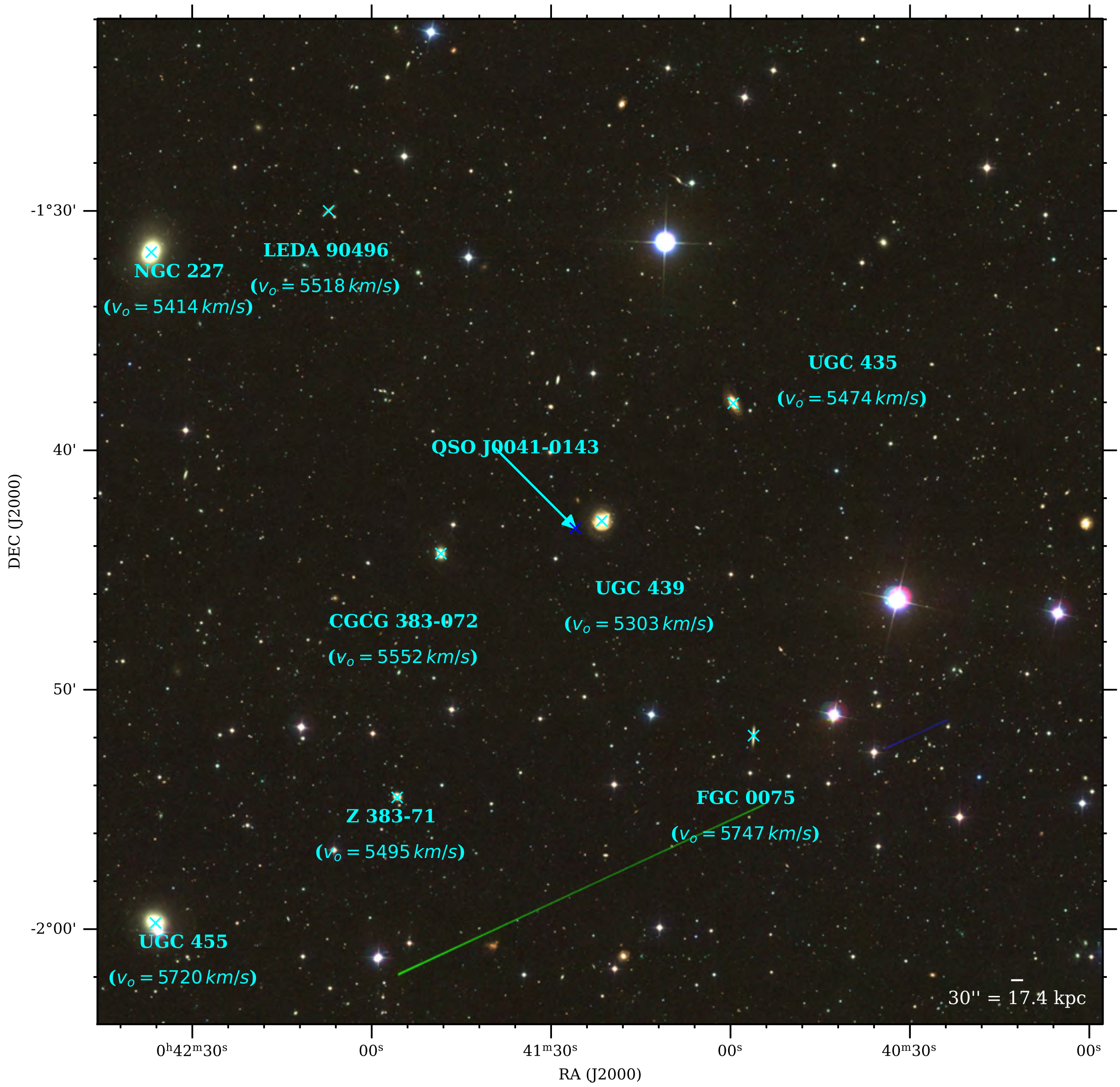

Figure 3.1: SDSS optical image of UGC 439 group. The background optical image comes from the Sloan Digital Sky Survey (SDSS) G, R, and I colour composite images. The recession velocities (v_0 in km s^{-1}) corresponding to z_g are written below the name of the galaxy, with the exception of LEDA 90496 whose redshift remains unknown, and consequently, the mentioned recession velocity is derived from H I measurements. The cyan crosses correspond to the optical centres of these galaxies.

arcsec^{-2} isophote of $r_{25} \sim 36$ arcsec or 13 kpc. When it comes to optical photometry, UGC 439 is face-on with an inclination of $i \sim 0°$, position angle of $PA \sim 170°$. This is contrasted by observations from the Two Micron All-Sky Survey (2MASS), which, from the K_s band photometry, has an inclination and position angles of $i \sim 31°$ and $PA \sim 160°$ respectively (Skrutskie et al., 2006).

UGC 439 has a large and bright central bulge with less defined spiral arms and hence a Sa morphology, and has a stellar mass of log $M_* \sim 10.5$ M$_\odot$ (Kannappan et al., 2013). It is also star-forming with a star-formation rate (SFR) of SFR(H$\alpha \sim 5$M$_\odot$ yr^{-1}) and solar metallicity of log(O/H) + 12 ~ 8.9 (Kewley et al., 2004).

UGC 439 was also observed using the Arecibo single-dish. From these observations, a velocity width of 115 ± 2 km s^{-1} and a total integrated flux density of $\int S dv = 7.07 \pm 0.76$ Jy km s^{-1} (Springob et al., 2005) were determined. The H I mass of UGC 439 was found to be log $M_{\rm H\,I}$= 9.99 ± 0.05 M$_\odot$. In addition to this, UGC 439 was observed to be at a redshift of $z = 0.017686 \pm 0.000005$ and a heliocentric velocity of $v_{\rm H\,I} = 5302 \pm 2$ km s^{-1}. This matches well with the optical spectra derived from the Six-degree-Field Galaxy Survey optical spectra (Jones et al., 2009) which give a redshift of $z = 0.017694 \pm 0.000150$ and a heliocentric velocity of $v_{\rm H\,I} = 5305 \pm 45$ km s^{-1}. There is also a background quasar in the UGC 439 group, J0041-0043, which is an extended radio-loud source at a redshift of $z = 1.679$ and an impact parameter of $b \sim 25$ kpc from UGC 439 forming a Quasar Galactic Pair (QGP).

H I studies of the UGC 439 group revealed sub-kpc scale structures in the absorbing gas with the line of sight velocities dominated by turbulent motion in the region coincident with the extended background radio source J0041-0043 ($z = 1.679$). Dutta et al. (2016) found H I absorption in the southern lobe extending over $\sim$ 2kpc^2 and found a much larger optical depth variations of $\sim$ 4-7 kpc scale towards the core and the northern lobe possibly revealing a patchy distribution of H I. The kinematics of the absorbing gas revealed the gas as being at the kinematical minor axis and co-rotating with UGC 439.

3.2 MeerKAT MALS observations

UGC 439 galaxy group, and specifically, the background quasar, was the target of this observation. The target was observed between 28 to 29 Aug 2019 as part of the MeerKAT Absorption Line Survey (MALS) in the commissioning phase for a combined total of 5.782 hours. The observation time was divided between the primary calibrator, J1939-6342, for $\sim$ 8 minutes interval, the secondary calibrator, J0022+0014, for $\sim$ 4 minute intervals and the target, J0041-0043, for $\sim$ 15 minutes interval. This scheme was repeated four times. The primary calibrator, J1939-6342, was used as the bandpass and flux calibrator; the secondary calibrator, J0022+0014, as the complex gains calibrator.

Observations were carried out in the L-band (900 $\sim$ 1670 MHz) using 60 antennas of

Table 3.1: List of galaxy members of UGC 439 group.

Name	RA	DEC	z_g^+	B mag[†] (mag)	$D_{25}^{\dagger}$ (kpc)	$i_{opt}^{\dagger}$	Morph.[†]	Angular separation (arcmin)	Impact parameter (kpc)	Stellar Mass ($\log M_*$)
(1)	(2)	(3)	(4)	(5)	(6)	(7)	(8)	(9)	(10)	(11)
UGC 439	00:41:21.47	-01:42:57.8	0.0177	13.83	21.6 ± 2.4	12	SBa	-	-	10.29
UGC 435	00:40:59.69	-01:38:01.8	0.0183	15.40	21.2 ± 2.4	61	Sab	7.35	159	9.84
CGCG 383-072	00:41:48.4	-01:44:18.9	0.0185	15.25	16.3 ± 2.6	45	E-SO	6.85	148	10.53
FGC 0075	00:40:56.2	-01:51:55.2	0.0192	16.63	22.8 ± 2.6	80	Sc	11.01	237	9.55
LEDA 90496	00:42:07.2	-01:29:59.2	-	17.56	14.5 ± 2.8	79	Sd	17.29	373	-
UGC 455	00:42:36.3	-01:59:43.4	0.0191	14.77	29.9 ± 2.6	29	E	25.12	542	10.92
Z 383-71	00:41:55.6	-01:54:29.5	0.0183	15.43	-	-	-	14.43	311	9.90
NGC 227	00:42:36.9	-01:31:44.4	0.0181	13.12	41.9 ± 2.4	41	E	21.96	474	11.05

Columns 1 – 3: Galaxy name, position i.e., right ascension and declination (J2000) from SIMBAD. Column 4: redshift of the galaxy obtained from the optical spectra of 6dF Galaxy Survey (6dFGS). Column 5: Total B-band magnitude. Column 6: the extinction-corrected optical diameter measured at the 25th mag arcsec^{-2} isophote from HyperLeda. Column 7: inclination angle calculated from the axis ratio of the isophote at 25 mag arcsec^{-2} in the B-band. Column 8: Morphological type of the galaxy. Column 9: Angular separation from UGC 439. Column 10: Projected distance from UGC 439 using redshift, $z = 0.01769$. Column 11: Stellar masses calculated using WISE W1 (3.35μm) and W2 (4.6μm) magnitudes as described in Cluver et al. (2014)

[†]from HYPERLEDA.

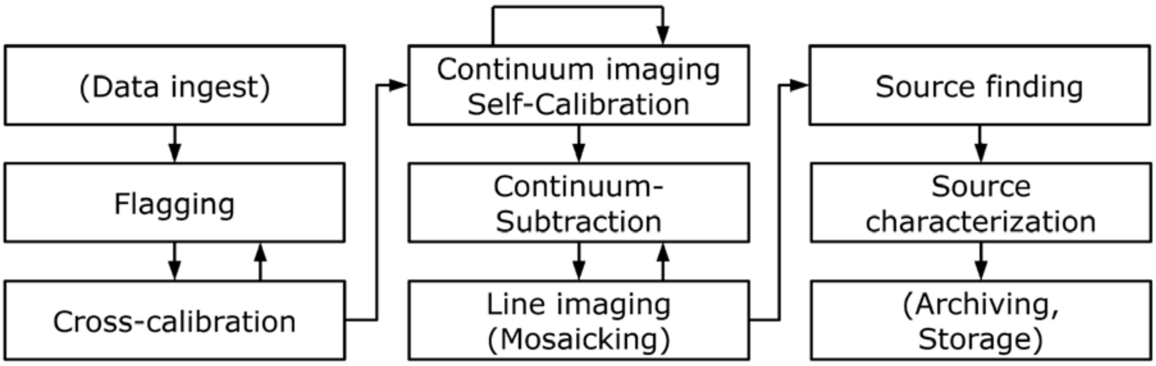

Figure 3.2: Diagram showing CARACal data reduction pipeline steps (Józsa et al., 2020).

the MeerKAT array, with each antenna having a dish diameter of 13.5m. A portion of 1378.46 MHz $\sim$ 1420.26 MHz band was recorded, giving a total bandwidth of 42.01 MHz centred on 1399.36 MHz. The bandwidth was divided into 201, 4k channels, each with a channel width of 208.98 KHz or 44 $\mathrm{km\,s^{-1}}$ (H I).

3.3 Data reduction

For the data reduction, the `Containerised Automated Radio Astronomy Calibration pipeline` (G. I. G. J'ozsa & Andati, 2020) was used following the steps shown in Fig. 3.2. `CARACal`[1] is a platform-independent data reduction software that is publicly available and developed by an international team whose main contributors are Rhodes University, the Italian National Institute for Astrophysics (INAF)-Cagliari and the South African Radio Astronomy Observatory (SARAO). It started out as an imaging pipeline for MeerKAT data, but the focus shifted to implementing it as a generic pipeline capable of reducing data from similar instruments such as the Very Large Array (VLA) and the Giant Metrewave Radio Telescope (GMRT). `CARACal` was used instead of `ARTIP` because `ARTIP` was in the testing phase at the time.

`CARACal` is a python-based script built on the backbone of `stimela`[2]. Consequently, it enables the user to perform different data reduction steps by providing access to standard software, in a standardised syntax, such as `CASA` (McMullin et al., 2007), `SoFiA` (Serra et al., 2015), `AOFlagger` (Offringa, 2010), `PyBDSM` (Mohan et al., 2015), see also (Van Weeren et al., 2012), source finding, `WSCLEAN` (Offringa et al., 2014) among others.

Data processing started by splitting the bandpass and phase calibrators, J1939-6342 and J0022+0014, within `CARACal` from the measurement set in order to flag and later calibrate our calibrator sources first. From there we would obtain the gain solutions

[1] https://caracal.readthedocs.io/
[2] https://github.com/caracal-pipeline/stimela

which we would apply to our target source.

3.3.1 Radio Frequency Interference

The MeerKAT array is located in a remote site in the Karoo with lower levels of Radio Frequency Interference (RFI). The array and the site were constructed to minimise extra RFI spillage from the electronic components of the telescope, as well as the correlators and data processing and storage servers. Additionally, the RFI management team on site utilises multiple tools for monitoring RFI to minimise any potential RFI from the site.

In spite of the measures taken to minimise RFI at the site, there are other unavoidable sources of RFI. These include RFI from aircraft navigation systems, global positioning satellites as well and telecommunications services such as the GSM 900/1800 mobile communication bands and H I emission from our own Milky Way galaxy. Consequently, RFI was flagged from the known frequency ranges, that is, 856 – 880 MHz for GSM 900, 1658 – 1800 MHz for GSM 1800 and 1419.8 – 1421.3 MHz for the Milky Way H I emission. This was followed by using the `AOFlagger` auto flagging algorithm, following the pre-defined *firstpass_ Q.rfis* strategy, to flag the calibrator's uncalibrated visibilities.

3.3.2 Calibration

Calibration within the `CARACal` pipeline is divided into three broad steps (Noordam & Smirnov, 2010): First Generation Calibration (1GC), Second Generation Calibration (2GC), Third Generation Calibration (3GC), which deals with correcting for direction-dependent effects and is not discussed in this thesis because of the field of view of our observation.

3.3.2.1 First Generation Calibration (1GC)

The First Generation Calibration (1GC), also known as cross-calibration or reference calibration, is the process of deriving direction-independent gain solutions from calibrator sources with well-known spectrum and flux properties. These calibration gain solutions are later applied to our target source in order to correct for these direction-independent effects. Therefore, when scheduling observations of a target source, it becomes important to first identify calibrator sources in the field. Thereafter, during observations of the target, the telescope switches between observing the target and the calibrator source, which in our case is the primary calibrator, J1939-6342, and the secondary calibrator, J0022+0014.

3.3.2.1.1 Flux Calibration

To apply a flux calibration, observations of a well-known and modelled, unresolved, constant flux source are required. For our observations, the primary calibrator, J1939-6342, was used as the bandpass and flux calibrator, making it necessary for the source to be very bright in order to obtain a high signal-to-noise ratio in the shortest amount of time. By comparing observations of J1939-6342 to the calibrator source model, the correct flux scales were determined using the `CASA` task SETJY.

3.3.2.1.2 Delay Calibration

Delay errors could be caused by a variety of factors, such as incorrect antenna positions as well as atmospheric effects. These errors result in a linear slope in a phase as a function of the frequency plot per baseline. This phase slope needs to be calibrated out, resulting in an ideal flat slope across the band. This is necessary to prevent decorrelation of the signal during continuum imaging where we average in frequency. Delay calibration was done for both the primary and secondary calibrator sources in two separate steps, using the `CASA` task GAINCAL.

3.3.2.1.3 Bandpass Calibration

Bandpass calibration corrects the frequency response of the telescope. This needs an ideal bandpass calibrator that is bright and unpolarised and has a stable or well-defined spectrum. The source should also be unresolved or have an accurately known model. The primary calibrator, J1939-6342, met these conditions and was therefore used as the bandpass calibrator. The `CASA` task BANDPASS was used to do bandpass calibration. Since the bandpass response of a telescope is usually stable in time, a single (long) solution time interval was used.

3.3.2.1.4 Complex Gains Calibration

The secondary calibrator source, J0022+0014, was selected to be as close as possible to the target source and was also the most observed calibrator source of the two sources. The reason behind this was to track the evolution of local effects or ensure it suffered approximately the same atmospheric effects as the target source. The complex gain solutions obtained from this calibrator source were used to calibrate this source, as well as our target source, by interpolating the solutions.

The calibration steps above resulted in the complex gains and bandpass calibration solutions, which were later applied to the target source. The target source visibilities were thereafter flagged using the `CARACal` FLAG worker and later split out from the measurement set using the `CARACal` TRANSFORM worker.

3.3.2.2 Second Generation Calibration (2GC or self calibration)

The Second Generation Calibration (2GC) improves upon the first-generation calibration by using the target field to calibrate itself. Specifically, it entails creating an image from the 1GC calibration step. This is followed by making a model from this image using tools such as `SoFiA` or the default `CARACal` option `PyBDSF`. Then, the model is used to calibrate the target field by solving for the complex antenna gains using `CubiCal`. These gains are later applied to the target field, and imaging is performed using `WSclean`. This process can be repeated a fixed number of times or used in an iterative process, in which images from consecutive calibration processes are compared. Quality measures are the detected flux density of bright sources or the rms around bright sources as a measure of the dynamic range. Therefore, self calibration attempts to minimise the target residuals, and if done correctly, can improve an image's dynamic range[3] (Noordam & Smirnov, 2010) as well as minimise an image rms.

3.3.3 Continuum Subtraction and Spectral Line Imaging

The self-calibration step enabled us to make a model of the target source, which was a model of the continuum emission that needed to be subtracted from the data. This model was saved in the MODEL_DATA column of the MeasurementSet file, which was later subtracted from the corrected visibilities stored in the CORRECTED_DATA column of the MeasurementSet file and the residuals fitted for using the `CASA` task UVCONTSUB by setting the polynomials to order 3 and subtracting. The resulting continuum subtracted visibilities were written in the CORRECTED_DATA column. The continuum subtracted visibilities were finally imaged using `WSclean` by applying a Briggs weighting scheme with UVTAPER 20 kλ and ROBUST weighting of 0, resulting in a data cube with 400×400 spatial pixels of size $6''$ each and 28 frequency channels, each channel having a resolution of $\sim$ 44 km s^{-1}. This imaged FITS cube had a common restoring beam of $33.5'' \times 28.3''$ with a position angle of 141.2° and an rms of 0.3 mJy beam^{-1} channel^{-1}.

3.4 SoFiA source finding and parametrisation

Source finding for UGC 439 galaxy group used the general procedure discussed in Chapter 2 section 2.4 and outlined in Fig. 2.4. The continuum subtraction step was skipped as the continuum had already been subtracted from the spectral cube.

3.4.1 Noise Normalisation

Upon closer inspection of the spectroscopic cube, it was found to have minor spatial and spectral noise variations. In order to normalise the noise across the cube, noise scaling

[3] The dynamic range is defined as the ratio between the highest peak in an image to the rms. However, should there be artefacts, then it is defined as the ratio of the highest peak in an image to the brightest artefact.

was switched on in `SoFiA 2` by setting *scaleNoise.mode=local*. A kernel of spatial size *scaleNoise.windowXY=71* and spectral size *scaleNoise.windowZ=7* was shifted across all three dimensions of the data cube on a grid that was half the window size since the grid size was not specified. `SoFiA 2` measured an rms value in each window and divided the corresponding grid cell by that rms value. To make sure that there were no sharp boundaries between the grid cells, linear interpolation between the grid cells was enabled by setting *scaleNoise.interpolate=True*.

3.4.2 S+C finder

SoFiA source finding followed the steps detailed in subsection 2.4.5 with a spatial kernel specified as *scifind.kernelXY=(0, 3, 6)* while the spectral kernel as *scifind.kernelZ=(0, 3, 5, 7)* and a threshold of *scifind.threshold=3.5* $\times$ rms. This process resulted in the creation of a raw source mask with the complete number of detections, which were later grouped into sources while discarding false detections based on parameters, as explained below.

3.4.3 Linking

The linking algorithm, explained in subsection 2.4.6, merged together all detections within a distance of 2 pixels in the spatial domain, *linker.radiusXY=2*, and three pixels in the spectral domain, *linker.radiusZ=3*. Once merged, all sources that were found to be smaller than 3 pixels in the spatial domain, *linker.minSizeXY=3*, and three pixels in the spectral domain, *linker.minSizeZ=3*, where each spectral pixel is 44 $\mathrm{km\,s^{-1}}$, were assumed to be false detections and consequently removed. the source radius and size values were found to be the most optimal values needed after a few trials.

3.4.4 Reliability filter

Of the remaining detections, the procedure that followed involved determining how reliable they were as detections. Using a reliability threshold of *reliability.threshold=0.9* enabled filtering out a large number of false detections. The distribution of positive (blue) and negative (sources) in parameter space is shown in Fig. 3.3, where the black dots represent genuine detections.

The density of positive and negative sources was measured by performing a Gaussian kernel density estimation (KDE) on the individual sources in parameter space in Fig. 3.3. The relative size of the Gaussian kernel used in the KDE was set to *reliability.scaleKernel=0.56*.

The integrated signal-to-noise ratio was also used to filter out a majority of false detections, as shown by the grey dashed line in Fig. 3.3. This $\mathrm{SNR_{min}}$ was set to

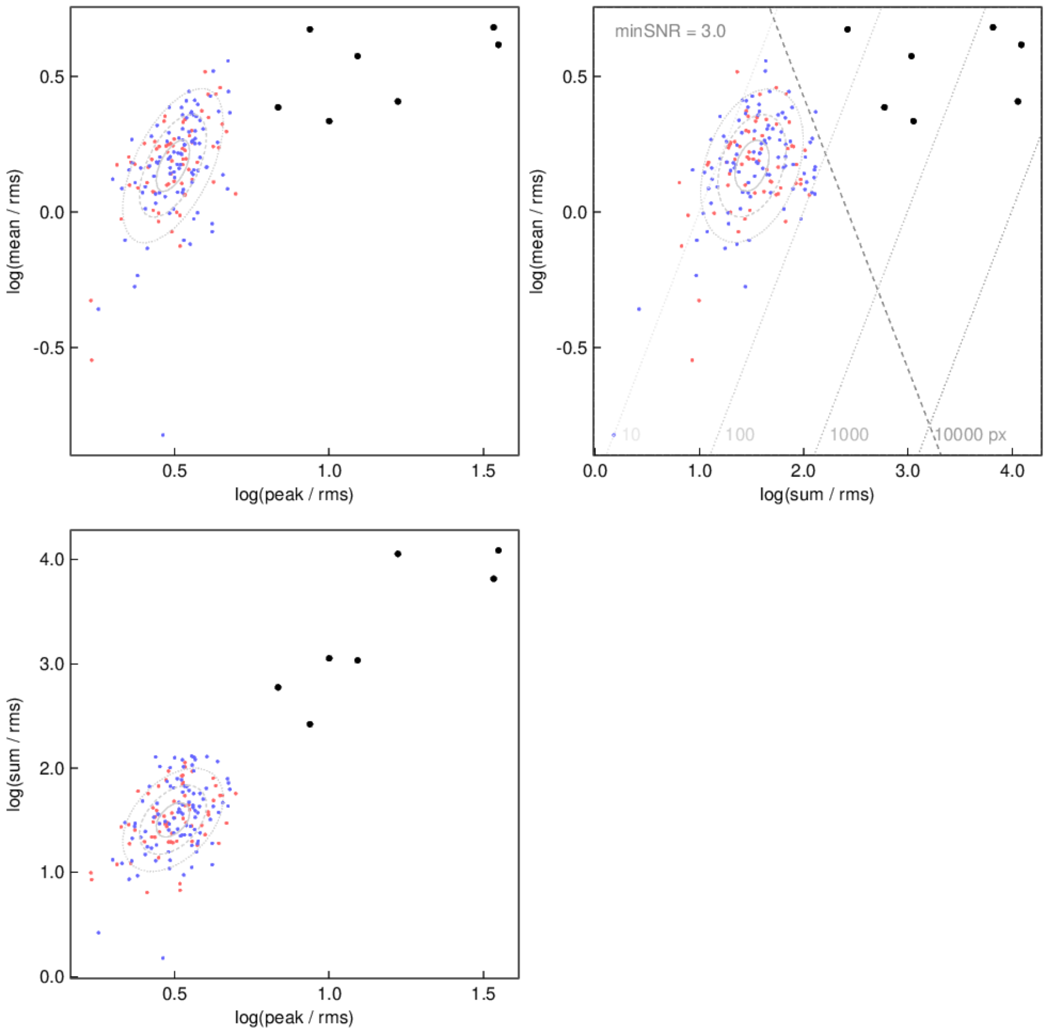

Figure 3.3: Three projections of the three-dimensional parameter space in which SoFiA calculates the reliability of detections. Each projection represents the distribution of positive (blue) and negative (red) sources in parameter space with the black dots representing our genuine sources. The grey dashed line represents the integrated constant signal-to-noise ratio limit of 3.0 below which sources are deemed unreliable and consequently are discarded and light grey ellipses are $1\sigma, 2\sigma$ and 3σ contours of the 3D Gaussian function used in the kernel density estimator (KDE).

reliability.minSNR=3.0. All sources falling below this SNR threshold were filtered out.

3.4.5 Parametrisation

Once reliable sources were determined, `SoFiA 2` proceeded to measure a range of source parameters across the source mask. These parameters were produced in a catalogue format alongside moment maps and mask cubes.

3.5 H I emission

After calibration, imaging and source finding, H I emission was detected in five out of the eight members of UGC 439 group, with two additional H I detections, each having an optical counterpart, albeit no redshift information was available to be used in determining if their redshifts are consistent with the member galaxy's redshift. Aside from the two additional detections, all galaxies seen in H I are spatially resolved at ~ 3 beams, as well as spectrally resolved at ~ 44 km s^{-1}. The detected emission resides in the frequency range $1392.0 - 1397.2$ MHz, corresponding to the redshift range of $z_{\mathrm{H\,I}} \sim 0.016614 - 0.020430$ or a recession velocity ranges of $v_0 = cz_{\mathrm{H\,I}} \sim 4981 - 6125$ km s^{-1}, estimated from the centres of the global H I emission profiles of individual galaxies.

Fig. 3.4 shows these H I detections, as well as the remaining three galaxies undetected in H I. The figure was made using the SDSS g, r and i colour composite image as the background with names obtained from SIMBAD and contours representing H I column densities of $2^{\mathrm{n}} \times 5 \times 10^{19}$ cm^2 plotted using the column density map ($N_{\mathrm{H\,I}}$) made from `SoFiA` total H I intensity map $\int I(v)dv$ Jy km s^{-1} beam^{-1} by applying Eqn. 2.10.

Similar to the figure is Fig. 3.5 with added ellipses drawn on top of the H I contour plots, with red representing the fitted H I ellipse and cyan representing the expected H I ellipse. For each galaxy detected in H I (red ellipses seen in Fig. 3.5) an ellipse was fitted to the 1 M$_\odot$pc^{-2} contour by using the uniformly weighted second-order moment of the pixel positions inside the contour as described in Wang et al. (2013) and later converted to kpc by using the redshifts given in Table. 3.1 as a proxy for each galaxy's distance. The cyan ellipses have only the major axis (expected) H I diameter calculated and consequently are represented as circles. The expected H I diameter was calculated by following Eqn. 2.20 where the D_{25} diameters were determined from HyperLeda and are detailed in Table 3.1. This difference between H I measured and expected diameter is also seen in Fig. 3.6.

Fig. 3.6 shows the H I mass size relation of the galaxies detected in H I. This relation visually shows galaxy group deficiency or excess by comparing the measured H I diameters, red (filled), to the expected H I diameters, blue (open), with the horizontal axis representing the logarithm of the measured H I masses for both the measured and expected diameters. This H I deficiency value can be calculated by finding the differ-

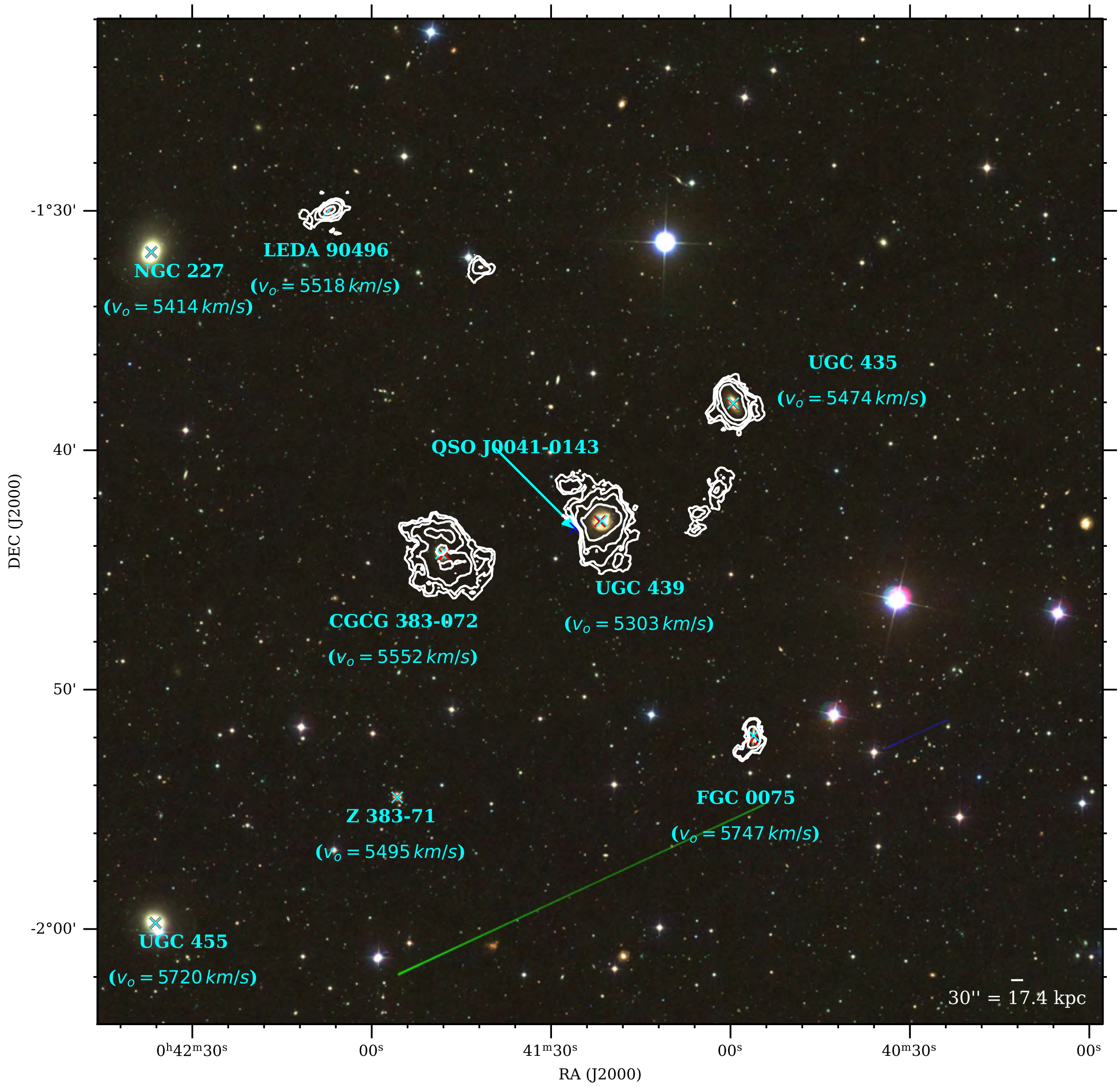

Figure 3.4: 5 of the 8 group members detected in H I. The H I column density contours are derived from the moment-0 map and correspond to H I column densities of $2^n \times 5 \times 10^{19}$cm^2($n = 0, 1, 2, 3$). The background optical image comes from the Sloan Digital Sky Survey (SDSS) G, R, and I colour composite images. The radio image has a restoring beam of $33.4'' \times 28.2''$ with a position angle of 140.2°. The recession velocities (v_0 in km s^{-1}) corresponding to z_g are written below the name of the galaxy, with the exception of LEDA 90496 whose redshift remains unknown, and consequently, the mentioned recession velocity is derived from H I measurements. The red and cyan crosses correspond to the H I and optical centres of these galaxies.The Green line in the background image is an SDSS image artefact.

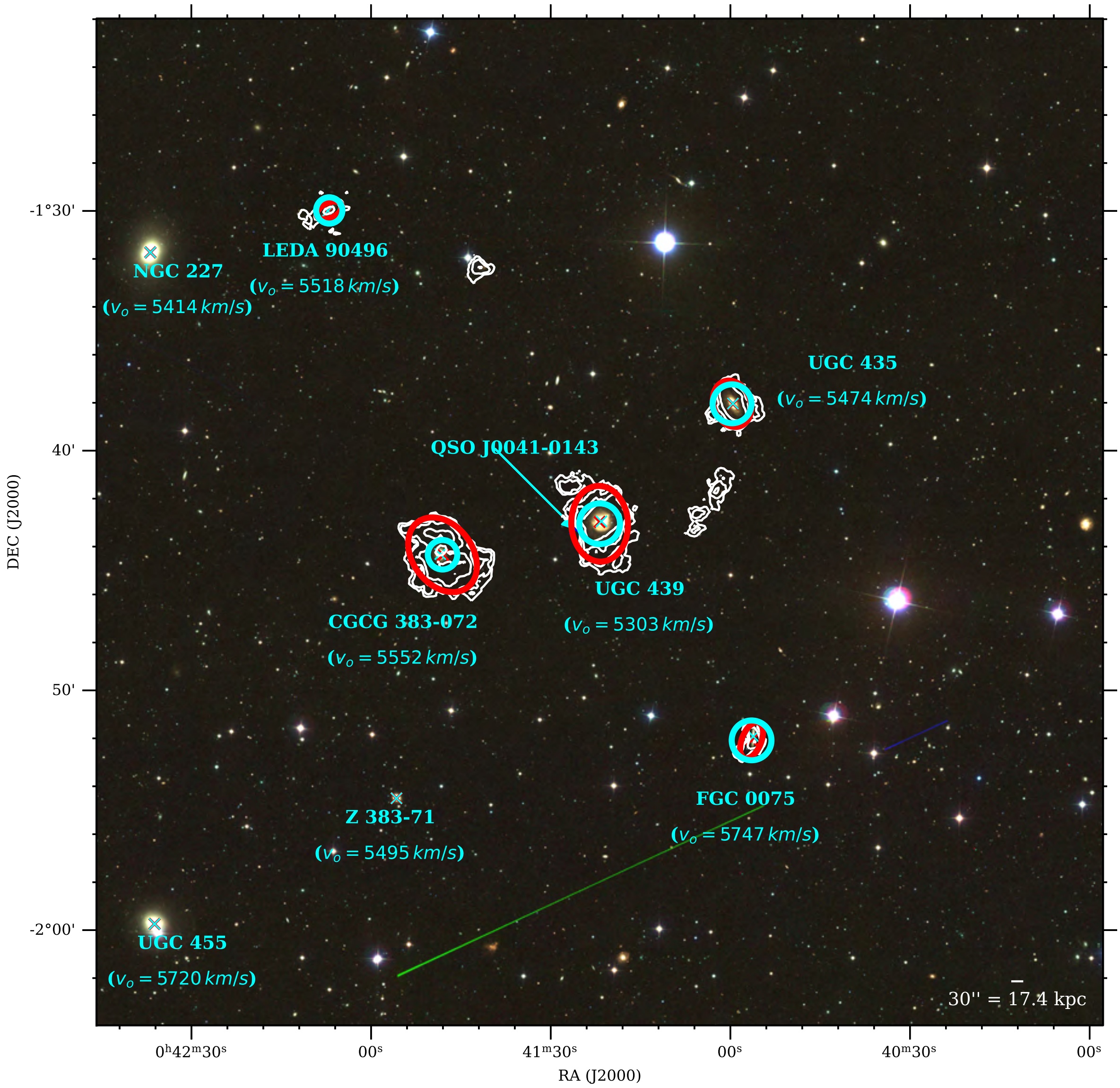

Figure 3.5: 5 of the 8 group members detected in H I, similar to Fig. 3.4, with the fitted (red) as well as expected (cyan) H I diameters plotted as ellipses for visual comparison. The expected H I diameters have been plotted as circles representing only the major axis of the expected H I diameters.The Green line in the background image is an SDSS image artefact.

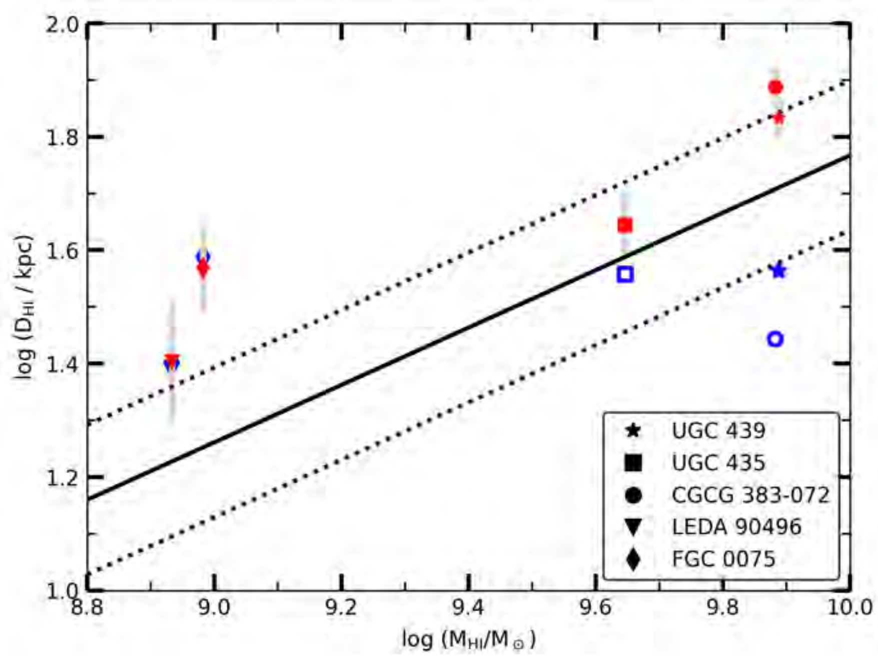

Figure 3.6: H I mass-size relation for five galaxies detected in H I. The solid line represents the best-fit linear relation from Wang et al. (2016) while the dashed lines represent the 3σ scatter. The red (filled) symbols represent $D_{\text{H I}}$ with their uncertainties representing the beam smearing effects on the measured H I diameters and estimated as half a beam width and $M_{\text{H I}}$ based on our measurements. The blue (open) symbols represent the predicted $D_{\text{H I}}$ from the D_{25} based on the relation in Broeils & Rhee (1997).

.

ence between the expected H I mass and measured H I mass, as shown in Eqn. 2.15. The expected H I masses were determined as described in subsection 2.5.2 using Eqn. 2.16 while the measured H I masses were determined using the total H I intensity map $\int I(v)dv$ Jy km s^{-1} beam^{-1} from SoFiA by following Eqn. 2.12. For galaxies undetected in H I 3σ upper limits on H I masses ($5.09 \times 10^8\ M_\odot$) were estimated assuming a linewidth of 200 km s^{-1} (please see Table 3.2). Fig. 3.7 includes information about the logarithm of the expected H I masses in the horizontal axis. The green points represent the expected H I mass and diameter, while the red points represent the measured H I mass and diameter.

As can be seen from both Fig. 3.6 and Fig. 3.7, just over half of all galaxies detected have positive H I deficiencies and consequently, have larger measured diameters compared to expected diameters, while at the same time having their measured mass exceeding their expected mass. This is also seen in Table 3.2 and indicates that the group is in H I excess.

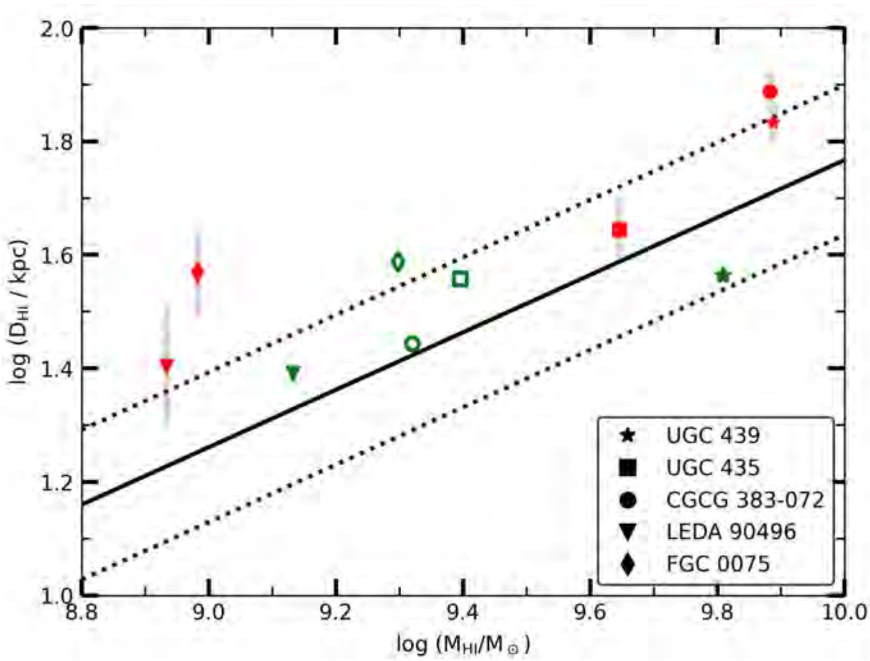

Figure 3.7: H I mass-size relation for five galaxies detected in H I. The solid line represents the best-fit linear relation from Wang et al. (2016) while the dashed lines represent the 3σ scatter. The red (filled) symbols represent $D_{\rm H\,I}$ with their uncertainties representing the beam smearing effects on the measured H I diameters and estimated as half a beam width and $M_{\rm H\,I}$ based on our measurements. The green (open) symbols represent the predicted $D_{\rm H\,I}$ from the D_{25} based on the relation in Broeils & Rhee (1997) as well as the expected $M_{\rm H\,I}$ based on the relation described in subsection 2.5.2 and Eqn. 2.16 (Jones et al., 2018b).

.

3.5.1 H I Mass, size and Morphology

Regarding H I integrated flux and masses, UGC 439 has the highest H I mass and integrated flux of 7.73×10^9 $M_\odot$ and 5.67 ± 0.18 Jy km s^{-1} respectively. The integrated flux had been observed with the GMRT radio telescope as $\int S dv = 1.42 \pm 0.14$ Jy km s^{-1} (Dutta et al., 2016) and the Arecibo telescope as $\int S dv = 7.07 \pm 0.76$ Jy km s^{-1} which translates to a H I mass of log $M_{\rm H\,I} = 9.99 \pm 0.05$ $M_\odot$ (Springob et al., 2005). UGC 439 is a barred spiral galaxy with morphological classification SBa and a B-band optical diameter at the isophotal level 25 mag/arcsec^2 (D_{25}) of 21.6 kpc, making it the fourth largest galaxy in the group, in terms of the optical diameter. UGC 439 has a position angle of 170° from optical B-band observations (Jansen et al., 2000b,a) and 160° from the Two Micron All-Sky Survey (2MASS) (Skrutskie et al., 2006). This is similar to the observed H I position angle of 169.5° (please see Table 3.2). When it comes to the measured H I diameter, UGC 439 has a diameter ($D_{\rm H\,I}$) of 68.2 kpc, therefore making it the second largest diameter in the group. As can be seen in both Figs. 3.5 and 3.7, the galaxy's measured H I diameter is larger than its expected H I diameter, and given that its deficiency parameter is -0.08, this galaxy has H I in excess. This H I excess is similarly evident in the predicted H I mass, calculated based on the stellar mass, with a deficiency parameter of -0.17. It also has H I clumps seen to the North East and South West of the galaxy. As a result of MeerKAT's sensitivity, contrary to Dutta et al. (2016), the H I emission detected from UGC 439 extends up to the sightline of the background quasar. This is shown in Fig. 3.10, where the quasar is represented as a blue cross on top of the velocity map.

Following UGC 439 in H I mass and integrated flux is CGCG 383-072 with 7.63×10^9 $M_\odot$ and 5.12 ± 0.20 Jy km s^{-1} as its H I mass and integrated flux respectively. The integrated flux had been observed with the GMRT radio telescope as $\int S dv = 0.76 \pm 0.20$ Jy km s^{-1} (Dutta et al., 2016). CGCG 383-072 is a lenticular galaxy with morphological classification E-SO and the second largest B-band D_{25} diameter of 16.3 kpc. However, when it comes to measured H I diameter, CGCG 383-072 has a measured H I diameter ($D_{\rm H\,I}$) of 77.2 kpc, making it the largest galaxy in terms of the measured H I diameter while the ratio of H I to optical diameters being 3.16, making its H I diameter about triple the optical diameter. However, it has a smaller expected H I diameter and mass compared to its measured counterparts. This is clearly seen in Figs. 3.6, 3.7 and 3.5. When comparing the expected H I mass to the measured H I mass, it can be seen from Table 3.2 that CGCG 383-072 has a deficiency parameter of -0.56, meaning that this galaxy has H I in excess.

UGC 435 comes in third with H I mass and integrated flux of 4.43×10^9 $M_\odot$ and 3.07 ± 0.14 Jy km s^{-1} respectively. This galaxy had been observed with the Nançay radio telescope resulting in a measurement of the integrated emission of $\int S dv = 2.57 \pm 0.47$ Jy km s^{-1} (Theureau et al., 2007), and also the GMRT radio telescope: Dutta et al. (2016) determined an integrated flux of $\int S dv = 0.52 \pm 0.15$ Jy km s^{-1}. UGC 435 is an intermediate spiral galaxy with morphology Sab and a B-band optical diameter D_{25} of 21.2 kpc, making it the fifth largest galaxy in terms of B-band optical diameter, only slightly smaller than UGC 439. When it comes to the measured H I diameter, UGC 435

Table 3.2: Properties of UGC 439 group members based on H I 21-cm emission line

		UGC 439	UGC 435	CGCG 383-072	LEDA 90496	FGC 0075	H I detection 2	H I detection 3
(1)	R.A.	$00^h\,41^m\,21\overset{s}{.}84$	$00^h\,40^m\,59\overset{s}{.}52$	$00^h\,41^m\,48\overset{s}{.}0$	$00^h\,42^m\,7\overset{s}{.}2$	$00^h\,40^m\,56\overset{s}{.}4$	$00^h\,41^m\,3\overset{s}{.}36$	$00^h\,41^m\,41\overset{s}{.}76$
(2)	Declination	$-1°\,42'\,57''.6$	$-1°\,38'\,2''.4$	$-1°\,44'\,20''.4$	$-1°\,30'\,0''.0$	$-1°\,52'\,4''.8$	$-1°\,42'\,7''.2$	$-1°\,32'\,24''.0$
(3)	$z_{\rm H\,I}$	0.017684	0.018189	0.018484	0.018409	0.019048	0.017670	0.017783
(4)	$v_{\rm H\,I}$ (km s^{-1})	5302	5453	5541	5519	5710	5297	5331
(5)	S (Jy Km/s)	5.67 ± 0.18	3.07 ± 0.14	5.12 ± 0.20	0.58 ± 0.12	0.61 ± 0.09	0.53 ± 0.12	0.24 ± 0.06
(6)	log $M_{\rm H\,I}$ ($M_\odot$)	9.89 ± 0.01	9.65 ± 0.02	9.88 ± 0.02	8.93 ± 0.09	8.98 ± 0.06	8.86 ± 0.10	8.52 ± 0.12
(7)	MAJ_s (arcsec)	189.6	118.9	205.4	67.7	95.3	-	-
(8)	MIN_s (arcsec)	141.8	92.6	149.4	37.0	48.5	-	-
(9)	PA_s (°)	169.5°	25.4°	211.8°	311.9°	1.9°	-	-
(10)	$D_{\rm H\,I}$ (kpc)	68.2±6.0	44.1±6.2	77.2±6.3	25.4±6.2	37.0±6.5	-	-
(11)	$D_{\rm H\,I}/D_{25}$	3.16	2.10	4.72	1.75	1.62	-	-
(12)	log $M^{\rm exp}_{\rm H\,I}$ ($M_\odot$)	9.81 ± 0.21	9.40 ± 0.21	9.32 ± 0.21	9.13 ± 0.21	9.30 ± 0.21	-	-
(13)	DEF ($M_\odot$)	−0.08	−0.25	−0.56	0.20	0.32	-	-
(14)	log $M^{\rm exp}_{\rm H\,I}$ ($M_\odot$)	9.72 ± 0.33	9.52 ± 0.33	-	8.63 ± 0.33	9.39 ± 0.33	-	-
(15)	DEF ($M_\odot$- M_*)	−0.17	−0.13	-	−0.30	0.41	-	-

Columns 1-4: Right ascension, declination, redshift and systemic velocity for every member of the galaxy group detected in H I. Column 5: Integrated flux with uncertainties calculated as explained in the `SoFiA 2` parametrisation section 2.4.8. Column 6: H I mass with uncertainties calculated as explained in the H I mass and morphology section 2.5.1. Columns 7-9: H I discs major axes, minor axes and position angles from `SoFiA 2` in arcseconds. Column 10: H I disc diameters in kpc from an ellipse fitted to the H I column density contour maps corresponding to 1 $M_\odot$ pc^{-2} = 1.25×10^{20} cm^{-2}, with uncertainties representing the beam smearing effects on the measured H I diameters and estimated as half a beam width. Column 11: Ratios of the H I to optical disk diameters. Column 12: Logarithm of the expected H I mass. Column 13: H I deficiencies. Values without uncertainties were taken directly from the `SoFiA 2` parameterization. Since they are not critical for our analysis and `SoFiA 2` does not provide these uncertainties, they are not calculated. Column 14: Logarithm of the expected H I mass based on stellar mass as described in Bok et al. (2020). Column 15: H I deficiencies based on stellar mass as described in Bok et al. (2020).

has a diameter of 44.1 kpc, making it the third largest galaxy in terms of H I diameter while the ratio of H I to optical diameters being 2.10, making its H I diameter about double the optical diameter. Similar to the previous two galaxies, UGC 435 has a larger measured H I mass and diameter compared to its expected counterparts. This can be seen in Figs. 3.6 and 3.7. When it comes to H I morphology, UGC 435 appears to have a regular disk with clumps of H I to both the East and West directions, which is not surprising given that it also has H I in excess with a deficiency parameter of -0.25 from B-band luminosity and -0.13 from stellar mass calculations as can be seen in Table 3.2.

FGC 0075 comes in fourth with H I mass and integrated flux of 9.61×10^8 $M_\odot$ and 0.61 ± 0.09 Jy km s^{-1} respectively. FGC 0075 is a spiral galaxy with morphological classification Sc and a B-band optical diameter D_{25} of 22.8 kpc, making it the third largest galaxy in terms of B-band optical diameter. FGC 0075 has a measured H I diameter of 37 kpc, making it among the least H I diameters measured, being only larger than LEDA 90496 while the ratio of H I to optical diameters is 1.75, making the H I diameter almost similar in size to the optical diameter. However, unlike the previous galaxies, this galaxy has a H I deficiency of 0.32, making it slightly H I deficient. This H I deficiency is similarly evident in the predicted H I mass, calculated based on the stellar mass, with a deficiency parameter of 0.41

Finally, LEDA 90496 has the least H I mass and integrated flux of 8.57×10^8 $M_\odot$ and 0.58 ± 0.12 Jy km s^{-1} respectively. LEDA 90496 is also a spiral galaxy with morphological classification Sd and a B-band optical diameter D_{25} of 14.5 kpc, making it the smallest galaxy in terms of optical diameter. Since there was no redshift information associated with LEDA 90496, the average group redshift value of $z = 0.01844$ was used when deriving LEDA 90496 properties. When it comes to the measured H I diameter, LEDA 90496 has a diameter of 25.4 kpc, making it the least galaxy in terms of H I diameter, with the ratio of H I to optical diameters being 1.62, making the H I diameter also almost similar in size to the optical diameter. LEDA 90496 is also observed to be only slightly H I deficient with a deficiency parameter of 0.20 as seen in Table 3.2.
In comparison to the stellar mass derived deficiency parameter, LEDA 90496 appears to have H I in excess with a deficiency parameter of -0.30. Given that we do not have the spectroscopic redshift for this galaxy needed to calculate its B-band expected H I mass and, consequently, its deficiency parameter, it is possible that this discrepancy in the deficiency parameter comes from our decision to use the group redshift.

The remaining galaxies not detected in H I are NGC 227, an elliptical galaxy with morphological classification E, which has the largest D_{25} diameter of 41.9 kpc and UGC 455, also an elliptical galaxy with morphological classification E and a D_{25} diameter of 29.9 kpc, making it the second largest galaxy in terms of optical B-band diameter. The galaxy Z 383-71 was not mentioned in this comparison as it remains undetected in H I and has no B-band diameter available in HyperLeda.

In summary, most galaxies detected in H I within the group have H I in excess, with UGC 439 being the most massive H I galaxy and LEDA 90496 being the least massive. However, there are two detections made that are not part of the discussion above.

These are Detection Two, which is closest to UGC 439 and UGC 435, and Detection Three, which is closest to LEDA 90496. Detection Two has what seems to be an optical counterpart in the southeast direction. This is, however difficult to conclusively determine if this optical detection is part of the group without redshift of the detection. Detection Three also has an optical counterpart but no redshift information.

3.5.2 H I Kinematics

To assess kinematics, the global spectra of each galaxy, detected in H I and centred on each galaxy's optical redshift, were compared as shown in Fig. 3.8. The same profiles were also compared without centring on each galaxy's optical redshift, as shown in Fig. 3.9. These global velocity profiles were made using `SoFiA` output products. Fig. 3.10 was also made, showing the first three moments: the H I column density moment-0, velocity moment-1 maps (middle) and velocity dispersion moment-2 maps (right). From Fig. 3.8, there is, on average, a match between each galaxy's optical redshift and H I systemic velocities, as well as a match in the spatial positions of the H I and optical disk as shown in Fig. 3.4. This serves as evidence of minimal interaction with the environment through ram-pressure stripping or any significant past merger events that could offset the two centres.

This velocity match is also reflected in previous observations of UGC 439, which found a redshift of $z = 0.017694 \pm 0.000150$, corresponding to a heliocentric velocity of $v_{\rm H\,I} = 5305 \pm 45$ km s^{-1}, from observations of the nuclear region's optical spectrum that is part of the Six-degree Field Galaxy Survey (Jones et al., 2009), as well as a redshift and heliocentric velocity of $z = 0.017686 \pm 0.000005$ and $v_{\rm H\,I} = 5302 \pm 2$ km s^{-1} using Arecibo H I 21-cm emission. These observations also match well with MeerKAT's observations of $z = 0.017684$ and $v_{\rm H\,I} = 5302$ km s^{-1} as can be seen in Table 3.2, and further shows that the offset in velocity between UGC 439 H I disk and its optical disk is negligible.

As mentioned in subsection 3.5.1 and shown in Table. 3.2, UGC 439 has the largest H I mass and integrated flux. This is also reflected in its global velocity profile shown in Fig. 3.8, where UGC 439 has more H I flux compared to other galaxies in the group. In addition to this, the UGC 439 double-horned global H I profile is asymmetric. This asymmetry is also seen in both the Arecibo and, to a lesser extent, the GMRT profiles as detailed in Dutta et al. (2016) and shown in Fig. 3.11. The asymmetry can be seen in the velocity map of Fig. 3.10 where the southern side of the galaxy, corresponding to the blue-green peak, seems to be more extended than the northern part, corresponding to the red peak. Observations of UV and infrared images of UGC 439 reveal its stellar disk to be asymmetric in terms of its spiral structure and light distribution, reflecting the asymmetry observed in the global H I profile (Dutta et al., 2016). Such an asymmetry could arise from three different environmental mechanisms: ram-pressure stripping, gas accretion, or galactic interaction (e.g. de Blok et al., 2014; Elagali et al., 2019).

Given that UGC 439 is observed to have H I in excess (see Table 3.2), it is unlikely

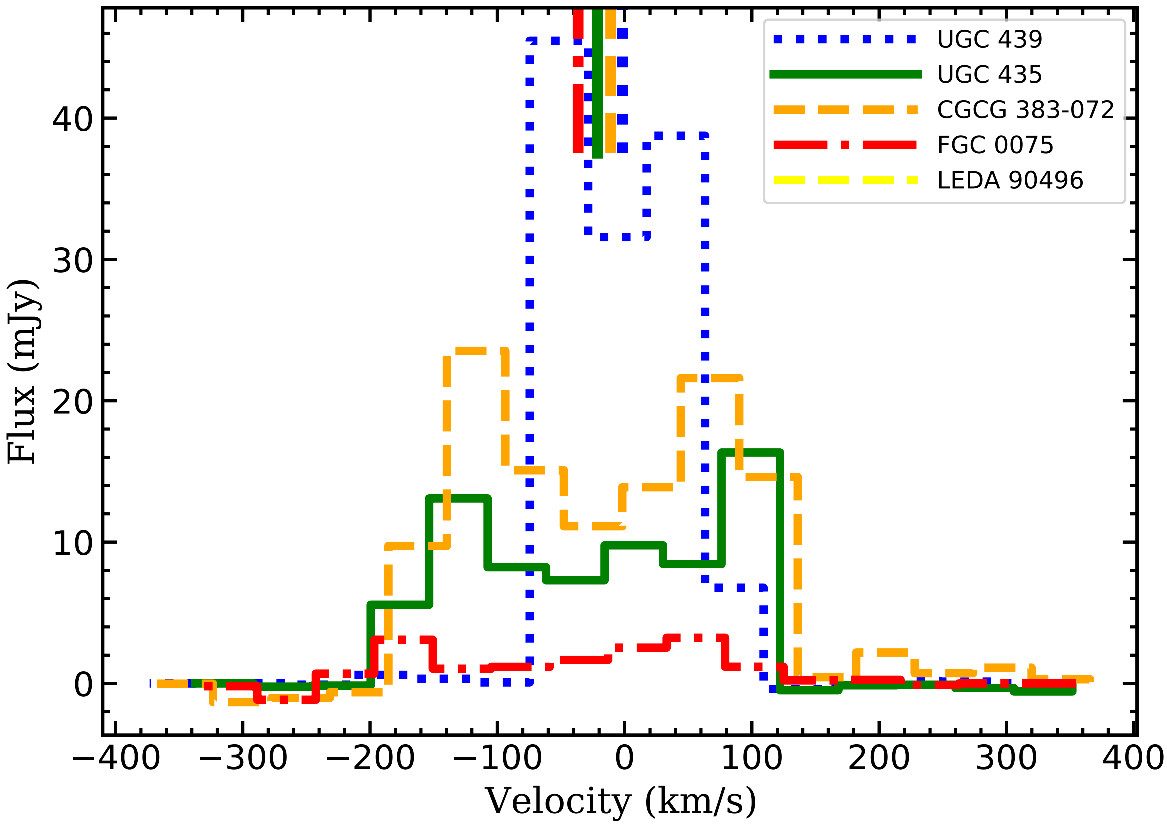

Figure 3.8: Global velocity profiles for UGC 439, UGC 435, CGCG 383-072, FGC 0075, LEDA 90496. The velocities of these galaxies have been shifted with zero corresponding to z_g (shown in Table 3.1) while the vertical lines represent $z_{\rm H\,I}$.

.

that ram-pressure stripping could be playing a significant role leading to this observed asymmetric global H I profile. However, UGC 439 is within a galaxy group. Given the asymmetry observed in both the H I and optical structures, it is possible that the galaxy was involved in a past merger event. Such events are known to affect the structure and kinematics of the extended H I disc (e.g. Hibbard & van Gorkom, 1996; Duc et al., 1997), with a few cases offsetting the H I centres from the optical discs. UGC 439 has a distorted moment 1 velocity profile and a disturbed moment 2 velocity dispersion profile, with peak dispersions (red) occurring at various points in the disk of the galaxy (please see Fig. 3.10), and not uniformly varying from the centre to the edge of the galaxy. However, the H I and optical disc centres seem to coincide in both the spatial and spectral domains. This implies that if a past merger event occurred in UGC 439, it was not significant enough to cause an offset in the two centres.

The presence of high-velocity clouds could either indicate H I accretion or gas removal from galactic disks through tidal interaction, serving as an alternative explanation to the asymmetric H I double-horned profile of UGC 439. High-velocity clouds can be observed by the presence of excess emission in the wings of the global H I profile (Schulman et al., 1994). However, this could also be a consequence of a warped H I

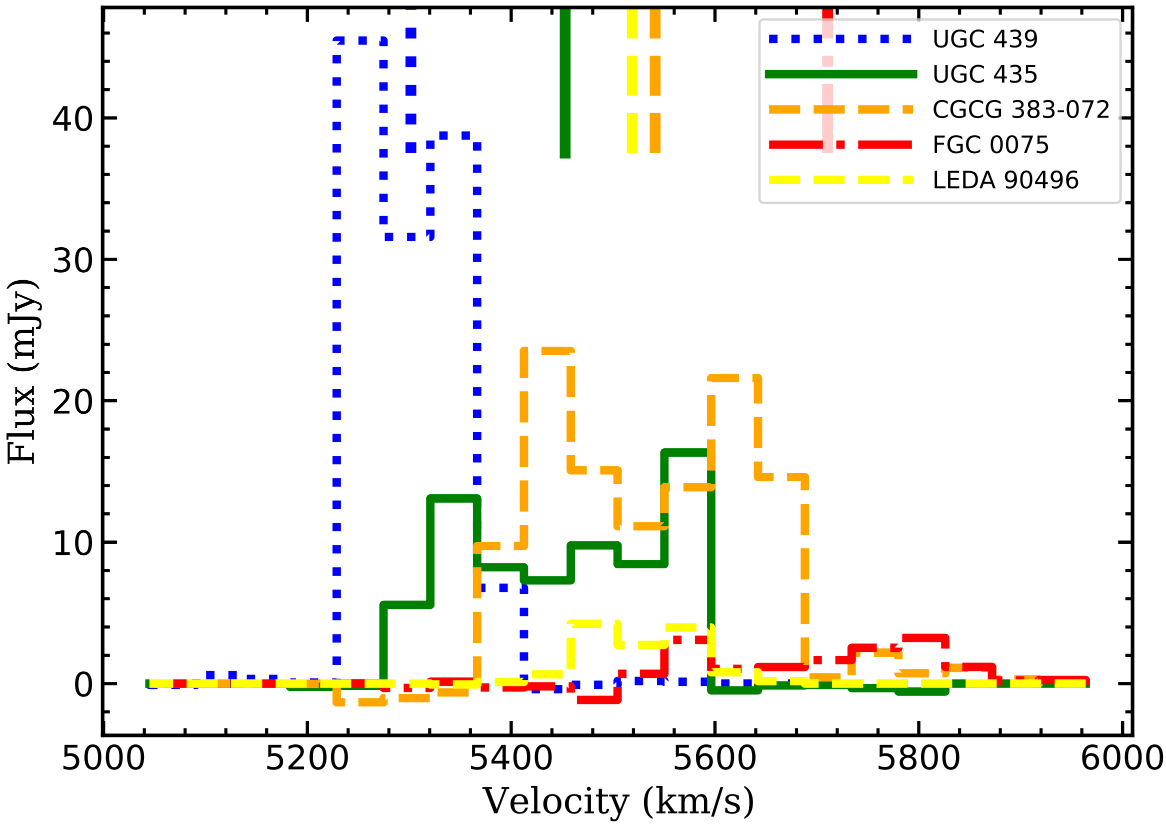

Figure 3.9: Global velocity profiles for UGC 439, UGC 435, CGCG 383-072, FGC 0075, LEDA 90496. The velocities of these galaxies have not been shifted with zero corresponding to z_g, while the vertical lines represent $z_{\mathrm{H\,I}}$

.

disk. Dutta et al. (2016) noted that there was excess emission in the blueshifted wing of the Arecibo global H I profile that could not be explained by a simple rotating disc model but needed deeper H I emission observations to distinguish between the two scenarios. The MeerKAT H I emission is detected over almost the full velocity range of both the Arecibo and GMRT (Fig. 3.11), however, with a lower velocity resolution of 44 km s^{-1}. Consequently, the wings are not well resolved, making it difficult to distinguish between the two scenarios. Higher velocity resolution H I emission observations of UGC 439 would be required to distinguish between these two scenarios and, therefore, provide a better clue into the nature of the excess emission in the blueshifted wing of the Arecibo global H I profile. Note that, as can be seen in Fig. 3.11, uGMRT H I 21-cm emission recovers only $\sim$ 20 per cent of that found in Arecibo spectrum. This is due to the poor sensitivity and uv-coverage of the uGMRT data, which does not allow detecting any diffuse and extended H I gas around UGC 439 (Dutta et al., 2016)

The other two neighbouring galaxies are within 150 kpc of UGC 439, that is, UGC 435 and CGCG 383-072. Dutta et al. (2016) had determined UGC 435's redshift and heliocentric velocities as z = 0.018139 and $v_{\mathrm{H\,I}}$ = 5438 km s^{-1}, which are comparable to MeerKAT's values of z = 0.018189 and $v_{\mathrm{H\,I}}$ = 5453 km s^{-1}. They also determined

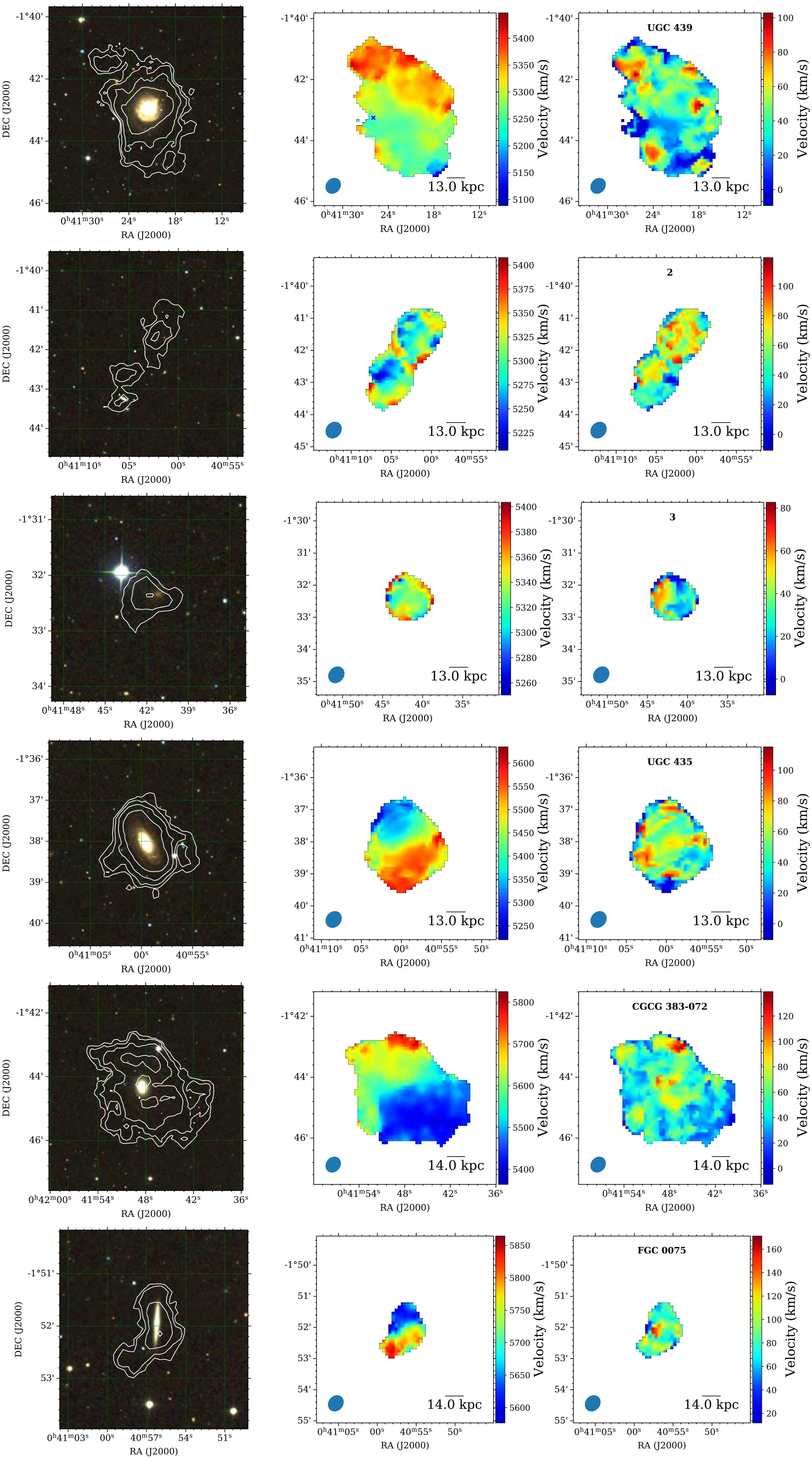
UGC 439
2
3
UGC 435
CGCG 383-072
FGC 0075
13.0 kpc
14.0 kpc
DEC (J2000)
RA (J2000)
Velocity (km/s)

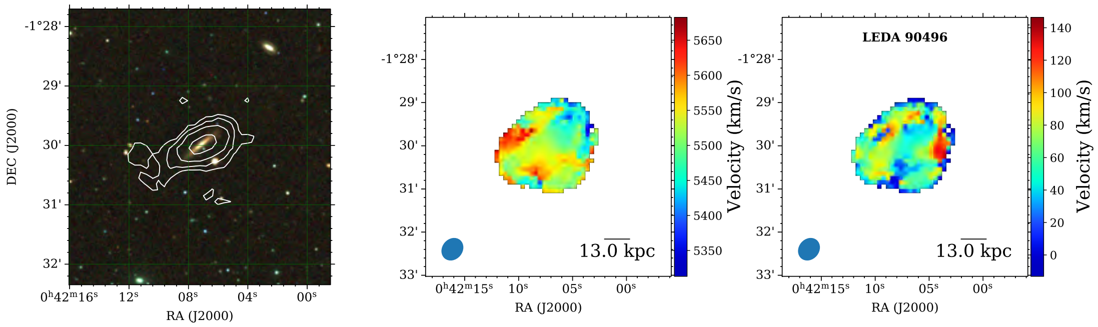

Figure 3.10: Moment maps representing the H I column density (moment-0) contours plotted over RGB cutouts from the optical SDSS image (left), moment-1 maps (middle) and moment-2 maps (right) of 7 detected H I sources, UGC 439, UGC 435, CGCG 383-072, FGC 0075, LEDA 90496 and two other sources with potential optical counterparts but no redshift information available.. The contours in the middle panels correspond to H I column densities of $2^n \times 5 \times 10^{19}$ cm^{-2} ($n = 0, 1, 2, 3, \ldots$). The MeerKat restoring beam of $33.4'' \times 28.2''$, a spatial scale bar of 13 kpc and the position of the quasar next to UGC 439 (blue cross) are also shown in the middle and right panels.

CGCG 383-072 redshift and heliocentric velocities as $z = 0.018356$ and $v_{\mathrm{H\,I}} = 5503$ km s^{-1}, which are also comparable to MeerKAT's values of $z = 0.018484$ and $v_{\mathrm{H\,I}} = 5541$ km s^{-1}. UGC 435 and CGCG 383-072 also have asymmetric global H I profiles as can be seen in both Fig. 3.8 and 3.9, albeit, to a lesser extent. There is more flux in the blue shifted portion of CGCG 383-072 global H I spectrum, seen in Fig. 3.8, which corresponds to the southern blue peak that is more extended than the northern peak, as seen in the velocity map of Fig. 3.10. UGC 435 shows more flux in the red shifted portion of its global H I spectrum, also seen in Fig. 3.8, which also corresponds to the southern red peak that is more extended than the northern blue peak, as seen in the velocity map of Fig. 3.10. The same pattern is reflected in UGC 439, where its global H I spectrum has more flux in its blue shifted portion, seen in Fig. 3.8, which also corresponds to the southern blue-green peak that is more extended than the northern red peak, as seen in the velocity map of Fig. 3.10. The moment 2 maps of UGC 435 and CGCG 383-072, seen in Fig. 3.10, also have red bumps at various points in the H I disk, corresponding to portions with high turbulence. However, they are, on average, centrally dominated. In summary, the three galaxies have more flux and are consequently more extended in their southern peaks than in their northern peaks.

It is also interesting to note that FGC 0075 is the most deficient galaxy of the galaxies detected in H I, with a deficiency parameter of 0.32 from Table. 3.2. FGC 0075 is located south of UGC 439, UGC 435 and CGCG 383-072, the same side of the three galaxies that has more H I flux in comparison. FGC 0075 also appears to have a warped velocity profile, as seen in the velocity map of Fig. 3.10, but shows clear signs of rotation. However, LEDA 90496 is also slightly deficient with a deficiency parameter of 0.20, as seen in Table. 3.2, but is located on the northern side instead. LEDA 90496 has less H I mass compared to FGC 0075, but is further away from UGC 439 with an angular separation of 17.3 arcminutes compared to 11.0 arcminutes separation for FGC 0075

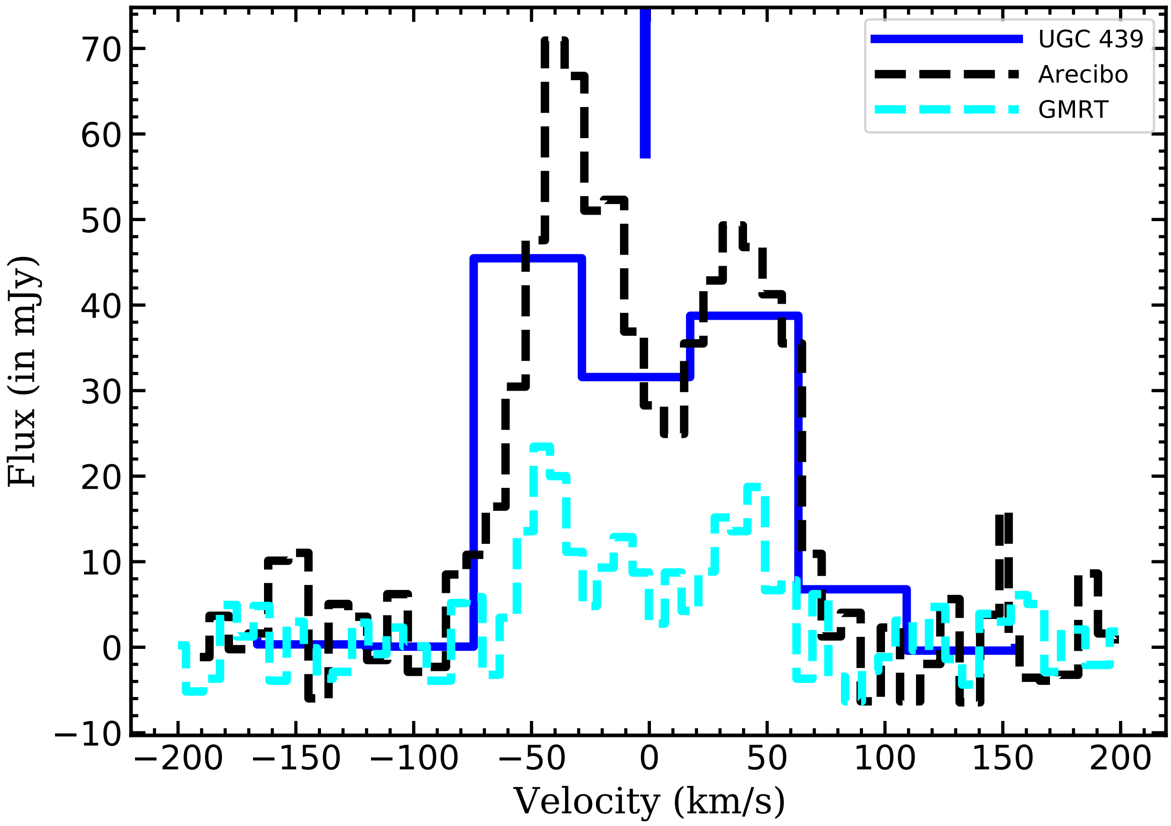

Figure 3.11: Comparison between MeerKAT, Arecibo (Springob et al., 2005) and uGMRT (Dutta et al., 2016) global velocity profiles for UGC 439. The velocities of these galaxies have been shifted with zero corresponding to z_g, while the dashed vertical lines represent $z_{\mathrm{H\,I}}$

.

(please see Table. 3.1).

West of UGC 439 and the south of UGC 435, H I is detected and imaged as seen in Fig. 3.4. It is Detection Two in Fig. 3.10. The SDSS background image in both Fig. 3.4 and 3.10 shows an optical counterpart to the southeast end, associated with this H I source. However, this source appears undetected in all catalogues used for this thesis, including the HyperLeda and NED. Consequently, there was no redshift associated with this optical counterpart that would allow us to conclusively determine if it is part of the current group and, therefore, associated with the H I source or is further away in redshift. It is possible that this is a dwarf galaxy, should it be within the group's redshift. However, based on its geometric appearance of a disk-type galaxy with a given inclination and position angle, we can only speculate that it is much further away than the redshift of the group, and the H I source is an extragalactic H I cloud within the group.

Upon visual inspection of Detection Two in the H I channel map or FITS cube, it is only visible in one channel. This is somewhat mirrored in the global H I profile shown

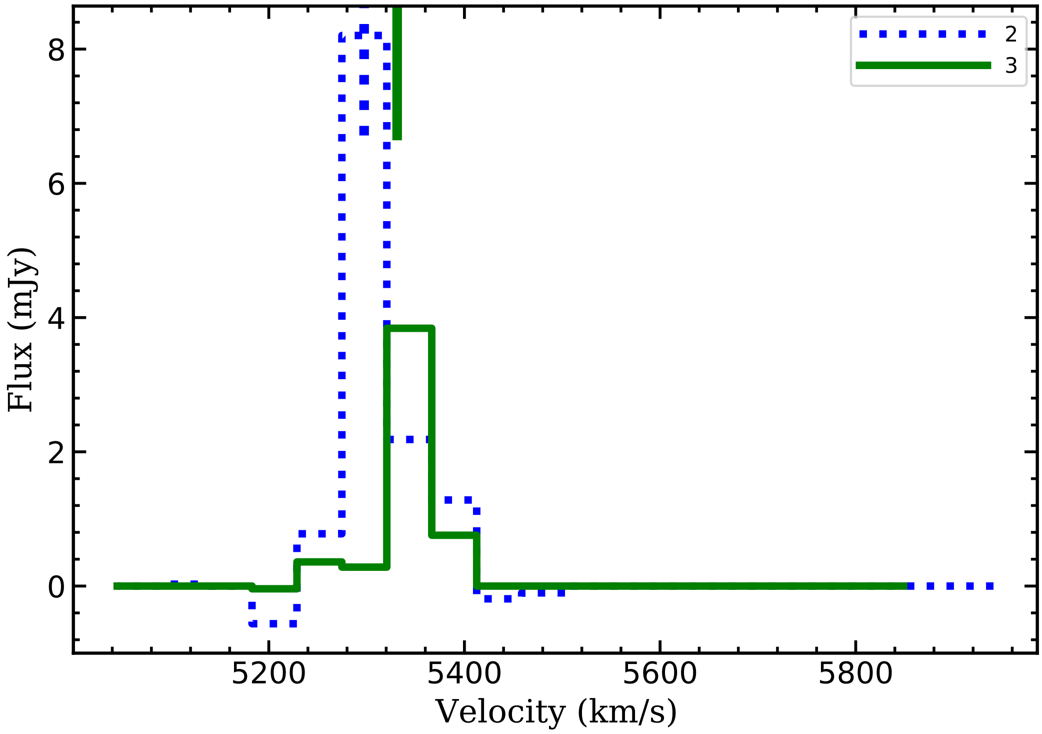

Figure 3.12: Global velocity profiles for the two sources identified in H I with potential optical counterparts but no redshift information available. The velocities of these galaxies have not been shifted with zero corresponding to z_g, while the dashed vertical lines represent $z_{\rm H\,I}$.

.

in Fig. 3.12, as well as the velocity map shown in Fig. 3.10. In both figures, there is an absence of a rotation signature, with Fig. 3.12 not exhibiting the typical double-horn profile and Fig. 3.10 not showing the typical velocity gradient expected for a rotating disk.

Given the absence of a rotation signature in both the global H I profile and the velocity map, one could presume that this H I source is rotating at velocities below our current velocity resolution of 44 $\rm km\,s^{-1}$. However, this is unlikely, as random motions usually dominate at these velocities. Therefore, it is more likely that this source is not rotating as a whole, and no section of this source is rotating. This supports our speculation that the optical detection seen to the southwest of the SDSS image is indeed further away in redshift compared to our H I source, given its disk-like appearance and disk-dominated galaxies usually have a much larger rotation velocity. However, spectroscopic and photometric observations of this optical counterpart are needed to conclusively ascertain this speculation.

When it comes to the H I mass, source two is detected above the 3σ upper limits on H I mass of $5.09 \times 10^8 \rm M_\odot$, with its H I mass being $7.93 \times 10^8 \rm M_\odot$ at the group redshift of $z = 0.01844$. This is a significant amount as it is $\sim 92\%$ the mass of LEDA 90496,

$\sim$ 83% the mass of FGC 0075 but only $\sim$ 10% mass of the most massive galaxy in terms of H I, UGC 439.

There also exists a second H I detection between LEDA 90496 and the three galaxies: CGCG 383-072, UGC 439 and UGC 435. It is Detection Three seen in Fig. 3.10. This H I detection also has a faint optical counterpart in the background SDSS image. Visually, this optical counterpart resembles a dwarf galaxy. However, it is not detected in any catalogues used in this thesis and consequently has no spectroscopic or photometric information associated with it that would make it possible to identify its morphology and position in redshift.

Detection Three is also only visible in one channel of our FITS cube upon visual inspection and also has a global H I profile shown in Fig. 3.12 and velocity map shown in Fig. 3.10 that show no rotation signature. It is, therefore, possible that this source is not rotating, similar to the previous source two. However, assuming that the faint optical counterpart of this source is not discordant and is indeed within the UGC 439 group and its H I and optical disks are aligned such that they are both sufficiently face-on, then there also exists a possibility that the rotation gradient is not detectable at the (relatively low) spectral resolution of 44 $\mathrm{km\,s^{-1}}$. However, we would need to determine the optical counterpart's redshift, as well as make H I higher velocity resolution observations of this detection in order to verify this possibility.

Detection Three has a H I mass of 3.55×10^8 $\mathrm{M_\odot}$ at the group redshift of 0.01844, which is above the 1σ limit of $1.70 \times 10^8 \mathrm{M_\odot}$ but below the 3σ upper limits of $5.09 \times 10^8 \mathrm{M_\odot}$. This makes it only $\sim$ 5% of the H I mass of UGC 439, but $\sim$ 37% of the mass of FGC 0075, $\sim$ 41% of the mass of LEDA 90496, and half the mass of Detection Two.

Regarding uncertainties in the measured $D_{\mathrm{H\,I}}$ values, we estimated uncertainties corresponding to half a beam size to estimate beam smearing effects on our measured $D_{\mathrm{H\,I}}$ values.

Beam smearing can cause the measured H I diameters to appear larger than they truly are, especially in cases where galaxies have a low spatial resolution. In this study, the measured H I sizes may reflect this potential bias, leading to overestimating the measured H I sizes. However, to assess the impact of this possible overestimation, we introduced an uncertainty based on half a beam size into our analysis, as shown in Figs. 3.6 and 3.7 as well as Table. 3.2.

After incorporating this into our error margins, we found that it did not significantly alter the overall trends or conclusions drawn from the data. The uncertainties introduced by beam smearing fall within the scatter in the H I mass-size relationship and follow the general trend observed.

While the decision was made not to apply beam corrections in the current analysis, it is acknowledged that future work could benefit from a more rigorous approach to correcting for this effect. Such corrections would allow for even more precise measurements of

HI sizes. For this study, however, the uncertainties introduced by beam smearing do not significantly impact the primary conclusions, as the overall results remain robust within the given error margins.

3.6 Absorption

Dutta et al. (2016) observed the peak absorption in the sightline of the background quasar towards UGC 439 was at the kinematic minor axis of the H I disc and at the systematic velocity of UGC 439. However, due to GMRT sensitivity constraints, they were not able to observe the H I disc from UGC 439 extending all the way up to the position of the quasar. In contrast to this, as seen in UGC 439 velocity map of Fig. 3.10, we observe the H I disc extending all the way to the sightline of the quasar at the systematic velocity of the galaxy and co-rotating with the H I disc. However, due to the low-velocity resolution nature of the current MeerKAT data, at 44 km s^{-1}, we were unable to proceed with detailed H I absorption line analysis for this group and would recommend higher velocity resolution observations of the group to determine the properties of H I gas at the sightline of the quasar. Combining both studies, it is likely that the absorption system is identical to the gas disk of UGC 439, and no further extraplanar gas is identified.

3.7 Summary

In summary, the UGC 439 group was observed as part of the MALS survey in the commissioning phase of the MeerKAT array. The group has eight members, five of which were detected in H I and shown in Fig. 3.4. Of the five detections, the three central ones, that is, CGCG 383-072, UGC 439 and UGC 435, had the largest H I mass and diameter. Dutta et al. (2016) also detected these three galaxies in H I emission, but did not detect H I emission from the absorbing gas, therefore making the absorbing gas appear separate from UGC 439. In this study, the observed H I disks of all three galaxies are more extended in comparison. UGC 439 and UGC 435 have H I in excess based on the expected H I masses calculated from the B-band luminosity and stellar masses. This is also seen for CGCG 383-072 from its B-band-based deficiency calculation. However, given that CGCG 383-072 is an early-type galaxy, we could not reliably determine its expected H I mass from the stellar mass because of the large variety of H I content in early-type galaxies as discussed in Serra et al. (2012). These galaxies are also systematically more extended towards the south than the north in their H I morphology.

The remaining two galaxies, LEDA 90496 to the north and FGC 0075 to the south, were the smallest galaxies in terms of H I mass and diameter and were also H I deficient based on the expected H I masses calculated from the B-band luminosity, with FGC 0075 to the south being more deficient than LEDA 90496 to the north. When compared to the H I deficiency calculated from the galaxies' stellar mass, FGC 0075 appeared to be deficient while LEDA 90496 has H I in excess. It is possible that the discrepancy between the B-band-based deficiency parameter and the stellar mass-based deficiency parameter is a result of our using the group redshift to calculate the expected H I mass based on the B-band luminosity. The decision was made because we did not have the spectroscopic redshift of LEDA 90496. In addition to the H I detected galaxies were two H I detections, both with unconfirmed optical counterparts and therefore need redshift and photometric information of these counterparts to conclusively determine if they are part of the group. Detection two has its H I mass above the 3σ limit, while detection three had its H I mass below this limit but above the 1σ limit, with detection two being about double the mass of detection three. Both detections did not exhibit signs of rotation that are characteristic of a rotating H I disc and, therefore, could possibly be H I clouds or galaxies at low inclination angles. These two H I detections were not seen in the ALFAFA data (Springob et al., 2005) and, despite detection two being within the field of view of the GMRT data, it was well below their rms value of 2.0 mJy beam^{-1} channel^{-1} (Dutta et al., 2016).

When it comes to the morphology of the H I detected galaxies in the group, all are late-type (spiral) galaxies with the exception of CGCG 383-072, an early-type (elliptical) galaxy located in the central region of the group. In spite of its morphological characteristics, it is the second most massive galaxy in terms of H I mass and has its H I mass distributed on a regularly rotating disc. While it is common for the remaining late-type galaxies to be H I rich, the presence of H I in early-type galaxies is not a universal characteristic, but it is relatively common, as detailed in Serra et al. (2012) who found 1/5 of all early-type galaxies and 1/4 of all early-type galaxies outside the Virgo cluster hosting H I distributed on a regularly rotating disc and at low column densities.

The environment also plays a role in the detection of H I in early-type galaxies as seen in the ALFAFA data, from just a few per cent in the Virgo cluster having H I (di Serego Alighieri et al., 2007) to $\sim$ 40 per cent outside it (Grossi et al., 2009). This suggests that the detection of H I in early-type galaxies is more common in areas where galaxies are less subject to disruptive environmental processes and also suggests that galaxy-galaxy interactions and environmental effects have not set in yet in our group implying that it could be at an intermediate state of preprocessing.

Our observations indicate that the UGC 439 group is in an intermediate state of preprocessing. The inner galaxies are H I rich. Whether this might stem from the accretion or stripping of gas from other galaxies can, given the quality of our observations, only be the subject of speculation.

Chapter 4

Summary

This thesis used data from the MeerKAT Absorption Line Survey (MALS) (Gupta et al., 2017), specifically focusing on the third key science theme titled Galaxy Evolution through H I and OH Emission. The first three main goals of the emission line part of the survey are: (1) to catalogue basic emission line parameters of observed objects, (2) to produce H I emission line maps and data cubes of resolved emission line objects, (3) to parameterize the extended morphology and kinematics, spin characteristics, rotation curves, and surface density profiles of the resolved galaxies independently as well as in connection with the absorption line survey to understand the nature of 21-cm and OH absorbers (Gupta et al., 2017).

Consequently, the thesis focused on studying the interstellar medium of galaxies, specifically the neutral hydrogen (H I) content, distribution, density, and dynamics, through high spatial resolution observations of the Klemola 31 and UGC 439 groups. Therefore, the thesis offers insights into the complex processes affecting galaxy evolution in different environments. To make use of an additional tool, the absorption line characteristics of H I were analysed and compared with the kinematics and the morphology as induced by the observation of the H I emission line in the same systems. In this chapter, a summary of the findings from the two galaxy groups is made.

4.1 Klemola 31

The aim of this work was to identify with high spatial resolution the interstellar medium responsible for the H I absorption in front of the background quasar, PKS2020-370, as part of the MeerKAT Absorption Line Survey (MALS) programme. To this end, the Klemola 31 galaxy group, the group at the foreground of quasar PKS2020-370, was observed using 60 antennas of MeerKAT-64 array and produced a data cube with 1024×1024 pixels of size $2''$ and with 2304 frequency channels each channel having a resolution of 5.7 $\mathrm{km\,s^{-1}}$ and a common restoring beam of $11.9'' \times 7.6''$.

H I emission from Klemola 31 member galaxies reside in the frequency range $1379.4 \sim 1382.2$ MHz, which corresponds to the redshift and recession velocity ranges of $0.0276 \sim$

0.0297 and 8274.3 $\sim$ 8903.8 km s^{-1}. Consequently, only SPW-9, of the 15 spectral windows, was selected for further processing and imaging, as it covered the relevant frequency spectrum of 1351 $\sim$ 1411 MHz needed for this study, which resulted in a data cube with an rms noise of 0.79 mJy $beam^{-1}$ $channel^{-1}$ corresponding to the 3σ H I column density of 3.1×10^{20} cm^{-2}, assuming a linewidth of 15 km s^{-1}.

From this data cube, we were able to detect H I emission associated with four of the six members of Klemola 31 galaxy group while also placing a 3σ upper limit ($< 5 \times 10^{8} M_{\odot}$) on the H I mass of the two undetected galaxies, assuming a linewidth of 200 km s^{-1}. The four galaxies detected in H I were ESO400-11, ESO400-12 (Klemola 31A), ESO400-13 and LEDA 631562, while the two galaxies that remained undetected were companion galaxies Klemola 31B and LEDA 2807038.

We later used the data cube to make surface density, velocity field, and velocity dispersion maps. We extracted the global spectra of the four galaxies detected in H I and compared them to each other by centring their H I spectra on their optically defined redshifts. From this, we observe that ESO400-13 is detected only on the blueshifted side and has the most irregular spectrum and velocity field. In addition to this, Klemola 31A and ESO400-13 show kinematic asymmetries in their emission profile compared to the other two galaxies' profiles.

Of the H I detected galaxies, ESO400-11 has the largest diameter and mass. It shows a disturbed morphology and tidal extensions, possibly attributed to its interaction with the gas-poor, early-type companion galaxy LEDA 2807038. This is followed by Klemola 31A, whose H I disc resembles a warped structure with a large quantity of H I gas trailing the far side of the spiral arm from the galaxy Klemola 31B. The receding tail displays recession velocities, suggesting that the tail is not in the same plane as the galaxy and is instead dragged out by the interaction with Klemola 31B and, therefore, points to the possibility of a recent tidal disruption. The least massive galaxy is ESO 400-13, which has its H I disc displaced from its optical disc. And finally, the last galaxy, LEDA 631562, has the most regular velocity field despite its central H I hole, possibly attributed to a central active galactic nucleus (AGN) present in the galaxy, evidenced by its BPT diagnostic being consistent with ionization through a power-law spectrum (Chilingarian et al., 2017).

The H I content and morphology of these detections show signs of galaxy-galaxy interaction or galaxy-environment interaction. Given that these interactions may lead to galaxies becoming H I deficient, we proceeded to compare our H I detections with the $D_{\rm H\,I}$- $M_{\rm H\,I}$ relation from Wang et al. (2016) and found them compliant with the relation to within 3σ. We later estimated the expected H I masses following the scaling relation by Jones et al. (2018a), based on the B-band luminosity, and compared these estimates to the H I masses derived from the H I detections in the data cube. From this comparison, we observed that all estimated points lie well above the $D_{\rm H\,I}$- $M_{\rm H\,I}$ relation of Wang et al. (2016) and above their observed counterparts. This demands further investigation of gas removal processes in different environments that affect the $D_{\rm H\,I}$ - D_{25} relation but leaves the $D_{\rm H\,I}$- $M_{\rm H\,I}$ relation fairly intact (Stevens et al., 2019).

This serves as clear evidence that all H I detected galaxies are H I deficient and significantly truncated with respect to their optical disks. However, only ESO 400-13 show the most significant H I deficiency of (DEF H I = 0.84). This is unsurprising, given that the same galaxy also shows maximum displacement between the optical and H I disks. The H I gas is totally asymmetric, being pushed to one side of the galaxy only. This is typical of a ram-pressure stripped galaxy, running at high velocity in a hot and tenuous intra-galactic medium (IGM) and has been observed in other galaxies such as NGC 4438 in the Virgo cluster and Arp 105 (Combes et al., 1988) as well as in the Coma cluster (Chen et al., 2020). It is, however, unique in galaxy groups and a possible avenue for further studies.

To estimate what velocity the galaxy must be travelling through the group, we modelled the ram pressure and anchoring self-gravity of ESO400-13 following Gunn & Gott III (1972) and found a relative velocity of ~ 200 km s^{-1} which is totally feasible and compatible with the hypothesis of ram pressure stripping for ESO 400-13.

Turning our focus to Klemola 31A, we found the estimated $D_{\mathrm{H\,I}}$ for Klemola 31A, 38.0 kpc, to be consistent with the value provided by Carilli & van Gorkom (1992) whereas its total line flux of 0.78 Jy km s^{-1}, reported by Boisse et al. (1988), is consistent with our MeerKAT measurement of 0.86 ± 0.08 Jy km s^{-1}.

Klemola 31A reveals a characteristic distortion in its SE extension due to competition between emission and absorption in front of PKS2020-370. At the position of PKS2020-370, we extracted a spectrum from GMRT data, smoothed it by three channels to obtain a spectral resolution comparable to the MeerKAT spectrum ~ 5.7 km s^{-1} and compared it to the MeerKAt spectrum. However, given that MeerKAT is more sensitive, we focused on the more sensitive MeerKAT spectrum.

The MeerKAT spectrum was contaminated by H I emission. Therefore, we corrected for emission using a simplistic single Gaussian component, resulting in a spectrum with an integrated absorption of 0.26 ± 0.03 km s^{-1}, which matches the VLA A-configuration measurement by Carilli & van Gorkom (1987) well within 1σ. This integrated absorption spectrum corresponded to a spin temperature $T_{\mathrm{s}} < 2950$ K, a conservative upper limit since H I emission is integrated over an area of 6.9 kpc $\times$ 4.4 kpc and cannot be compared to absorption if there are inhomogeneities and clumpiness.

To estimate the H I column density, spin temperature and velocity of the H I gas at the position of PKS2020-370 without being affected by beam smearing effects, we created a tilted-ring (TiRiFiC) model of Klemola 31A, using a direct fit to the data cube, at a very high spatial resolution (pixel size of $0.2''$ and half-power beam width of $0.6''$). Assuming the morphology of Klemola 31A is correctly modelled by our tilted-ring model, we estimated a spin temperature of $T_{\mathrm{s}} = 530$ K for a homogeneous regularly rotating disk. However, this estimate did not take kinematics into account and assumed that the absorbing gas was in the plane of the galaxy.

When considering kinematics, we took the peak positions of the absorption spectrum from the data cube and the emission spectrum from the tilted-ring model and compared them. The emission peak has a dispersion of 12.9 $\mathrm{km\,s^{-1}}$ and is offset with respect to the absorption peak by 38.0 $\mathrm{km\,s^{-1}}$, serving as evidence that the observed absorption profile stems from anomalous gas not participating in the assumed regular rotation of the disk.

This anomalous gas was also confirmed by the low Na I / Ca II ratio towards PKS2020-370, reflecting low radiation field as compared to the galactic background radiation (Dutta et al., 2017c). This is typically seen in quasar-galaxy pairs where the line-of-sight does not pass through the gaseous or stellar disk and further cements the evidence that the absorption is produced by gas unrelated to the cold H I disc.

Assuming the anomalous gas comes from Klemola 31A disc, the spin temperature estimate of $T_s = 530$ K may be valid. However, given a maximum rotation velocity of 56 $\mathrm{km\,s^{-1}}$, the velocity offset of 38 $\mathrm{km\,s^{-1}}$ is relatively significant, and it may be difficult to justify the occurrence of such strong streaming motions along the spiral arms. Alternatively, the gas seen in absorption is not from the disc and is, in fact, extra-planar. Should this be the case, the spin temperature would remain unknown as we would not have a good measure of the H I column density in emission. An independent estimate of $N_{\mathrm{H\,I}}$ through ultraviolet spectroscopy would help to derive the harmonic mean temperature along the line of sight towards PKS2020-370 and could be pursued as an extension of this thesis (Keeney et al., 2005, e.g.).

In conclusion, Klemola 31 galaxy group is an example of a group at an early stage of evolution with different morphologies and types of galaxies. Although we find recent gravitational disturbances in most of the individual galaxies, we do not detect any intra-group H I emission in the form of bridges and clumps.

This study of the Klemola 31 group combines an analysis of an H I absorption line study with the analysis of the distribution and the status of H I indicating the potential of this approach to study the physical status and properties of both the intergalactic medium/interstellar medium interface in galaxy groups as well as the origin and nature of absorption lines.

4.2 UGC 439

This galaxy group was observed in the commissioning phase as part of the MeerKAT Absorption Line Survey (MALS), aiming to study the neutral H I content in galaxy groups in both emission and absorption. To this end, UGC 439 galaxy group, the galaxy group at the foreground of the quasar, J0041-0043, was observed using 60 antennas of the MeerKat array, resulting in a data cube with 400 × 400 spatial pixels of size 6″ each and 28 frequency channels, each channel having a resolution of ∼ 44 $\mathrm{km\,s^{-1}}$ and a common restoring beam of 33.5″ × 28.3″ .

H I emission was detected in five out of the eight members of UGC 439 group, with two additional H I detections. Of the two detections, one has an optical counterpart, albeit no redshift information that could be used to determine if it is within the group was available, while the other detection does not have an optical counterpart. All H I detections reside in the frequency range 1392.0 – 1397.2 MHz, corresponding to a recession velocity ranges of $v_0 = cz_{\mathrm{H\,I}} \sim 4981 - 6125$ km s^{-1} , and are UGC 439, CGCG 383-072, UGC 435, FGC 0075 and LEDA 90496 in order of their H I masses, as well as the two unnamed H I detections. For galaxies undetected in H I, 3σ upper limits on H I masses ($5.09 \times 10^8 \mathrm{M}_\odot$) were estimated assuming a linewidth of 200 km s^{-1}. These galaxies include UGC 455, Z 383-71 and NGC 227.

Specifically, UGC 439 has the highest H I mass and integrated flux, the second largest H I diameter, with the H I disk extending all the way up to the sightline of the background quasar, and the fourth largest galaxy in terms of B-band D_{25} diameter. Following UGC 439 in H I mass and integrated flux is CGCG 383-072 with the largest measured H I diameter and second largest B-band D_{25} diameter. This makes UGC 435 third in terms of H I mass and integrated flux. Coincidentally, it is also the third-largest galaxy in terms of H I diameter but the fifth-largest galaxy in terms of B-band optical diameter, only slightly smaller than UGC 439. FGC 0075 comes in fourth in H I mass and integrated flux, but among the least in terms of the H I diameters measured, being only larger than LEDA 90496, and third largest galaxy in terms of B-band optical diameter. Finally, LEDA 90496 has the least H I mass and integrated flux, the least H I and optical diameters.

The remaining galaxies not detected in H I are NGC 227, an elliptical galaxy with the largest B-band diameter; UGC 455, also an elliptical galaxy with the second largest galaxy in terms of optical B-band diameter; While Z 383-71 was not mentioned in this comparison as it remains undetected in H I and has no B-band diameter available in HyperLeda.

To assess kinematics, the global spectra of each galaxy detected in H I were compared with and without centering on each galaxy's optical redshift. From this comparison, there was, on average, a match between each galaxy's optical redshift and H I systemic velocities, as well as a match in the spatial positions of the H I and optical disks. Therefore, should a previous merger event or interaction with the environment have occurred, it was not significant enough to offset the two centres.

UGC 439, UGC 435 and CGCG 383-072, the three most massive galaxies in the group in terms of H I mass, had asymmetric double-horned, global H I profiles, albeit to varying extents depending on the individual galaxy. This asymmetry is reflected in their velocity maps, where their southern sides seem to be more extended than their northern sides. The same three galaxies were observed to have H I in excess, with their deficiency parameter being -0.8, -0.25 and -0.56.

The remaining two galaxies detected in H I: LEDA 90496 and FGC 0075, are located in the north and south of the group, respectively, and are the two galaxies that are deficient in H I. LEDA 90496 to the north is slightly deficient with a deficiency parameter of 0.20, while FGC 0075 to the south, the same side of the three galaxies that have more H I flux in comparison, is the most deficient galaxy with a deficiency parameter of 0.32. FGC 0075 also appears to have a warped velocity profile.

West of UGC 439 and south of UGC 435, there is a H I detection, which has an optical counterpart seen in the SDSS background image towards the southeast end but no redshift information that would allow us to conclusively determine if it is part of the current group is available. This detection shows no signs of differential rotation in both its velocity map and global H I profile, making it possible that this could either be a dwarf galaxy or H I cloud. There also exists a second H I detection with an optical counterpart but also no redshift information. It is situated between LEDA 90496 to the north, and the three galaxies: CGCG 383-072, UGC 439 and UGC 435. This H I detection has no differential rotation, making it a possible second H I cloud.

In the case of this group, we confirmed the presence of an extended H I disk at the position of the absorption line system but could not add further information due to the poor velocity resolution of the observations. It is likely that the absorption system is identical to the gas disk of UGC 439, and no further extraplanar gas is identified.

4.3 Comparison and Future Work

In summary, this thesis details observations of two galaxy groups using the MeerKAT array and as part of MALS, Klemola 31 and UGC 439. Klemola 31 is a compact group, and UGC 439 is a loose group.

Klemola 31 galaxy group is mostly deficient in H I with all estimated points lying well above the $D_{\rm H\,I}$- $M_{\rm H\,I}$ relation of Wang et al. (2016) and above their observed counterparts. This demands further investigation of gas removal processes in different environments that affect the $D_{\rm H\,I}$ - D_{25} relation but leaves the $D_{\rm H\,I}$- $M_{\rm H\,I}$ relation fairly intact (Stevens et al., 2019).

Klemola 31 galaxy group also has evidence of tidal interactions between individual galaxies and their satellites, as well as possible ram-pressure stripping seen in ESO400-13, where its H I disk is totally asymmetric, being pushed to one side of the galaxy only. This is typical of a ram-pressure stripped galaxy, running at high velocity in a hot and tenuous intra-galactic gas (IGM) and has been observed in other galaxies such as NGC 4438 in the Virgo cluster and Arp 105 (Combes et al., 1988) as well as in the Coma cluster (Chen et al., 2020). It is, however, unique in galaxy groups and a possible avenue for further studies.

When it comes to Klemola 31A, a spin temperature estimate of $T_{\rm s}$ = 530 K, along the line of sight towards PKS2020-370, was found using the tilted-ring model. However, the emission peak from the tilted-ring model was offset in velocity from the absorption peak by 38 km s^{-1}, which is relatively significant given a maximum disk rotation velocity of 56 km s^{-1}, making it difficult to justify the occurrence of such strong streaming motions along the spiral arms. Alternatively, the gas seen in absorption is not from the disc and is, in fact, extraplanar. Should this be the case, the spin temperature would remain unknown as we would not have a good measure of the H I column density in emission. Consequently, an independent estimate of $N_{\rm H\,I}$ through ultraviolet spectroscopy would help to derive the harmonic mean temperature along the line of sight towards PKS2020-370 and could be pursued as an extension of this thesis (e.g. Keeney et al., 2005).

On turning our attention to UGC 439 galaxy group, our 4K observations at the velocity resolution of $\sim$ 44 km s^{-1} hindered our analysis of H I absorption in the line of sight of towards J0041-0143. This is because 44 km s^{-1} velocity resolution is much lower than the fitted FWHM value of 8 ± 1 km s^{-1} found by Dutta et al. (2016). Therefore, for a detailed analysis of H I absorption, 32K observations at a much higher velocity resolution of $\sim$ 5 km s^{-1} are needed.

When it comes to H I emission, UGC 439 galaxy group is mostly in H I excess. Specifically, the central three galaxies have H I in excess, while the peripheral galaxies are deficient in H I. The UGC 439 group also has two H I detections, each with an optical counterpart that could possibly have discordant redshift. None of these extra H I detections show differential rotation and could possibly be intragroup H I. Therefore, more sensitive H I observations are needed to understand the dynamics and evolution of galaxies in this group.

Due to the differing nature of the two groups, it is, at this stage, difficult to draw statistical conclusions from our work on the general processes dominating gas removal and accretion in galaxy groups in general. Our findings are generally in line with the picture of galaxy groups as a place where H I is being preprocessed and subject to a set of interactions, subsequently leading to the loss of gas. Both galaxy groups show severe sights of interaction between the galaxies. With the UGC 439 group being the looser group, galaxy interaction is affecting the H I distribution of the gas, while the H I content of some galaxies is even increased. Extragalactic gas clouds are detected, which might be the result of tidal or gas removal from galaxies by winds and might be accreted or reaccreted by other galaxies. As galaxies become more concentrated and more evolved, the gas removal processes have acted on them for a longer time, such that they are mostly devoid of H I. The Klemola 31 group seems to be an example of a more evolved galaxy group in comparison, in which the kinematics of some member galaxies are also disturbed as a signature of past interaction. No extragalactic gas clouds at greater distances from galaxies are found, while detecting anomalous gas in emission still indicates that gas is still processed, entering an extragalactic phase or being accreted.

Due to the low frequency of strong background sources and the current insufficient sensitivity of radio telescopes that can be reached in statistical surveys targeting many background targets, we can only find a few H I absorption lines per targeted field that can be studied in combination with the H I emission line properties. In fact, it is a lucky coincidence if, in these observations, H I can be observed along more than one sightline. This is also the case for our observations. Accordingly, we get two coincidental snapshots of the H I line systems in galaxy groups. In the Klemola 31 group, H I associated with the absorption feature shows anomalous kinematics and might, therefore, not be associated with a disk. In UGC 439, the presence of gas not associated with a rotating galaxy, and hence presumably extragalactic, has been observed in emission since we detect extragalactic clouds. It should be highlighted that hence the study of gas in absorption adds important information about the status of the Klemola 31 group. In combination, we can conclude that anomalous gas is present in both systems, and extragalactic clouds are potentially detectable in both systems.

We can hence conclude that the combination of H I absorption line studies and observations of H I in emission will bear important insights into the nature of both the evolution of gas around galaxies and groups or clusters of galaxies as well as the origin and physics of H I absorption line systems.

MALS has observed several associations of strong background sources and galaxy groups or galaxies, offering the chance to follow up our studies on a larger number of systems in preparation for more sensitive surveys with the Square Kilometre Array, opening the full path to the combination of studies of the neutral gas in and around galaxies combining H I absorption and emission lines.

Bibliography

Aditya J. N. H. S., Kanekar N., 2018, A Giant Metrewave Radio Telescope search for associated H I 21 cm absorption in GHz-peaked-spectrum sources, Monthly Notices of the Royal Astronomical Society, 473, 59

Allison J. R., et al., 2015, Discovery of H I gas in a young radio galaxy at z = 0.44 using the Australian Square Kilometre Array Pathfinder, Monthly Notices of the Royal Astronomical Society, 453, 1249

Allison J. R., et al., 2022, The First Large Absorption Survey in H I (FLASH): I. Science goals and survey design, Publications of the Astronomical Society of Australia, 39, e010

Andrews B. H., Martini P., 2013, The Mass-Metallicity Relation with the Direct Method on Stacked Spectra of SDSS Galaxies, The Astrophysical Journal, 765, 140

Arabsalmani M., Roychowdhury S., Zwaan M. A., Kanekar N., Micha\lowski M. J., 2015, First measurement of H I 21 cm emission from a GRB host galaxy indicates a post-merger system, Monthly Notices of the Royal Astronomical Society, 454, L51

Aragon-Calvo M. A., Szalay A. S., 2013, The hierarchical structure and dynamics of voids, Monthly Notices of the Royal Astronomical Society, 428, 3409

Audit E., Hennebelle P., 2005, Thermal condensation in a turbulent atomic hydrogen flow, Astronomy and Astrophysics, 433, 1

Bacchini C., Fraternali F., Iorio G., Pezzulli G., 2019, Volumetric star formation laws of disc galaxies, Astronomy & Astrophysics, 622, A64

Balashev S. A., Noterdaeme P., 2018, Constraining the H_2 column density distribution at $z \sim 3$ from composite DLA spectra, Monthly Notices of the Royal Astronomical Society, 478, L7

Balogh M. L., Navarro J. F., Morris S. L., 2000, The origin of star formation gradients in rich galaxy clusters, The Astrophysical Journal, 540, 113

Banerjee A., Jog C. J., 2008, The Flattened Dark Matter Halo of M31 as Deduced from the Observed H I Scale Heights, The Astrophysical Journal, 685, 254

Banerjee A., Matthews L. D., Jog C. J., 2010, Dark matter dominance at all radii in the superthin galaxy UGC 7321, New Astronomy, 15, 89

Barnes J. E., 1989, Evolution of compact groups and the formation of elliptical galaxies, Nature, 338, 123

Barnes D. G., et al., 2001, The h i parkes all sky survey: southern observations, calibration and robust imaging, Monthly Notices of the Royal Astronomical Society, 322, 486

Begeman K. K. G., 1987, PhD thesis, University of Groningen, Netherlands

Begum A., Chengalur J. N., Karachentsev I. D., Sharina M. E., 2008a, Baryonic Tully-Fisher relation for extremely low mass Galaxies, Monthly Notices of the Royal Astronomical Society, 386, 138

Begum A., Chengalur J. N., Karachentsev I. D., Sharina M. E., Kaisin S. S., 2008b, FIGGS: Faint Irregular Galaxies GMRT Survey - overview, observations and first results, Monthly Notices of the Royal Astronomical Society, 386, 1667

Bell E. F., 2003, Estimating Star Formation Rates from Infrared and Radio Luminosities: The Origin of the Radio-Infrared Correlation, The Astrophysical Journal, 586, 794

Bell E. F., de Jong R. S., 2001, Stellar mass-to-light ratios and the Tully-Fisher relation, Astrophysical Journal, 550, 212

Bell E. F., McIntosh D. H., Katz N., Weinberg M. D., 2003, A first estimate of the baryonic mass function of galaxies, The Astrophysical Journal, 585, L117

Belsole E., Sauvageot J.-L., Ponman T., Bourdin H., 2003, The detection of diffuse emission in hcg 16 with xmm-newton, Astronomy & Astrophysics, 398, 1

Ben-Kiki O., Evans C., Ingerson B., 2009, Yaml ain't markup language (yaml™) version 1.1, Working Draft 2008, 5, 11

Bergeron J., 1986, The MG II absorption system in the QSO PKS 2128-12 : A galaxy disc/halo with a radius of 65 kpc., Astronomy and Astrophysics, 155, L8

Beygu B., Kreckel K., van de Weygaert R., van der Hulst J. M., van Gorkom J. H., 2013, An Interacting Galaxy System along a Filament in a Void, The Astronomical Journal, 145, 120

Biggs A. D., Zwaan M. A., Hatziminaoglou E., Péroux C., Liske J., 2016, Parsec-scale H I absorption structure in a low-redshift galaxy seen against a compact symmetric object, Monthly Notices of the Royal Astronomical Society, 462, 2819

Bigiel F., Leroy A., Walter F., Brinks E., De Blok W. J., Madore B., Thornley M. D., 2008, The star formation law in nearby galaxies on SUB-KPC scales, The Astronomical Journal, 136, 2846

Bigiel F., Leroy A., Walter F., Blitz L., Brinks E., de Blok W. J. G., Madore B., 2010, Extremely Inefficient Star Formation in the Outer Disks of Nearby Galaxies, The Astronomical Journal, 140, 1194

Binney J., 1978, On the rotation of elliptical galaxies., Monthly Notices of the Royal Astronomical Society, 183, 501

Blitz L., Rosolowsky E., 2004, The Role of Pressure in Giant Molecular Cloud Formation, The Astrophysical Journal, 612, L29

Blyth S. L., et al., 2016, Laduma: looking at the distant universe with the meerkat array, Proceedings of Science

Boisse P., Dickey JM., Kazes I., Bergeron J., 1988, A 21 CM study of some QSO/galaxy pairs., Astronomy and Astrophysics, 191, 193

Boissier S., et al., 2007, Radial Variation of Attenuation and Star Formation in the Largest Late-Type Disks Observed with GALEX, The Astrophysical Journal, 173, 524

Bok J., Skelton R. E., Cluver M. E., Jarrett T. H., Jones M. G., Verdes-Montenegro L., 2020, H i study of isolated and paired galaxies: the mir sfr-m sequence, Monthly Notices of the Royal Astronomical Society, 499, 3193

Boksenberg A., Danziger I., Fosbury R., Goss W., 1980, Ca ii absorption lines in the spectrum of the quasar pks 2020-370 due to galactic material in the group klemola 31, Astrophysical Journal, Part 2-Letters to the Editor, vol. 242, Dec. 15, 1980, p. L145-L148., 242, L145

Borthakur S., 2016, Distribution of Cold ($\lesssim$ 300 K) Atomic Gas in Galaxies: Results from the GBT H I Absorption Survey Probing the Inner Halos ($\rho < 20$ kpc) of Low-z Galaxies, The Astrophysical Journal, 829, 128

Borthakur S., Yun M. S., Verdes-Montenegro L., 2010, Detection of diffuse neutral intragroup medium in hickson compact groups, The Astrophysical Journal, 710, 385

Bosma A., 1978a, PhD thesis, University of Groningen, Netherlands

Bosma A., 1978b, The distribution and kinematics of neutral hydrogen in spiral galaxies of various morphological types

Bouché N., et al., 2010, The Impact of Cold Gas Accretion Above a Mass Floor on Galaxy Scaling Relations, The Astrophysical Journal, 718, 1001

Bouwens R. J., et al., 2014, A Census of Star-forming Galaxies in the Z $\sim 9-10$ Universe based on HST+Spitzer Observations over 19 Clash Clusters: Three Candidate Z $\sim 9-10$ Galaxies and Improved Constraints on the Star Formation Rate Density at Z ~ 9.2, The Astrophysical Journal, 795, 126

Broeils A. H., Rhee M. H., 1997, Short 21-cm WSRT observations of spiral and irregular galaxies. HI properties., Astronomy and Astrophysics, 324, 877

Brook C. B., Santos-Santos I., Stinson G., 2016, The different baryonic Tully-Fisher relations at low masses, Monthly Notices of the Royal Astronomical Society, 459, 638

Burbidge E. M., Burbidge G., 1959, Some interconnected multiple extragalactic nebulae., Astrophysical Journal, vol. 130, p. 23, 130, 23

Burbidge E. M., Burbidge G., 1961, A further investigation of stephan's quintet., Astrophysical Journal, vol. 134, p. 244, 134, 244

Byrd G., Valtonen M., 1990, Tidal Generation of Active Spirals and S0 Galaxies by Rich Clusters, The Astrophysical Journal, 350, 89

Cannon J. M., et al., 2011, The Survey of H I in Extremely Low-mass Dwarfs (SHIELD), The Astrophysical Journal, 739, L22

Carilli C., Van Gorkom J., 1987, Discovery of low-redshift, neutral hydrogen absorption in the radio spectrum of pks 2020-370, Astrophysical Journal, Part 1 (ISSN 0004-637X), vol. 319, Aug. 15, 1987, p. 683-686., 319, 683

Carilli C. L., van Gorkom J. H., 1987, Discovery of low-redshift, neutral hydrogen absorption in the radio spectrum of PKS 2020-370, The Astrophysical Journal, 319, 683

Carilli C. L., van Gorkom J. H., 1992, H i Imaging of Four Quasar-Galaxy Pairs: The Parent Galaxies of Low-Redshift Quasar Absorption Systems, The Astrophysical Journal, 399, 373

Carilli C. L., Lane W., de Bruyn A. G., Braun R., Miley G. K., 1996, Redshift H I 21 CM Line Observations of Damped Ly alpha Absorption Systems, The Astronomical Journal, 111, 1830

Catinella B., Haynes M. P., Giovanelli R., Gardner J. P., Connolly A. J., 2008, A Pilot Survey of H I in Field Galaxies at Redshift $z \sim 0.2$, The Astrophysical Journal, 685, L13

Catinella B., et al., 2010, The GALEX Arecibo SDSS Survey - I. Gas fraction scaling relations of massive galaxies and first data release: The GALEX Arecibo SDSS Survey - I, Monthly Notices of the Royal Astronomical Society, 403, 683

Catinella B., et al., 2013, The GALEX Arecibo SDSS Survey - VIII. Final data release. The effect of group environment on the gas content of massive galaxies, Monthly Notices of the Royal Astronomical Society, 436, 34

Cayatte V., van Gorkom J. H., Balkowski C., Kotanyi C., 1990, VLA Observations of Neutral Hydrogen in Virgo Cluster Galaxies. I. The Atlas, The Astronomical Journal, 100, 604

Chen H.-W., Helsby J. E., Gauthier J.-R., Shectman S. A., Thompson I. B., Tinker J. L., 2010, An Empirical Characterization of Extended Cool Gas Around Galaxies Using Mg II Absorption Features, The Astrophysical Journal, 714, 1521

Chen H., et al., 2020, The ram pressure stripped radio tails of galaxies in the Coma cluster, Monthly Notices of the Royal Astronomical Society, 496, 4654

Chengalur J. N., Kanekar N., 2000, Implications of 21-cm observations for damped Ly α systems, Monthly Notices of the Royal Astronomical Society, 318, 303

Chengalur J. N., Kanekar N., 2003, Constraining the Variation of Fundamental Constants using 18cm OH Lines, Physical review letters, 91, 241302

Chengalur J. N., Pustilnik S. A., 2013, Discovery of an extremely gas rich dwarf triplet near the centre of the Lynx-Cancer void, Monthly Notices of the Royal Astronomical Society, 428, 1579

Chengalur J. N., Ghosh T., Salter C. J., Kanekar N., Momjian E., Keeney B. A., Stocke J. T., 2015, H I 21cm emission from the subdamped Lyman- α absorber at $z = 0.0063$ towards PG 1216+069, Monthly Notices of the Royal Astronomical Society, 453, 3135

Chengalur J. N., Pustilnik S. A., Egorova E. S., 2017, UGC 3672: An unusual merging triplet of gas-rich galaxies in the Lynx-Cancer void, Monthly Notices of the Royal Astronomical Society, 465, 2342

Cherinka B., Schulte-Ladbeck R. E., 2011, Ca ii and na i quasar absorption-line systems in an emission-selected sample of sdss dr7 galaxy/quasar projections. i. sample selection, The Astronomical Journal, 142, 122

Chilingarian I. V., Zolotukhin I. Y., Katkov I. Y., Melchior A.-L., Rubtsov E. V., Grishin K. A., 2017, RCSED—A Value-added Reference Catalog of Spectral Energy Distributions of 800,299 Galaxies in 11 Ultraviolet, Optical, and Near-infrared Bands: Morphologies, Colors, Ionized Gas, and Stellar Population Properties$_*$, The Astrophysical Journal Supplement Series, 228, 14

Chung A., Van Gorkom J., Kenney J., Crowl H., Vollmer B., 2009, VLA imaging of Virgo spirals in atomic gas (VIVA). I. the atlas and the H I properties, Astronomical Journal, 138, 1741

Churchill C. W., Mellon R. R., Charlton J. C., Jannuzi B. T., Kirhakos S., Steidel C. C., Schneider D. P., 2000, Low- and High-Ionization Absorption Properties of Mg II Absorption-selected Galaxies at Intermediate Redshifts. II. Taxonomy, Kinematics, and Galaxies, The Astrophysical Journal, 543, 577

Cluver M. E., et al., 2014, Galaxy and mass assembly (gama): mid-infrared properties and empirical relations from wise, The Astrophysical Journal, 782, 90

Combes F., Dupraz C., Casoli F., Pagani L., 1988, CO emission in NGC 4438 : A case for tidal stripping ?, Astronomy and Astrophysics, 203, L9

Cresci G., Mannucci F., Curti M., 2019, Fundamental metallicity relation in CALIFA, SDSS-IV MaNGA, and high-z galaxies, Astronomy and Astrophysics, 627, A42

Crighton N. H., et al., 2015, The neutral hydrogen cosmological mass density at $z = 5$, Monthly Notices of the Royal Astronomical Society, 452, 217

Curran S. J., Tzanavaris P., Darling J. K., Whiting M. T., Webb J. K., Bignell C., Athreya R., Murphy M. T., 2010, New searches for HI 21 cm in damped Lyman α absorption systems, Monthly Notices of the Royal Astronomical Society, 402, 758

Curti M., Mannucci F., Cresci G., Maiolino R., 2020, The mass-metallicity and the fundamental metallicity relation revisited on a fully T_e-based abundance scale for galaxies, Monthly Notices of the Royal Astronomical Society, 491, 944

Daddi E., et al., 2007, Multiwavelength Study of Massive Galaxies at $z \sim 2$. I. Star Formation and Galaxy Growth, The Astrophysical Journal, 670, 156

Dalcanton J. J., Spergel D. N., Summers F. J., 1997, The Formation of Disk Galaxies, The Astrophysical Journal, 482, 659

Darling J., 2012, Toward a Direct Measurement of the Cosmic Acceleration, The Astrophysical Journal, 761, L26

Davé R., Finlator K., Oppenheimer B. D., 2011, Galaxy evolution in cosmological simulations with outflows - II. Metallicities and gas fractions, Monthly Notices of the Royal Astronomical Society, 416, 1354

Davé R., Finlator K., Oppenheimer B. D., 2012, An analytic model for the evolution of the stellar, gas and metal content of galaxies, Monthly Notices of the Royal Astronomical Society, 421, 98

Dekel A., et al., 2009, Cold streams in early massive hot haloes as the main mode of galaxy formation, Nature, 457, 451

Desjardins T. D., et al., 2013, Intragroup and galaxy-linked diffuse x-ray emission in hickson compact groups, The Astrophysical Journal, 763, 121

Di Teodoro E. M., Fraternali F., 2015, $^{3D\$}$ BAROLO: A new 3D algorithm to derive rotation curves of galaxies, Monthly Notices of the Royal Astronomical Society, 451, 3021

Dressler A., et al., 1997, Evolution since z= 0.5 of the morphology-density relation for clusters of galaxies, The Astrophysical Journal, 490, 577

Duc P. A., Brinks E., Wink J., Mirabel F., 1997, Gas segregation in the interacting system Arp 105

Dutta S., Khandai N., 2021, The distribution of neutral hydrogen in the colour-magnitude plane of galaxies, Monthly Notices of the Royal Astronomical Society, 500, L37

Dutta R., Gupta N., Srianand R., O'Meara J. M., 2016, Mapping kiloparsec-scale structures in the extended H I disc of the galaxy UGC 000439 by H I 21-cm absorption, Monthly Notices of the Royal Astronomical Society, 456, 4209

Dutta R., Srianand R., Gupta N., Momjian E., Noterdaeme P., Petitjean P., Rahmani H., 2017a, H I 21-cm absorption survey of quasar-galaxy pairs: Distribution of cold gas around z < 0.4 galaxies, Monthly Notices of the Royal Astronomical Society, 465, 588

Dutta R., Srianand R., Gupta N., Joshi R., Petitjean P., Noterdaeme P., Ge J., Krogager J. K., 2017b, Incidence of H I 21-cm absorption in strong Fe II systems at 0.5 < z < 1.5, Monthly Notices of the Royal Astronomical Society, 465, 4249

Dutta R., Srianand R., Gupta N., Joshi R., 2017c, H I 21-cm absorption from $z \sim 0.35$ strong Mg II absorbers, Monthly Notices of the Royal Astronomical Society, 468, 1029

Dutta R., Raghunathan S., Gupta N., Joshi R., 2020, uGMRT search for cold gas at $z \sim 1-1.4$ towards red quasars, Monthly Notices of the Royal Astronomical Society, 491, 838

Dutta R., et al., 2021, Metal-enriched halo gas across galaxy overdensities over the last 10 billion years, Monthly Notices of the Royal Astronomical Society, 508, 4573

Dutton A. A., van den Bosch F. C., Dekel A., 2010, On the origin of the galaxy star-formation-rate sequence: Evolution and scatter, Monthly Notices of the Royal Astronomical Society, 405, 1690

D'Abrusco R., et al., 2019, Two new catalogs of blazar candidates in the wise infrared sky, The Astrophysical Journal Supplement Series, 242, 4

Elagali A., et al., 2019, WALLABY early science - III. An H I study of the spiral galaxy NGC 1566, Monthly Notices of the Royal Astronomical Society, 487, 2797

Ellison S. L., Patton D. R., Simard L., McConnachie A. W., 2008, Clues to the Origin of the Mass-Metallicity Relation: Dependence on Star Formation Rate and Galaxy Size, The Astrophysical Journal, 672, L107

Elmegreen B. G., Hunter D. A., 2015, A Star Formation Law for Dwarf Irregular Galaxies, The Astrophysical Journal, 805, 145

Elmegreen D. M., Sundin M., Elmegreen B. G., Sundelius B., 1990, Properties and Simulations of Interacting Spiral Galaxies with Transient "Ocular" Shapes.

Erb D. K., Shapley A. E., Pettini M., Steidel C. C., Reddy N. A., Adelberger K. L., 2006, The Mass-Metallicity Relation at z $\gtrsim$ 2, The Astrophysical Journal, 644, 813

Franx M., van Gorkom J. H., de Zeeuw T., 1994, Evidence for Axisymmetric Halos: The Case of IC 2006, The Astrophysical Journal, 436, 642

Freedman W. L., et al., 2001, Final Results from the Hubble Space Telescope Key Project to Measure the Hubble Constant, The Astrophysical Journal, 553, 47

Freeland E., Cardoso R., Wilcots E., 2008, Bent-double radio sources as probes of intergalactic gas, The Astrophysical Journal, 685, 858

Fumagalli M., O'Meara J. M., Prochaska J. X., Rafelski M., Kanekar N., 2015, Directly imaging damped Ly α galaxies at z > 2 - III. The star formation rates of neutral gas reservoirs at $z \sim 2.7$, Monthly Notices of the Royal Astronomical Society, 446, 3178

G. I. G. J'ozsa S. V. White K. T. O. M. S. P. S. M. R. A. J. T. R. S. J. P. D. C. M. S. M. F. M. M. D. K. P. K. B. V. H. W. J. G. d. B., Andati L. A. L., 2020, in Pizzo R., Deul E., Mol J.-D., de Plaa J., Verkouter H., eds, ASP Conf. Ser. Vol. 527, ADASS XXIX. San Francisco, pp 635–638

Gallimore J., Baum S., O'Dea C., Pedlar A., Brinks E., 1999, Neutral hydrogen (21 centimeter) absorption in seyfert galaxies: evidence for free-free absorption and sub-kiloparsec gaseous disks, The Astrophysical Journal, 524, 684

Gault L., et al., 2021, VLA Imaging of H I-bearing Ultra-diffuse Galaxies from the ALFALFA Survey, The Astrophysical Journal, 909, 19

Ghodsi L., Man A. W., Donevski D., Davé R., Lim S., Lovell C. C., Narayanan D., 2024, Star formation efficiency across large-scale galactic environments, Monthly Notices of the Royal Astronomical Society, 528, 4393

Giovanelli R., Haynes M. P., 1985, Gas deficiency in cluster galaxies : A comparison of nine clusters., The Astrophysical Journal, 292, 404

Giovanelli R., Haynes M. P., Kent B. R., 2005, The Arecibo Legacy Fast ALFA Survey. I. Science Goals, Survey Design, and Strategy, The Astronomical Journal, 130, 2598

Glowacki M., Albrow L., Reynolds T., Elson E., Mahony E., Allison J., 2024, A serendipitous discovery of H I rich galaxy groups with meerkat, Monthly Notices of the Royal Astronomical Society, 529, 3469

González V., Labbé I., Bouwens R. J., Illingworth G., Franx M., Kriek M., Brammer G. B., 2010, The Stellar Mass Density and Specific Star Formation Rate of the Universe at z $\sim$ 7, The Astrophysical Journal, 713, 115

Governato F., Tozzi P., Cavaliere A., 1995, Small groups of galaxies: a clue to a critical universe, arXiv preprint astro-ph/9508152

Grossi M., et al., 2009, The hi content of early-type galaxies from the alfalfa survey-ii. the case of low density environments, Astronomy & Astrophysics, 498, 407

Gunn J. E., Gott III J. R., 1972, On the infall of matter into clusters of galaxies and some effects on their evolution, The Astrophysical Journal, 176, 1

Guo H., Li C., Zheng Z., Mo H. J., Jing Y. P., Zu Y., Lim S. H., Xu H., 2017, Constraining the H I-Halo Mass Relation from Galaxy Clustering, The Astrophysical Journal, 846, 61

Gupta N., Srianand R., Bowen D. V., York D. G., Wadadekar Y., 2010, GMRT mini-survey to search for 21-cm absorption in quasar-galaxy pairs at z $\sim$ 0.1, Monthly Notices of the Royal Astronomical Society, 408, 849

Gupta N., Srianand R., Petitjean P., Bergeron J., Noterdaeme P., Muzahid S., 2012, Search for cold gas in strong Mg II absorbers at $0.5 < z < 1.5$: Nature and evolution of 21-cm absorbers, Astronomy and Astrophysics, 544, A21

Gupta N., et al., 2017, The MeerKAT Absorption Line Survey (MALS), arXiv:1708.07371 [astro-ph]

Gupta N., Momjian E., Srianand R., Petitjean P., Noterdaeme P., Gyanchandani D., Sharma R., Kulkarni S., 2018, Discovery of OH Absorption from a Galaxy at $z \sim 0.05$: Implications for Large Surveys with SKA Pathfinders, The Astrophysical Journal, 860, L22

Gupta N., et al., 2021, Blind H I and OH Absorption Line Search: First Results with MALS and uGMRT Processed Using ARTIP, The Astrophysical Journal, 907, 11

Haynes M. P., et al., 2011, The Arecibo Legacy Fast ALFA Survey: The α.40 H I Source Catalog, Its Characteristics and Their Impact on the Derivation of the H I Mass Function, The Astronomical Journal, 142, 170

Healy J., et al., 2021, H I content in Coma cluster substructure, Astronomy and Astrophysics, 650, A76

Hess K., Wilcots E., 2013, Evolution in the H I Gas content of galaxy groups: Pre-processing and mass assembly in the current epoch, Astronomical Journal, 146, 124

Hibbard J. E., van Gorkom J. H., 1996, HI, HII, and R-Band Observations of a Galactic Merger Sequence, The Astronomical Journal, 111, 655

Hickson P., 1982, Systematic properties of compact groups of galaxies, Astrophysical Journal, Part 1, vol. 255, Apr. 15, 1982, p. 382-391. Research supported by the Natural Sciences and Engineering Research Council of Canada., 255, 382

Hopkins P. F., Hernquist L., Cox T. J., Robertson B., Springel V., 2006, Determining the Properties and Evolution of Red Galaxies from the Quasar Luminosity Function, The Astrophysical Journal, 163, 50

Hoppmann L., Staveley-Smith L., Freudling W., Zwaan M. A., Minchin R. F., Calabretta M. R., 2015, A blind H I mass function from the Arecibo Ultra-Deep Survey (AUDS), Monthly Notices of the Royal Astronomical Society, 452, 3726

Hunter D. A., et al., 2012, Little Things, The Astronomical Journal, 144, 134

Jansen R. A., Franx M., Fabricant D., Caldwell N., 2000a, Surface photometry of nearby field galaxies: the data, The Astrophysical Journal Supplement Series, 126, 271

Jansen R. A., Fabricant D., Franx M., Caldwell N., 2000b, Spectrophotometry of nearby field galaxies: The data, The Astrophysical Journal Supplement Series, 126, 331

Jones D. H., et al., 2009, The 6df galaxy survey: final redshift release (dr3) and southern large-scale structures, Monthly Notices of the Royal Astronomical Society, 399, 683

Jones M. G., Haynes M. P., Giovanelli R., Moorman C., 2018a, The ALFALFA H I mass function: A dichotomy in the low-mass slope and a locally suppressed 'knee' mass, Monthly Notices of the Royal Astronomical Society, 477, 2

Jones M. G., et al., 2018b, The amiga sample of isolated galaxies-xiii. the hi content of an almost "nurture free" sample, Astronomy & Astrophysics, 609, A17

Jones M. G., et al., 2019, Evolution of compact groups from intermediate to final stages-a case study of the H I content of hcg 16, Astronomy & Astrophysics, 632, A78

Jones M., et al., 2023, Disturbed, diffuse, or just missing?-a global study of the H I content of hickson compact groups, Astronomy & Astrophysics, 670, A21

Jozsa G. I. G., Kenn F., Klein U., Oosterloo T. A., 2007, Kinematic modelling of disk galaxies: I. A new method to fit tilted rings to data cubes, Astronomy & Astrophysics, 468, 731

Józsa G. I., et al., 2020, Meerkathi–an end-to-end data reduction pipeline for meerkat and other radio telescopes, arXiv preprint arXiv:2006.02955

Józsa G. I. G., et al., 2021, Anomalous gas in ESO 149-G003: A MeerKAT-16 view, Monthly Notices of the Royal Astronomical Society, 501, 2704

Junkkarinen V. T., Barlow T. A., 1994, in American Astronomical Society Meeting Abstracts. p. 13.05

Kamphuis P., Józsa G. I. G., Oh S.-. H., Spekkens K., Urbancic N., Serra P., Koribalski B. S., Dettmar R. J. J., 2015, Automated kinematic modelling of warped galaxy discs in large H I surveys: 3D tilted-ring fitting of H I emission cubes, Monthly Notices of the Royal Astronomical Society, 452, 3139

Kanekar N., Chengalur J. N., Subrahmanyan R., Petitjean P., 2001, ATCA search for 21 cm emission from a candidate damped Ly-alpha absorber at $z = 0.101$, Astronomy and Astrophysics, 367, 46

Kanekar N., Subrahmanyan R., Chengalur J. N., Safouris V., 2003, The temperature of the warm neutral medium in the Milky Way, Monthly Notices of the Royal Astronomical Society, 346, L57

Kanekar N., Langston G. I., Stocke J. T., Carilli C. L., Menten K. M., 2012, Constraining Fundamental Constant Evolution with H I and OH Lines, The Astrophysical Journal, 746, L16

Kanekar N., et al., 2014, The spin temperature of high-redshift damped Lyman α systems, Monthly Notices of the Royal Astronomical Society, 438, 2131

Kanekar N., Neeleman M., Prochaska J. X., Ghosh T., 2018, The gas and stellar mass of low-redshift damped Lyman-α absorbers, Monthly Notices of the Royal Astronomical Society, 473, L54

Kannappan S. J., Fabricant D. G., Franx M., 2002, Physical Sources of Scatter in the Tully-Fisher Relation, The Astronomical Journal, 123, 2358

Kannappan S. J., et al., 2013, Connecting transitions in galaxy properties to refueling, The Astrophysical Journal, 777, 42

Kantharia N. G., Ananthakrishnan S., Nityananda R., Hota A., 2005, GMRT observations of the group Holmberg 124: Evolution by tidal forces and ram pressure?, Astronomy and Astrophysics, 435, 483

Kaur B., Kanekar N., Prochaska J. X., 2022, A fast radio burst progenitor born in a galaxy merger, The Astrophysical Journal, 925, L20

Keel W. C., Kennicutt Jr R., Hummel E., Van der Hulst J., 1985, The effects of interactions on spiral galaxies. i-nuclear activity and star formation, Astronomical Journal (ISSN 0004-6256), vol. 90, May 1985, p. 708-730., 90, 708

Keeney B. A., Momjian E., Stocke J. T., Carilli C. L., Tumlinson J., 2005, Absorption-Line Study of Halo Gas in NGC 3067 toward the Background Quasar 3C 232, The Astrophysical Journal, 622, 267

Kennicutt Robert C. Jr., 1989, The Star Formation Law in Galactic Disks, The Astrophysical Journal, 344, 685

Kennicutt R., Van Der Hulst J., 1997, The Interstellar Medium in Galaxies

Kennicutt Jr. R., 1998, The Global Schmidt Law in Star-forming Galaxies, The Astrophysical Journal, 498, 541

Kereš D., Katz N., Weinberg D. H., Davé R., 2005, How do galaxies get their gas?, Monthly Notices of the Royal Astronomical Society, 363, 2

Kerp J., Winkel B., Ben Bekhti N., Flöer L., Kalberla P. M., 2011, The effelsberg bonn hi survey (ebhis)

Kewley L. J., Geller M. J., Jansen R. A., 2004, [o ii] as a star formation rate indicator, The Astronomical Journal, 127, 2002

Kilborn V., Forbes D., Barnes D., Koribalski B., Brough S., Kern K., 2009, Southern GEMS groups-II. H I distribution, mass functions and H I deficient galaxies, Monthly Notices of the Royal Astronomical Society, 400, 1962

Klemola A., 1969, Groups and clusters of southern galaxies., Astronomical Journal, Vol. 74, p. 804-806, 74, 804

Kocjan Z., Cadiou C., Agertz O., Pontzen A., 2023, Hot gas accretion fuels star formation faster than cold accretion in high redshift galaxies, arXiv preprint arXiv:2311.04961

Koribalski B. S., et al., 2018, The Local Volume H i Survey (LVHIS), Monthly Notices of the Royal Astronomical Society, 478, 1611

Koribalski B. S., et al., 2020, Wallaby–an ska pathfinder h i survey, Astrophysics and Space Science, 365, 1

Krajnović D., Cappellari M., de Zeeuw P. T., Copin Y., 2006, Kinemetry: A generalization of photometry to the higher moments of the line-of-sight velocity distribution, Monthly Notices of the Royal Astronomical Society, 366, 787

Kreckel K., Platen E., Aragón-Calvo M. A., van Gorkom J. H., van de Weygaert R., van der Hulst J. M., Beygu B., 2012, The Void Galaxy Survey: Optical Properties and H I Morphology and Kinematics, The Astronomical Journal, 144, 16

Krogager J. K., Møller P., Fynbo J. P. U., Noterdaeme P., 2017, Consensus report on 25 yr of searches for damped Ly α galaxies in emission: Confirming their metallicity-luminosity relation at z $\sim$ 2, Monthly Notices of the Royal Astronomical Society, 469, 2959

Krogager J.-K., Fynbo J. P. U., Møller P., Noterdaeme P., Heintz K. E., Pettini M., 2019, The effect of dust bias on the census of neutral gas and metals in the high-redshift Universe due to SDSS-II quasar colour selection, Monthly Notices of the Royal Astronomical Society, 486, 4377

Krumholz M. R., McKee C. F., 2005, A General Theory of Turbulence-regulated Star Formation, from Spirals to Ultraluminous Infrared Galaxies, The Astrophysical Journal, 630, 250

Kurapati S., 2020, PhD thesis, TIFR, National Center for Radiophysics, Pune

Lagos P., Scott T., Nigoche-Netro A., Demarco R., Humphrey A., Papaderos P., 2018, Detecting metal-poor gas accretion in the star-forming dwarf galaxies um 461 and mrk 600, Monthly Notices of the Royal Astronomical Society, 477, 392

Larson R. B., Tinsley B. M., Caldwell C. N., 1980, The evolution of disk galaxies and the origin of S0 galaxies, The Astrophysical Journal, 237, 692

Lee H., Skillman E. D., Cannon J. M., Jackson D. C., Gehrz R. D., Polomski E. F., Woodward C. E., 2006, On Extending the Mass-Metallicity Relation of Galaxies by 2.5 Decades in Stellar Mass, The Astrophysical Journal, 647, 970

Lee N., et al., 2015, A turnover in the galaxy main sequence of star formation at m* 1010 m for redshifts z$<$ 1.3, The Astrophysical Journal, 801, 80

Leisman L., Haynes M. P., Giovanelli R., Józsa G., Adams E. A. K., Hess K. M., 2016, ALFALFA and WSRT imaging of extended H I features in the Leo Cloud of galaxies, Monthly Notices of the Royal Astronomical Society, 463, 1692

Leisman L., et al., 2017, (Almost) Dark Galaxies in the ALFALFA Survey: Isolated H I-bearing Ultra-diffuse Galaxies, The Astrophysical Journal, 842, 133

Lelli F., McGaugh S. S., Schombert J. M., 2016, The Small Scatter of the Baryonic Tully-Fisher Relation, The Astrophysical Journal, 816, L14

Lelli F., McGaugh S. S., Schombert J. M., Desmond H., Katz H., 2019, The baryonic Tully-Fisher relation for different velocity definitions and implications for galaxy angular momentum, Monthly Notices of the Royal Astronomical Society, 484, 3267

Lequeux J., Peimbert M., Rayo J. F., Serrano A., Torres-Peimbert S., 1979, Chemical Composition and Evolution of Irregular and Blue Compact Galaxies, Astronomy and Astrophysics, 80, 155

Leroy A. K., et al., 2013, Molecular Gas and Star Formation in nearby Disk Galaxies, The Astronomical Journal, 146, 19

Lilly S. J., Carollo C. M., Pipino A., Renzini A., Peng Y., 2013, Gas Regulation of Galaxies: The Evolution of the Cosmic Specific Star Formation Rate, the Metallicity-Mass-Star-formation Rate Relation, and the Stellar Content of Halos, The Astrophysical Journal, 772, 119

Lisenfeld U., et al., 2011, The AMIGA sample of isolated galaxies - IX. Molecular gas properties, Astronomy & Astrophysics, 534, A102

Maccagni F., Morganti R., Oosterloo T., Mahony E., 2014, What triggers a radio agn?-the intriguing case of pks b1718–649, Astronomy & Astrophysics, 571, A67

Mackenzie R., et al., 2019, Linking gas and galaxies at high redshift: MUSE surveys the environments of six damped Lyα systems at $z \sim 3$, Monthly Notices of the Royal Astronomical Society, 487, 5070

Madau P., Dickinson M., 2014, Cosmic Star Formation History, Annual Review of Astronomy and Astrophysics, 52, 415

Maddox N., et al., 2021, MIGHTEE-HI: The H I emission project of the MeerKAT MIGHTEE survey, Astronomy & Astrophysics, 646, A35

Maina E. K., et al., 2022, Mapping HI 21-cm in the Klemola 31 group at z = 0.029: Emission and absorption towards PKS2020-370, Monthly Notices of the Royal Astronomical Society, 516, 2050

Maiolino R., et al., 2008, AMAZE. I. The evolution of the mass-metallicity relation at $z > 3$, Astronomy and Astrophysics, 488, 463

Mannucci F., et al., 2009, LSD: Lyman-break galaxies Stellar populations and Dynamics - I. Mass, metallicity and gas at z $\sim$ 3.1, Monthly Notices of the Royal Astronomical Society, 398, 1915

Mannucci F., Cresci G., Maiolino R., Marconi A., Gnerucci A., 2010, A fundamental relation between mass, star formation rate and metallicity in local and high-redshift galaxies, Monthly Notices of the Royal Astronomical Society, 408, 2115

Mapelli M., Moore B., Bland-Hawthorn J., 2008, Lopsided galaxies: the case of ngc 891, Monthly Notices of the Royal Astronomical Society, 388, 697

Martin C. L., Kennicutt Robert C. Jr., 2001, Star Formation Thresholds in Galactic Disks, The Astrophysical Journal, 555, 301

Martin A. M., Papastergis E., Giovanelli R., Haynes M. P., Springob C. M., Stierwalt S., 2010, The arecibo legacy fast alfa survey. x. the H I mass function and from the 40% alfalfa survey, The Astrophysical Journal, 723, 1359

Martin A. M., Giovanelli R., Haynes M. P., Guzzo L., 2012, The Clustering Characteristics of H I-selected Galaxies from the 40% ALFALFA Survey, The Astrophysical Journal, 750, 38

McGaugh S. S., Schombert J. M., Bothun G. D., 2000, THE BARYONIC TULLY-FISHER RELATION, The Astrophysical Journal, 533, L99

McMullin J. P., Waters B., Schiebel D., Young W., Golap K., 2007, in Astronomical data analysis software and systems XVI. p. 127

Mendes de Oliveira C., Hickson P., 1991, The luminosity function of compact groups of galaxies, Astrophysical Journal, Part 1 (ISSN 0004-637X), vol. 380, Oct. 10, 1991, p. 30-38. Research supported by NSERC., 380, 30

Meyer M., et al., 2004, The HIPASS catalogue - I. Data presentation, Monthly Notices of the Royal Astronomical Society, 350, 1195

Meyer M., Zwaan M., Webster R., Schneider S., Staveley-Smith L., 2008, Tully-Fisher relations from an H I-selected sample, Monthly Notices of the Royal Astronomical Society, 391, 1712

Mo H. J., Mao S., White S. D. M., 1998, The formation of galactic discs, Monthly Notices of the Royal Astronomical Society, 295, 319

Mocz P., Green A., Malacari M., Glazebrook K., 2012, The Tully-Fisher Relation for 25,000 SDSS Galaxies as Function of Environment, Monthly Notices of the Royal Astronomical Society, 425, 296

Mohan N., Rafferty D., Norris R. P., 2015, Astrophysics Source Code Library, record ascl: 1502.007

Moore B., Lake G., Katz N., 1998, Morphological Transformation from Galaxy Harassment, The Astrophysical Journal, 495, 139

Moorman C. M., Vogeley M. S., Hoyle F., Pan D. C., Haynes M. P., Giovanelli R., 2014, The H I mass function and velocity width function of void galaxies in the Arecibo Legacy Fast ALFA Survey, Monthly Notices of the Royal Astronomical Society, 444, 3559

Moorman C. M., Moreno J., White A., Vogeley M. S., Hoyle F., Giovanelli R., Haynes M. P., 2016, On the Star Formation Properties of Void Galaxies, The Astrophysical Journal, 831, 118

Morganti R., Peck A., Oosterloo T., van Moorsel G., Capetti A., Fanti R., Parma P., de Ruiter H., 2009, Is cold gas fuelling the radio galaxy ngc 315?, Astronomy & Astrophysics, 505, 559

Morganti R., Holt J., Tadhunter C., Ramos Almeida C., Dicken D., Inskip K., Oosterloo T., Tzioumis T., 2011, PKS 1814-637: A powerful radio-loud AGN in a disk galaxy, Astronomy and Astrophysics, 535, A97

Morganti R., Fogasy J., Paragi Z., Oosterloo T., Orienti M., 2013, Radio Jets Clearing the Way Through a Galaxy: Watching Feedback in Action, Science, 341, 1082

Moss V. A., et al., 2017, Connecting X-ray absorption and 21 cm neutral hydrogen absorption in obscured radio AGN, Monthly Notices of the Royal Astronomical Society, 471, 2952

Narayan C. A., Jog C. J., 2002, Origin of radially increasing stellar scaleheight in a galactic disk, Astronomy and Astrophysics, 390, L35

Navarro J. F., Steinmetz M., 2000, Dark Halo and Disk Galaxy Scaling Laws in Hierarchical Universes, The Astrophysical Journal, 538, 477

Neeleman M., Prochaska J. X., Ribaudo J., Lehner N., Howk J. C., Rafelski M., Kanekar N., 2016, The H I content of the universe over the past 10 gyr, The Astrophysical Journal, 818, 113

Neeleman M., Kanekar N., Prochaska J. X., Rafelski M., Carilli C. L., Wolfe A. M., 2017, [C II] 158-∼ mum emission from the host galaxies of damped Lyman-alpha systems, Science, 355, 1285

Nelder J. A., Mead R., 1965, A simplex method for function minimization, The computer journal, 7, 308

Nielsen N. M., Churchill C. W., Kacprzak G. G., Murphy M. T., 2013, MAGIICAT I. The Mg II Absorber-Galaxy Catalog, The Astrophysical Journal, 776, 114

Noeske K. G., et al., 2007, Star Formation in AEGIS Field Galaxies since z=1.1: The Dominance of Gradually Declining Star Formation, and the Main Sequence of Star-forming Galaxies, The Astrophysical Journal, 660, L43

Noordam J. E., Smirnov O. M., 2010, The meqtrees software system and its use for third-generation calibration of radio interferometers, Astronomy & Astrophysics, 524, A61

Noordermeer E., Van Der Hulst J. M., Sancisi R., Swaters R. A., Van Albada T. S., 2005, The Westerbork HI survey of spiral and irregular galaxies. III. HI observations of early-type disk galaxies, A&A, 442, 137

Noterdaeme P., Ledoux C., Petitjean P., Srianand R., 2008, Molecular hydrogen in high-redshift damped Lyman-α systems: The VLT/UVES database, Astronomy and Astrophysics, 481, 327

Noterdaeme P., Petitjean P., Pâris I., Cai Z., Finley H., Ge J., Pieri M. M., York D. G., 2014, A connection between extremely strong damped Lyman-α systems and Lyman-α emitting galaxies at small impact parameters, Astronomy and Astrophysics, 566, A24

O'Sullivan E., et al., 2014, Deep chandra observations of hcg 16. ii. the development of the intra-group medium in a spiral-rich group, The Astrophysical Journal, 793, 74

Offringa A. R., 2010, AOFlagger: RFI Software, ascl, p. ascl:1010.017

Offringa A., et al., 2014, Wsclean: an implementation of a fast, generic wide-field imager for radio astronomy, Monthly Notices of the Royal Astronomical Society, 444, 606

Oh S.-H. H., Staveley-Smith L., Spekkens K., Kamphuis P., Koribalski B. S., 2018, 2D Bayesian automated tilted-ring fitting of disc galaxies in large H I galaxy surveys: 2dbat, Monthly Notices of the Royal Astronomical Society, 473, 3256

Onodera M., et al., 2016, ISM Excitation and Metallicity of Star-forming Galaxies at z $\simeq$ 3.3 from Near-IR Spectroscopy, The Astrophysical Journal, 822, 42

Patiri S. G., Prada F., Holtzman J., Klypin A., Betancort-Rijo J., 2006, The properties of galaxies in voids, Monthly Notices of the Royal Astronomical Society, 372, 1710

Patra N. N., Banerjee A., Chengalur J. N., Begum A., 2014, Modelling H I distribution and kinematics in the edge-on dwarf irregular galaxy KK250, Monthly Notices of the Royal Astronomical Society, 445, 1424

Patra N. N., Chengalur J. N., Karachentsev I. D., Sharina M. E., 2016a, FIGGS 2: An HI survey of extremely faint irregular galaxies, Astrophysical Bulletin, 71, 408

Patra N. N., Chengalur J. N., Karachentsev I. D., Kaisin S. S., Begum A., 2016b, Cold H I in faint dwarf galaxies, Monthly Notices of the Royal Astronomical Society, 456, 2467

Peeples M. S., Shankar F., 2011, Constraints on star formation driven galaxy winds from the mass-metallicity relation at $z = 0$, Monthly Notices of the Royal Astronomical Society, 417, 2962

Pence W. D., Chiappetti L., Page C. G., Shaw R. A., Stobie E., 2010, Definition of the Flexible Image Transport System (FITS), version 3.0, Astronomy & Astrophysics, 524, A42

Péroux C., Bouché N., Kulkarni V. P., York D. G., Vladilo G., 2012, A SINFONI integral field spectroscopy survey for galaxy counterparts to damped Lyman α systems - III. Three additional detections, Monthly Notices of the Royal Astronomical Society, 419, 3060

Petrov L., Kovalev Y., 2017, On significance of vlbi/gaia position offsets, Monthly Notices of the Royal Astronomical Society: Letters, 467, L71

Pizagno J., et al., 2007, The Tully-Fisher Relation and its Residuals for a Broadly Selected Sample of Galaxies, The Astronomical Journal, 134, 945

Poggianti B. M., Smail I., Dressler A., Couch W. J., Barger A. J., Butcher H., Ellis R. S., Oemler Augustus Jr., 1999, The Star Formation Histories of Galaxies in Distant Clusters, The Astrophysical Journal, 518, 576

Polak B., et al., 2023, Massive star cluster formation i. high star formation efficiency while resolving feedback of individual stars, arXiv preprint arXiv:2312.06509

Ponomareva A. A., Verheijen M. A. W., Bosma A., 2016, Detailed H I kinematics of Tully-Fisher calibrator galaxies, Monthly Notices of the Royal Astronomical Society, 463, 4052

Ponomareva A. A., Verheijen M. A. W., Peletier R. F., Bosma A., 2017, The multiwavelength Tully-Fisher relation with spatially resolved H I kinematics, Monthly Notices of the Royal Astronomical Society, 469, 2387

Pustilnik S. A., Martin J. M., 2016, Study of galaxies in the Lynx-Cancer void. VI. H I-observations with Nançay Radio Telescope, Astronomy and Astrophysics, 596, A86

Putman M. E., 2017, in Fox A., Davé R., eds, Astrophysics and Space Science Library Vol. 430, Gas Accretion onto Galaxies. p. 1, doi:10.1007/978-3-319-52512-9_1

Rahmani H., Srianand R., Gupta N., Petitjean P., Noterdaeme P., Vásquez D. A., 2012, Constraining the variation of fundamental constants at $z \sim 1.3$ using 21-cm absorbers, Monthly Notices of the Royal Astronomical Society, 425, 556

Ranchod S., et al., 2021, Mightee-hi: discovery of an H I rich galaxy group at z= 0.044 with meerkat, Monthly Notices of the Royal Astronomical Society, 506, 2753

Ranjan A., et al., 2018, Molecular gas and star formation in an absorption-selected galaxy: Hitting the bull's eye at z $\simeq$ 2.46, Astronomy and Astrophysics, 618, A184

Ranjan A., Noterdaeme P., Krogager J. K., Petitjean P., Srianand R., Balashev S. A., Gupta N., Ledoux C., 2020, Chemical enrichment and host galaxies of extremely strong intervening DLAs towards quasars. Do they probe the same galactic environments as DLAs associated with $\sim$ gamma-ray burst afterglows?, Astronomy and Astrophysics, 633, A125

Rao S. M., Belfort-Mihalyi M., Turnshek D. A., Monier E. M., Nestor D. B., Quider A., 2011, A ground-based imaging study of galaxies causing damped Lyman α (DLA), sub-DLA and Lyman limit system absorption in quasar spectra, Monthly Notices of the Royal Astronomical Society, 416, 1215

Rasmussen J., Ponman T. J., Verdes-Montenegro L., Yun M. S., Borthakur S., 2008, Galaxy evolution in Hickson compact groups: The role of ram-pressure stripping and strangulation, Monthly Notices of the Royal Astronomical Society, 388, 1245

Rees M. J., Ostriker J. P., 1977, Cooling, dynamics and fragmentation of massive gas clouds: Clues to the masses and radii of galaxies and clusters., Monthly Notices of the Royal Astronomical Society, 179, 541

Reeves S. N., et al., 2016, H I emission and absorption in nearby, gas-rich galaxies - II. Sample completion and detection of intervening absorption in NGC 5156, Monthly Notices of the Royal Astronomical Society, 457, 2613

Rogstad D. H., Lockhart I. A., Lockart I. A., Wright M. C. H., 1974, Aperture-synthesis observations of H I in the galaxy M 83., The Astrophysical Journal, 193, 309

Rojas R. R., Vogeley M. S., Hoyle F., Brinkmann J., 2004, Photometric Properties of Void Galaxies in the Sloan Digital Sky Survey, The Astrophysical Journal, 617, 50

Roychowdhury S., Chengalur J. N., Begum A., Karachentsev I. D., 2009, Star formation in extremely faint dwarf galaxies, Monthly Notices of the Royal Astronomical Society, 397, 1435

Roychowdhury S., Chengalur J. N., Kaisin S. S., Begum A., Karachentsev I. D., 2011, Small Bites: Star formation recipes in extreme dwarfs, Monthly Notices of the Royal Astronomical Society, 414, L55

Roychowdhury S., Chengalur J. N., Kaisin S. S., Karachentsev I. D., 2014, The relation between atomic gas and star formation rate densities in faint dwarf irregular galaxies, Monthly Notices of the Royal Astronomical Society, 445, 1392

Roychowdhury S., Arabsalmani M., Kanekar N., 2019, H I 21 cm mapping of the host galaxy of AT2018cow: A fast-evolving luminous transient within a ring of high column density gas, Monthly Notices of the Royal Astronomical Society, 485, L93

Roychowdhury S., et al., 2022, The Variation of the Gas Content of Galaxy Groups and Pairs Compared to Isolated Galaxies, The Astrophysical Journal, 927, 20

Rubin K. H. R., Diamond-Stanic A. M., Coil A. L., Crighton N. H. M., Moustakas J., 2018, Galaxies probing galaxies in primus. i. sample, spectroscopy, and characteristics of the mg ii–absorbing circumgalactic medium, The Astrophysical Journal, 853, 95

Sabater J., Best P., Argudo-Fernández M., 2013, Effect of the interactions and environment on nuclear activity, Monthly Notices of the Royal Astronomical Society, 430, 638

Said K., Kraan-Korteweg R. C., Staveley-Smith L., 2019, The H I mass function in the Parkes H I Zone of Avoidance survey, Monthly Notices of the Royal Astronomical Society, 486, 1796

Sánchez Almeida J., Elmegreen B. G., Munoz-Tunón C., Elmegreen D. M., 2014, Star formation sustained by gas accretion, The Astronomy and Astrophysics Review, 22, 1

Sancisi R., Fraternali F., Oosterloo T., van der Hulst T., 2008a, Cold gas accretion in galaxies, åpr, 15, 189

Sancisi R., Fraternali F., Oosterloo T., Van Der Hulst T., 2008b, Cold gas accretion in galaxies, The Astronomy and Astrophysics Review, 15, 189

Sanders D., Mirabel I., 1996, Luminous infrared galaxies, Annual Review of Astronomy and Astrophysics, 34, 749

Sanders R. L., et al., 2015, The MOSDEF Survey: Mass, Metallicity, and Star-formation Rate at z $\sim$ 2.3, The Astrophysical Journal, 799, 138

Sanders R. L., et al., 2018, The MOSDEF Survey: A Stellar Mass-SFR-Metallicity Relation Exists at $z \sim 2.3$, The Astrophysical Journal, 858, 99

Sargent W. L., 1968, The redshifts of galaxies in the remarkable chain vv 172, Astrophysical Journal, vol. 153, p. L135, 153, L135

Savaglio S., et al., 2005, The Gemini Deep Deep Survey. VII. The Redshift Evolution of the Mass-Metallicity Relation, The Astrophysical Journal, 635, 260

Schawinski K., et al., 2014, The green valley is a red herring: Galaxy zoo reveals two evolutionary pathways towards quenching of star formation in early-and late-type galaxies, Monthly Notices of the Royal Astronomical Society, 440, 889

Schaye J., 2004, Star Formation Thresholds and Galaxy Edges: Why and Where, The Astrophysical Journal, 609, 667

Schmidt M., 1959a, The Rate of Star Formation., The Astrophysical Journal, 129, 243

Schmidt M., 1959b, The rate of star formation, Astrophysical Journal, 129, 243

Schoenmakers R. H. M., Franx M., de Zeeuw P. T., 1997, Measuring non-axisymmetry in spiral galaxies, Monthly Notices of the Royal Astronomical Society, 292, 349

Schulman E., Bregman J. N., Roberts M. S., 1994, An hi survey of high-velocity clouds in nearby disk galaxies, The Astrophysical Journal, Part 1 (ISSN 0004-637X), vol. 423, no. 1, p. 180-189, 423, 180

Schulz R., Morganti R., Nyland K., Paragi Z., Mahony E. K., Oosterloo T., 2021, Parsec-scale HI outflows in powerful radio galaxies, Astronomy and Astrophysics, 647, A63

Serra P., et al., 2012, The atlas3d project–xiii. mass and morphology of h i in early-type galaxies as a function of environment, Monthly Notices of the Royal Astronomical Society, 422, 1835

Serra P., et al., 2014, The ATLAS3D project – XXVI. H i discs in real and simulated fast and slow rotators, Monthly Notices of the Royal Astronomical Society, 444, 3388

Serra P., et al., 2015, SOFIA: a flexible source finder for 3D spectral line data, Monthly Notices of the Royal Astronomical Society, 448, 1922

Shetty R., Kelly B. C., Rahman N., Bigiel F., Bolatto A. D., Clark P. C., Klessen R. S., Konstandin L. K., 2014, Indications of a sub-linear and non-universal Kennicutt-Schmidt relationship, Monthly Notices of the Royal Astronomical Society, 437, L61

Simon J. D., Bolatto A. D., Leroy A., Blitz L., 2003, High-Resolution Measurements of the Dark Matter Halo of NGC 2976: Evidence for a Shallow Density Profile, The Astrophysical Journal, 596, 957

Simon J. D., Bolatto A. D., Leroy A., Blitz L., Gates E. L., 2005, High-Resolution Measurements of the Halos of Four Dark Matter-Dominated Galaxies: Deviations from a Universal Density Profile, The Astrophysical Journal, 621, 757

Skillman E. D., 1996, in The Minnesota Lectures on Extragalactic Neutral Hydrogen. p. 208

Skrutskie M., et al., 2006, The two micron all sky survey (2mass), The Astronomical Journal, 131, 1163

Solanes J. M., Manrique A., García-Gómez C., González-Casado G., Giovanelli R., Haynes M. P., 2001, The H I Content of Spirals. II. Gas Deficiency in Cluster Galaxies, The Astrophysical Journal, 548, 97

Springob C. M., Haynes M. P., Giovanelli R., Kent B. R., 2005, A digital archive of hi 21 centimeter line spectra of optically targeted galaxies, The Astrophysical Journal Supplement Series, 160, 149

Srianand R., Gupta N., Petitjean P., Noterdaeme P., Ledoux C., 2010, Detection of 21-cm, H_2 and deuterium absorption at $z > 3$ along the line of sight to J1337+3152, Monthly Notices of the Royal Astronomical Society, 405, 1888

Srianand R., Gupta N., Petitjean P., Noterdaeme P., Ledoux C., Salter C. J., Saikia D. J., 2012, Search for cold gas in $z > 2$ damped Lyα systems: 21-cm and H_2 absorption, Monthly Notices of the Royal Astronomical Society, 421, 651

Srianand R., Gupta N., Rahmani H., Momjian E., Petitjean P., Noterdaeme P., 2013a, Parsec-scale structures and diffuse bands in a translucent interstellar medium at $z \simeq 0.079$, Monthly Notices of the Royal Astronomical Society, 428, 2198

Srianand R., Gupta N., Rahmani H., Momjian E., Petitjean P., Noterdaeme P., 2013b, Parsec-scale structures and diffuse bands in a translucent interstellar medium at z 0.079, Monthly Notices of the Royal Astronomical Society, 428, 2198

Srianand R., Hussain T., Noterdaeme P., Petitjean P., Krühler T., Japelj J., Pâris I., Kashikawa N., 2016, Detection of emission lines from $z \sim 3$ DLAs towards the QSO J2358+0149, Monthly Notices of the Royal Astronomical Society, 460, 634

Steidel C. C., Dickinson M., Persson S. E., 1994, Field Galaxy Evolution Since Z approximately 1 from a Sample of QSO Absorption–selected Galaxies, The Astrophysical Journal, 437, L75

Stevens A. R. H., Diemer B., Lagos C. d. P., Nelson D., Obreschkow D., Wang J., Marinacci F., 2019, Origin of the galaxy H I size-mass relation, Monthly Notices of the Royal Astronomical Society, 490, 96

Struve C., Conway J. E., 2010, An H I absorbing circumnuclear disk in Cygnus A, Astronomy and Astrophysics, 513, A10

Swaters R. A., 1999, PhD thesis, University of Groningen

Swaters R. A., van Albada T. S., van der Hulst J. M., Sancisi R., 2002, The Westerbork HI survey of spiral and irregular galaxies: I. HI imaging of late-type dwarf galaxies, Astronomy & Astrophysics, 390, 829

Teng Y.-H., et al., 2024, Star formation efficiency in nearby galaxies revealed with a new co-to-h2 conversion factor prescription, The Astrophysical Journal, 961, 42

Teuben P. J., 1991, in Warped Disks and Inclined Rings around Galaxies. p. 40

Teuben P., 1995, in Shaw R. A., Payne H. E., Hayes J. J. E., eds, Astronomical Society of the Pacific Conference Series Vol. 77, Astronomical Data Analysis Software and Systems IV. p. 398

Theureau G., Hanski M., Coudreau N., Hallet N., Martin J., 2007, Kinematics of the local universe, A&A, 465, 71

Tobias Westmeier 2021, SoFiA 2 User Manual, pp 1–47

Tremblay G. R., et al., 2016, Cold, clumpy accretion onto an active supermassive black hole, Nature, 534, 218

Tremonti C. A., et al., 2004, The Origin of the Mass-Metallicity Relation: Insights from 53,000 Star-forming Galaxies in the Sloan Digital Sky Survey, The Astrophysical Journal, 613, 898

Tully R. B., Fisher J. R., 1977, A new method of determining distances to galaxies., A&A, 54, 661

Tully R. B., Pierce M. J., 2000, Distances to Galaxies from the Correlation between Luminosities and Line Widths. III. Cluster Template and Global Measurement of H_0, The Astrophysical Journal, 533, 744

Van Albada T. S., Bahcall J. N., Begeman K., Sanscisi R., 1985, Distribution of dark matter in the spiral galaxy NGC 3198., ApJ. . ., 295, 305

Van Weeren R. J., et al., 2012, First LOFAR observations at very low frequencies of cluster-scale non-thermal emission: the case of Abell 2256, Astronomy & astrophysics, 543, A43

Verdes-Montenegro L., Yun M. S., Williams B. A., Huchtmeier W. K., Del Olmo A., Perea J., 2001, Where is the neutral atomic gas in Hickson groups?, Astronomy & Astrophysics, 377, 812

Verheijen M. A. W., Sancisi R., 2001, The ursa major cluster of galaxies - IV. HI synthesis observations, Astronomy & Astrophysics, 370, 765

Verheijen M., van Gorkom J. H., Szomoru A., Dwarakanath K. S., Poggianti B. M., Schiminovich D., 2007, WSRT Ultradeep Neutral Hydrogen Imaging of Galaxy Clusters at z $\sim$ 0.2: A Pilot Survey of Abell 963 and Abell 2192, The Astrophysical Journal, 668, L9

Verheijen M., Oosterloo T., Heald G., van Cappellen W., 2009, Hi surveys with apertif, Panoramic radio astronomy: wide-field, pp 1–2

Vollmer B., Cayatte V., Balkowski C., Duschl W. J., 2001, Ram Pressure Stripping and Galaxy Orbits: The Case of the Virgo Cluster, The Astrophysical Journal, 561, 708

Walter F., Brinks E., de Blok W. J. G., Bigiel F., Kennicutt R. C., Thornley M. D., Leroy A. K., 2008, THINGS: THE H I NEARBY GALAXY SURVEY, The Astronomical Journal, 136, 2563

Wang J., et al., 2013, The Bluedisks project, a study of unusually H I-rich galaxies - I. H I sizes and morphology, Monthly Notices of the Royal Astronomical Society, 433, 270

Wang J., Koribalski B. S., Serra P., van der Hulst T., Roychowdhury S., Kamphuis P., Chengalur J. N., 2016, New lessons from the H I size-mass relation of galaxies, Monthly Notices of the Royal Astronomical Society, 460, 2143

Welty D. E., Morton D. C., Hobbs L., 1996, A high-resolution survey of interstellar ca ii absorption, Astrophysical Journal Supplement v. 106, p. 533, 106, 533

Westmeier T., et al., 2021, Sofia 2 – an automated, parallel H i source finding pipeline for the WALLABY survey, Monthly Notices of the Royal Astronomical Society, 506, 3962

Whitaker K. E., van Dokkum P. G., Brammer G., Franx M., 2012, THE STAR FORMATION MASS SEQUENCE OUT TO z = 2.5, The Astrophysical Journal Letters, 754, L29

Whiting M. T., 2012, duchamp: a 3d source finder for spectral-line data, Monthly Notices of the Royal Astronomical Society, 421, 3242

Wolfe A. M., Brown R. L., Roberts M. S., 1976, Limits on the variation of fundamental atomic quantities over cosmic time scales, Physical Review Letters, 37, 179

Wolfe A. M., Briggs F. H., Turnshek D. A., Davis M. M., Smith H. E., Cohen R. D., 1985, Detection of 21 centimeter absorption at Z = 2.04 in the QSO PKS 0458-02., The Astrophysical Journal, 294, L67

Wong O. I., et al., 2006, The northern hipass catalogue–data presentation, completeness and reliability measures, Monthly Notices of the Royal Astronomical Society, 371, 1855

Wyder T. K., et al., 2009, THE STAR FORMATION LAW AT LOW SURFACE DENSITY, The Astrophysical Journal, 696, 1834

Xu J.-L., et al., 2021, Discovery of Extraplanar H I Clouds and a H I Tail in the M101 Galaxy Group with FAST, The Astrophysical Journal, 922, 53

Yoon H., Chung A., Smith R., Jaffé Y. L., 2017, A History of H I Stripping in Virgo: A Phase-space View of VIVA Galaxies, The Astrophysical Journal, 838, 81

Young J. S., Knezek P. M., 1989, The ratio of molecular to atomic gas in spiral galaxies as a function of morphological type, The Astrophysical Journal, 347, L55

Zabludoff A. I., Mulchaey J. S., 1998, The Properties of Poor Groups of Galaxies. I. Spectroscopic Survey and Results, The Astrophysical Journal, 496, 39

Zhang C.-P., et al., 2024, The fast all sky H I survey (fashi): The first release of catalog, Science China Physics, Mechanics & Astronomy, 67, 219511

Zuo P., Ho L. C., Wang J., Yu N., Shangguan J., 2022, Massive galaxy mergers have distinctive global h i profiles, The Astrophysical Journal, 929, 15

Zwaan M. A., Prochaska J. X., 2006, Where Is the Molecular Hydrogen in Damped Lyα Absorbers?, The Astrophysical Journal, 643, 675

Zwaan M. A., et al., 2003, The 1000 brightest hipass galaxies: The H I mass function and $\omega_{\rm H\,I}$, The Astronomical Journal, 125, 2842

Zwaan M. A., Meyer M. J., Staveley-Smith L., Webster R. L., 2005, The HIPASS catalogue: Omega$_{\rm H\,I}$ and environmental effects on the H I mass function of galaxies, Monthly Notices of the Royal Astronomical Society: Letters, 359, L30

Zwaan M. A., Liske J., Péroux C., Murphy M. T., Bouché N., Curran S. J., Biggs A. D., 2015, New H I 21-cm absorbers at low and intermediate redshifts, Monthly Notices of the Royal Astronomical Society, 453, 1268

de Avillez M. A., Breitschwerdt D., 2005, Global dynamical evolution of the ISM in star forming galaxies. I. High resolution 3D simulations: Effect of the magnetic field, Astronomy and Astrophysics, 436, 585 de Blok W. J. G., et al., 2014, A low H I column density filament in NGC 2403: Signature of interaction or accretion, Astronomy and Astrophysics, 569, A68

de Blok W. J. G., et al., 2016, in MeerKAT Science: On the Pathway to the SKA. p. 7

de los Reyes M. A. C., Kennicutt Robert C. Jr., 2019, Revisiting the Integrated Star Formation Law. I. Non-starbursting Galaxies, The Astrophysical Journal, 872, 16

di Serego Alighieri S., et al., 2007, The hi content of early-type galaxies from the alfalfa survey-i. catalogued hi sources in the virgo cluster, Astronomy & Astrophysics, 474, 851

von Benda-Beckmann A. M., Müller V., 2008, Void statistics and void galaxies in the 2dF Galaxy Redshift Survey, Monthly Notices of the Royal Astronomical Society, 384, 1189